

## ABSTRACT

Title of Dissertation: ENGINEERING OF SELF-ASSEMBLED  
MULTIFERROIC NANOSTRUCTURES IN  
PbTiO<sub>3</sub>-CoFe<sub>2</sub>O<sub>4</sub> THIN FILMS

Jianhua Li, Doctor of Philosophy, 2006

Dissertation Directed By: Professor A. L. Roytburd  
Department of Materials Science and  
Engineering

Multiferroic materials which display a coexistence of ferroelectric and ferromagnetic properties attract considerable interest for their potential for novel device applications as well as for the interesting physics and materials science underlying their functional responses. In multiferroic composite, electromagnetic coupling facilitate elastic interaction between ferroelectric and ferromagnetic components via piezoeffect and magnetostriction. The major goal of our research is designing the transverse epitaxial multiferroic nanostructures with controlled morphologies. The PbTiO<sub>3</sub>-CoFe<sub>2</sub>O<sub>4</sub> system was selected for this study because of the (i) large spontaneous strain associated with the ferroelectric phase transition in PbTiO<sub>3</sub> (6.5%), which should create strong elastic interactions between the two phases accompanying the piezoelectric effect, and (ii) large magnetostriction of ferrimagnetic CoFe<sub>2</sub>O<sub>4</sub>.

We successfully fabricate self-assembling multiferroic nanostucture films of CoFe<sub>2</sub>O<sub>4</sub>-PbTiO<sub>3</sub> by PLD deposition on SrTiO<sub>3</sub> substrates of different orientations. X-

ray and TEM characterization show that all films have columnar architecture and 3D epitaxial relationships between phases and each phase and substrates. The morphology of nanostructures has been controlled by changing orientation of a substrate. It has been shown that it is possible to obtain the ferromagnetic ( $\text{CoFe}_2\text{O}_4$ ) rods with a diameter about 10-20 nm in the ferroelectric  $\text{PbTiO}_3$  matrix in (001) films of composition  $0.67\text{PbTiO}_3\text{-}0.33\text{CoFe}_2\text{O}_4$ , and vice versa: ferroelectric rods in ferrimagnetic matrix in (111) films of composition  $0.33\text{PbTiO}_3\text{-}0.67\text{CoFe}_2\text{O}_4$ . The lamellate morphology with a specific crystallographic orientation of lamellae corresponding to  $\{111\}$  planes has been obtained in (110) films. The measurements of lattice parameters of the constitutive phases at different temperature allows us to determine the level of internal stresses due to misfit between phases. The measurements of piezo- and magnetic responses of the films prove that the films are ferroelectric and ferromagnetic simultaneously. The piezo- and magnetic responses are considerable suppressed due to mutual constraints between phases. This suppression indicates the strong elastic interactions between the phases which allows us to suggest the strong electro-magnetic coupling in the films. Combining theoretical and experimental studies of self-assembled multiferroic nanostructures in epitaxial films has revealed that the elastic interactions caused by epitaxial stresses play the dominate role in defining the morphology of the nanostructures and their magnetic and electric responses.

ENGINEERING OF SELF-ASSEMBLED MULTIFERROIC NANOSTRUCTURES  
IN  $\text{PbTiO}_3\text{-CoFe}_2\text{O}_4$  THIN FILMS

By

Jianhua Li

Dissertation submitted to the Faculty of the Graduate School of the  
University of Maryland, College Park, in partial fulfillment  
of the requirements for the degree of  
Doctor of Philosophy  
2006

Advisory Committee:

Professor A. Roytburd, Chair/Advisor  
Professor J. Melngailis  
Professor A. Christou  
Professor M. Wuttig  
Professor J. Cullen

© Copyright by  
Jianhua Li  
2006

## DEDICATION

*To my family*

## ACKNOWLEDGEMENTS

I would like to express my sincere gratitude to my advisors, Prof. A. L. Roytburd for giving me the opportunity to work on this exciting project and for his faith, guidance and support throughout the course of my Ph.D. research. I have been working with Prof. A. L. Roytburd since the first day I came to the U.S. I benefited from his guidance in every aspect during my Ph.D study. It was his wide knowledge of materials science especially on thermodynamics of elastic domains, creative thoughts and sparkling of fresh ideas, dedication to scientific excellence, and most important, his pure love and enthusiasm toward scientific research, that had led to every progress in my Ph.D. research. I deeply appreciate all his invaluable help, the care he showed for me, and the freedom he gave me. The same gratitude goes to Prof. R. Ramesh, who gave me the opportunity to be a part of his team at the Advanced Thin Film Laboratory, which is at the forefront of research in oxide thin film materials.

I would like to thank the other members of my Ph.D. committee Prof. M. Wuttig, Prof. A. Christou, Prof. J. Megailias and Prof. J. Cullen for taking time out of their busy schedules to evaluate my work.

I would also like to thank Dr. Martin Green (NIST) who gave me the opportunity to use all the facilities in the NIST, and his consistence support from the entire field.

I would also like to thank Dr. Igor Levin (NIST) for all the TEM work, discussion, and support.

I would also like to thank Dr. Julia Slutsker (NIST) for the theoretical simulation and discussion.

I would also like to thank Dr. Peter Schenck (NIST) who gave me the freedom to use his lab.

I show my gratitude for the helping hands from my friends in our research group, Tong Zhao, Junling Wang, for all the helpful discussion of my experiments, Zhenkun Ma for the piezoelectric measurements, Haimei Zheng for the TEM characterization. I want to thank all of the group members at University of Maryland, Lang Chen and Jun Ouyang. My research has been so exciting because of all the talented and great team members.

I would like to thank all my friends who made my life in the U.S. colorful.

Finally, I want to thank my husband and my son for their love, enthusiasm and support. I wouldn't have gone this far without their unfaltering belief and support.

# TABLE OF CONTENTS

|   |             |
|---|-------------|
| <b>DEDICATION .....</b>   | <b>ii</b>   |
| <b>ACKNOWLEDGEMENTS .....</b>   | <b>iii</b>  |
| <b>TABLE OF CONTENTS .....</b>  | <b>v</b>    |
| <b>LIST OF TABLES.....</b>  | <b>vii</b>  |
| <b>LIST OF FIGURES.....</b>   | <b>viii</b> |
| <b>Chapter 1: Motivation and Objectives of Research .....</b>               | <b>1</b>    |
| <b>Chapter 2. Physical Background.....</b>                                  | <b>5</b>    |
| 2.1 Ferroelectricity and Piezoelectricity .....                             | 5           |
| 2.1.1 Ferroelectricity.....   | 5           |
| 2.1.2 Piezoelectricity.....   | 8           |
| 2.2 Ferromagnetism and Magnetostriction .....                               | 10          |
| 2.2.1 Ferromagnetism .....  | 10          |
| 2.2.2 Magnetostriction .....  | 11          |
| 2.3 Multiferroic and Ferroelectromagnetic Thin Films .....                  | 13          |
| 2.3.1 Single-Phase Multiferroic Thin Films .....                            | 13          |
| 2.3.2 Composite Multiferroic Thin Films .....                               | 14          |
| 2.4 PbTiO <sub>3</sub> -CoFe <sub>2</sub> O <sub>4</sub> system.....        | 17          |
| 2.4.1 PbTiO <sub>3</sub> Structure and Property .....                       | 17          |
| 2.4.2 CoFe <sub>2</sub> O <sub>4</sub> Structure and Properties.....        | 20          |
| 2.4.3 PbTiO <sub>3</sub> -CoFe <sub>2</sub> O <sub>4</sub> System .....     | 22          |
| <b>Chapter 3: Thin Film Deposition and Characterization .....</b>           | <b>24</b>   |
| 3.1 Pulsed Laser Deposition .....   | 24          |
| 3.1.1 Mechanism of Pulsed Laser Deposition .....                            | 26          |
| 3.1.2 Features of Pulsed Laser Deposition.....                              | 28          |
| 3.2 X-Ray Diffraction (XRD).....  | 29          |
| 3.3 Transmission Electron Microscopy (TEM) .....                            | 30          |
| 3.4 Scanning Electron Microscopy (SEM).....                                 | 31          |
| 3.5 Atomic Force Microscopy (AFM).....                                      | 33          |
| 3.6 Superconductor Quantum Interference Device (SQUID).....                 | 36          |
| 3.7 Electrical Measurement .....  | 39          |
| <b>Chapter 4: Multiferroic Nanostructures in Epitaxial Films .....</b>      | <b>41</b>   |
| 4.1 PbTiO <sub>3</sub> - CoFe <sub>2</sub> O <sub>4</sub> Film Growth ..... | 41          |
| 4.2 Structure Characterization .....  | 43          |

|  |           |
|--|-----------|
| 4.2.1 XRD Characterization.....  | 43        |
| 4.2.2 TEM Characterization.....  | 49        |
| 4.3 Discussion of Formation of Self-Assembling Two-Phase Nanostructures..... | 58        |
| <b>Chapter 5: Property Characterization .....</b>                            | <b>64</b> |
| 5.1 Ferroelectric Properties.....  | 64        |
| 5.1.1 Polarization Measurement .....   | 64        |
| 5.1.2 Piezoelectric Properties.....  | 66        |
| 5.2 Ferromagnetic Properties.....  | 70        |
| 5.3 Tuning magnetic easy axial from in-plane to out-of-plane.....            | 75        |
| <b>APPENDIX.....</b>   | <b>80</b> |
| <b>REFERENCE.....</b>  | <b>90</b> |

## LIST OF TABLES

|  |          |
|--|----------|
| Table 2.1: Material constants for $\text{PbTiO}_3$ at room temperature                       | -----23  |
| Table 4.1: Typical processing parameters used in the thin film deposition                    | ----- 46 |
| Table 4.2: Out-of-plane d-spacing of $\text{CoFe}_2\text{O}_4$ - $\text{PbTiO}_3$ thin film- | ----- 49 |
| Table 5.1: Parameters of magnetic hysteresis loop-   | ----- 78 |

## LIST OF FIGURES

|         |   |          |
|---------|---|----------|
| Fig.2.1 | Hysteresis loop showing polarization switching in ferroelectric materials.- -<br>-----  | -11      |
| Fig.2.2 | Schematic illustration of direct and converse piezoelectric effects- - - -  | 13       |
| Fig.2.3 | Hysteresis loop showing magnetization switching in ferromagnetic<br>materials- - - - -  | -16      |
| Fig.2.4 | Schematic illustration of magnetostriction.- - - - -  | 16       |
| Fig.2.5 | A) Schematic illustration of a heterostructures consisting of alternating<br>ferroelectric and ferromagnetic layers on a substrate - - - - -<br>B) Schematic illustration of a transverse thin film heterostructure<br>consisting of pillars of one phase embedded in a matrix of the other<br>phase on a substrate - - - - - | 20<br>20 |
| Fig.2.6 | Schematic of the cubic perovskite structure - - - - -   | -22      |
| Fig.2.7 | Schematic of the spinel structure, showing octahedral and tetrahedral sites<br>occupied by the A and B cations. - - - - -   | 25       |
| Fig.3.1 | Schematic illustration of a Pulsed Laser Deposition system-- - - - -  | -29      |
| Fig.3.2 | Schematic of nucleation and growth of crystals on a substrate- - - - -  | 31       |
| Fig.3.3 | Schematic illustration of electron/specimen interactions - - - - -  | 36       |
| Fig.3.4 | Schematic illustration of the PFM setup- - - - -  | -39      |
| Fig.3.5 | Schematic illustration of the SQUID setup- - - - -  | -42      |
| Fig.3.6 | A). Schematic of electrical measurement set-up- - - - -<br>B). Pulse train for switching measurements - - - - -   | 44<br>44 |
| Fig.4.1 | X-ray diffraction patterns of $\text{CoFe}_2\text{O}_4$ - $\text{PbTiO}_3$ thin film- - - - -<br>A) (001) orientation of the $\text{SrTiO}_3$ substrate<br>B) (110) orientation of the $\text{SrTiO}_3$ substrate   | 48       |

C) (111) orientation of the SrTiO<sub>3</sub> substrate

|          |   |    |
|----------|---|----|
| Fig.4.2  | Phi scan of the 0.33CoFe <sub>2</sub> O <sub>4</sub> -0.67PbTiO <sub>3</sub> thin film grown on (001) SrTiO <sub>3</sub> substrate -----  | 49 |
| Fig.4.3  | Effective out-of-plane lattice spacing as function of temperature for the (001) film 0.33CoFe <sub>2</sub> O <sub>4</sub> -0.67PbTiO <sub>3</sub> - -----   | 52 |
| Fig.4.4  | Selected area electron diffraction patterns of the 0.33CoFe <sub>2</sub> O <sub>4</sub> -0.67PbTiO <sub>3</sub> film grown on SrTiO <sub>3</sub> substrates having the following crystallographic orientations: a) (001), b) (110), c) (111). -----   | 54 |
| Fig.4.5  | TEM plane view and cross-section dark field images of the 0.33CoFe <sub>2</sub> O <sub>4</sub> -0.67PbTiO <sub>3</sub> films grown on differently oriented SrTiO <sub>3</sub> substrates: a) (001); b) (110); c) (111) -----  | 55 |
| Fig.4.6  | a) Magnified TEM cross-sectional image of the 0.33CoFe <sub>2</sub> O <sub>4</sub> -0.66PbTiO <sub>3</sub> film grown on (001) SrTiO <sub>3</sub> ; b) HRTEM image of the CoFe <sub>2</sub> O <sub>4</sub> /PbTiO <sub>3</sub> interface in the same cross-sectional sample; c) HRTEM image of CoFe <sub>2</sub> O <sub>4</sub> -----   | 57 |
| Fig.4.7  | Representative EELS spectra recorded from the CoFe <sub>2</sub> O <sub>4</sub> and PbTiO <sub>3</sub> phases. The presence of Ti in the CoFe <sub>2</sub> O <sub>4</sub> and of Fe in the PbTiO <sub>3</sub> was additionally confirmed by recording separate EELS spectra with the microscope energy offsets corresponding to the Ti-L <sub>2,3</sub> (450 eV) and Fe-L <sub>2,3</sub> (710 eV) edges, respectively. ----- | 58 |
| Fig.4.8  | TEM dark field images of the 0.33PbTiO <sub>3</sub> -0.67CoFe <sub>2</sub> O <sub>4</sub> films on differently oriented SrTiO <sub>3</sub> substrates a) (001); b) (110); c) (111)- -----   | 60 |
| Fig.4.9  | SEM plane-view images: a)-c)0.67PbTiO <sub>3</sub> -0.33CoFe <sub>2</sub> O <sub>4</sub> on a)-(001), b)-(110) and c)-(111) SrTiO <sub>3</sub> ; d)-f) 0.57 PbTiO <sub>3</sub> -0.43CoFe <sub>2</sub> O <sub>4</sub> on d)-(001), e)-(110), and f)-(111) SrTiO <sub>3</sub> ; g)-i) 0.33PbTiO <sub>3</sub> -0.67CoFe <sub>2</sub> O <sub>4</sub> on g)-(001), h)-(110), and i)-(111) SrTiO <sub>3</sub> . -----             | 61 |
| Fig.4.10 | Schematic drawings of a)-b) a coherent two-phase structure on a substrate, c)-d) semi-coherent structure with the inter-phase boundaries partially relaxed along the normal to the substrate, e)-f) semi-coherent structure with  |    |

|          |  |     |
|----------|--|-----|
|          | a partially relaxed film/substrate interface.-----   | -63 |
| Fig.4.11 | Top-view of TEM images of the epitaxial $0.33\text{CoFe}_2\text{O}_4\text{-}0.67\text{PbTiO}_3$ (a-c) and $0.67\text{CoFe}_2\text{O}_4\text{-}0.33\text{PbTiO}_3$ (e-f) films grown on $\text{SrTiO}_3$ substrates having the following orientations: a), d)-(001), b), e)-(110), and c), f)-(111).-----   | 67  |
| Fig.5.1  | Polarization hysteresis loop of the $0.66\text{PbTiO}_3\text{-}0.33\text{CoFe}_2\text{O}_4$ thin film grown on (001) $\text{SrTiO}_3$ -----  | 69  |
| Fig.5.2  | $d_{zz}$ loop for the $0.67\text{PbTiO}_3\text{-}0.33\text{CoFe}_2\text{O}_4$ thin film grown on differently oriented $\text{SrTiO}_3$ substrates: a) (001), b) (110), c) (111)-----   | -71 |
| Fig.5.3  | The color maps showing the strain distributions in multiferroic nanostructures in $0.33\text{CoFe}_2\text{O}_4\text{-}0.67\text{PbTiO}_3$ on differently oriented substrates.-----   | 73  |
| Fig.5.4  | Piezoresponce of differently oriented $\text{PbTiO}_3$ : single crystal (bulk) (white circles), theoretic calculations for continues film (triangles), phase field modeling results for multiferroic films ( $0.33\text{CoFe}_2\text{O}_4\text{-}0.67\text{PbTiO}_3$ ) (rhombs), experimental measurements of the multiferroic films with the same composition (black circles).----- | 73  |
| Fig.5.5  | Magnetization hysteresis loop for the $0.67\text{PbTiO}_3\text{-}0.33\text{CoFe}_2\text{O}_4$ film grown on differently oriented $\text{SrTiO}_3$ : a) (001), b) (110), c) (111)-----  | 76  |
| Fig.5.6  | Magnetization hysteretic loop for the $0.33\text{PbTiO}_3\text{-}0.67\text{CoFe}_2\text{O}_4$ film grown on differently oriented $\text{SrTiO}_3$ : a) (001), b) (110), c) (111)-----  | 77  |
| Fig.5.7  | Magnetization hysteresis loop of $0.67\text{PbTiO}_3\text{-}0.33\text{CoFe}_2\text{O}_4$ with the $\text{CoFe}_2\text{O}_4$ pillars having the aspect ratio of $\sim 35$ as compared to $\sim 5$ , as shown in Fig. 6.3-----   | 80  |
| Fig.5.8  | TEM dark-field images of the $0.67\text{PbTiO}_3\text{-}0.33\text{CoFe}_2\text{O}_4$ film with the $\text{CoFe}_2\text{O}_4$ nano-pillars, having a height-to-diameter ratio of 35, embedded in the $\text{PbTiO}_3$ matrix. a) plane view; b) cross-section-----  | -80 |

# Chapter 1: Motivation and Objectives of Research

Multiferroic materials which display a coexistence of ferroelectric and ferromagnetic properties attract considerable interest for their potential for novel device applications as well as for the interesting physics and materials science underlying their functional responses.

Natural multiferroic single-phase crystals are rare and exhibit relatively weak magnetic and electrical responses as well as weak coupling between the electric and magnetic fields [1-6]. In contrast, two-phase ceramic laminate composites, which incorporate both ferroelectric and ferri-/ferromagnetic components, typically yield strong direct responses to electric or magnetic fields. However, the magnetoelectric (ME) coupling in such composites, which is strain-mediated due to piezoelectric and magnetostriction effects, is still relatively weak being limited by the mechanical adhesion of the component phases [7-18]. The efficiency of the ME coupling can be increased in the so called *in situ* composites which represent a product of the phase transformation. The first attempt to fabricate a multiferroic composite through the eutectic crystallization of the mixture of BaTiO<sub>3</sub> and CoFe<sub>2</sub>O<sub>4</sub> was reported by J. Van Suchtelen in 1972 [7]. However, the multiferroic properties of these microscopic self-assembled composites were still limited by the imperfections of the mechanical bonding across the phase boundaries.

On the other side, the thermodynamic theory of heterophase thin film nanostructures predicts formation of self-organized periodic heterophase structures as

a result of phase transformations in constrained films [19]. In particular, this theory suggests that self-assembled nanostructures can be formed as result of a eutectic transformation on a single crystal substrate [20].

Recently, these ideas were realized in the multiferroic heterostructures consisting of ferroelectric BaTiO<sub>3</sub> and ferromagnetic CoFe<sub>2</sub>O<sub>4</sub> grown on the (001) SrTiO<sub>3</sub> substrates [17, 18, 20]. These self-assembled nanocomposite films exhibited a 3-D epitaxy between phases and between each phase and a substrate, featured hexagonal arrays of CoFe<sub>2</sub>O<sub>4</sub> nanopillars (20nm-30nm diameters) embedded in a BaTiO<sub>3</sub> matrix. Measurements of temperature dependence of magnetization revealed strong coupling between the ferroelectric and magnetic order parameters, which was manifested as change in magnetization at the ferroelectric Curie temperature; the magnitude of this change was consistent with the predictions of a thermodynamic theory which assumed a perfect elastic coupling among the component phases. No strain-coupling has been observed for the layered CoFe<sub>2</sub>O<sub>4</sub>/BaTiO<sub>3</sub> heterostructures. It has confirmed that the clamping effect of a substrate effectively suppresses strain interactions for the multilayer composite architectures. In contrast, in the transversely modulated two-phase heterostructures, having inter-phase boundaries perpendicular to the substrate, the clamping effects are minimized thus yielding strong elastic coupling and the associated ME response. As suggested in [21], the self-assembling of the phases during growth is also driven by the epitaxial elastic interactions so that the resulting nanostructure morphologies can be treated in the framework of a thermodynamic theory of elastic domains.

According to this approach, the self-assembly and the resulting morphologies of epitaxial two-phase nanostructures can be predicted and controlled via the stress conditions in the film during growth by varying, for example, a lattice misfit of the component phases or by varying the in-plane elastic anisotropy of the film. The major goal of our research is a realization of this idea with the ultimate objective to design transverse epitaxial multiferroic nanostructures with controlled morphologies. The  $\text{PbTiO}_3\text{-CoFe}_2\text{O}_4$  system was selected for this study because of the (i) large spontaneous strain associated with the ferroelectric phase transition in  $\text{PbTiO}_3$  (6.5%), and large piezoeffect which should create strong elastic interactions between the two phases, and (ii) large magnetostriction of ferrimagnetic  $\text{CoFe}_2\text{O}_4$ . The composite films with different phase fractions were grown on  $\text{SrTiO}_3$  substrates having different crystallographic orientations, to modify the stress conditions during growth. To achieve the research objective, the two-phase nanostructures were grown on single crystal  $\text{SrTiO}_3$  having (001), (110), and (111) orientations. Our results demonstrate that regardless of substrate orientation, the nanostructures exhibited a 3-D epitaxy and consisted of vertical columns of either ferromagnetic  $\text{CoFe}_2\text{O}_4$  dispersed in the ferroelectric  $\text{PbTiO}_3$  matrix, or vice versa. However, the morphologies of these columns, and their spatial arrangements, exhibited a marked dependence on the substrate orientation. Comparison with theoretical analysis and modeling allows us to conclude that the differences in nanostructure morphologies arise mainly from elastic anisotropy of the film. The evolution of internal stresses, developed in the nanostructures upon the cubic-tetragonal transition in  $\text{PbTiO}_3$ , was analyzed using high-temperature X-ray diffraction, and a strong elastic coupling was confirmed.

Multifunctional ferroelectric and ferromagnetic properties have been explored to demonstrate their correlation with nanostructure morphology.

The content of this thesis is following:

General physical background is presented in Chapter 2. Deposition and characterization methods are discussed in Chapter 3. Fabrication and characterization of  $\text{PbTiO}_3\text{-CoFe}_2\text{O}_4$  thin film nanostructures on differently orientated substrates and theoretical discussion of nanostructure morphology are presented in Chapter 4. The ferroelectric and ferromagnetic properties are presented in Chapter 5. After Conclusions as Appendix we present the results of our theoretical study of piezoeffect in constrained films.

# Chapter 2. Physical Background

## *2.1 Ferroelectricity and Piezoelectricity*

### **2.1.1 Ferroelectricity**

Ferroelectrics are materials that possess at least two equilibrium orientations of the spontaneous polarization vector in the absence of an external electric field, and in which the spontaneous polarization vector may be switched between those orientations by an electric field [22]. There are two main types of a ferroelectric behavior: displacive and order-disorder. The displacive type is due to an ion being displaced from the equilibrium position, and hence acquiring a permanent dipole moment. At high temperatures ( $T > T_c$ , where  $T_c$  is a ferroelectric Curie temperature), the thermal energy is sufficient to allow the ions to move randomly from one position to another, so there is no fixed asymmetry. When the temperature is below  $T_c$ , the ion is frozen in an off-center position giving rise to a net dipole moment. In an order-disorder ferroelectric, there is a dipole moment in each unit cell, but at high temperatures they are pointing in random directions. Upon lowering the temperature, the dipoles order and become aligned in the same direction within a single domain.

According to their symmetry, crystals can be divided into the 32 point groups with 11 of them being centro-symmetric (non-polar) and 21 lacking an inversion center (polar). Lack of inversion center is a pre-requisite for the piezoelectric behavior of the crystal. The crystal lacking a centre of symmetry will have a net

displacement of the positive and negative ions with respect to each other resulting in an electric dipole, whereas, for the centro-symmetric crystals, the centers of the two opposite charges will always coincide, so there is no electric dipole generated. Out of the twenty piezoelectric classes, only ten, possessing a unique polar axis which can be spontaneously polarized, belong to ferroelectrics.

Ferroelectric hysteresis loop (Fig.2.1) is the characteristic of a ferroelectric material, which arises due to the presence of ferroelectric domains in the crystal. Application of an external dc electric field  $E > E_c$  to a polydomain ferroelectric crystal, causes the polarization,  $P$ , vectors having different orientations in different domains to align themselves parallel to the direction of the field via domain wall movement. The minimum dc field required to move the domain walls is a measure of the coercive field. The initial value of  $P_s$  in a polydomain crystal increases with increasing dc field to a maximum that is characteristic of the material. Reversing the electric field reintroduces domain walls movement and results in the  $P_s$  in different regions to be reversed. At zero applied field, the crystal will have a remnant polarization which is smaller than the spontaneous polarization. At fully reversed field, the final  $P_s$  will have the same magnitude as the original  $P_s$  but the opposite sign. The hysteretic loop is a function of the work required to displace the domain walls which is closely related to the defect distribution in the crystal and to the energy barrier separating the different orientational states.

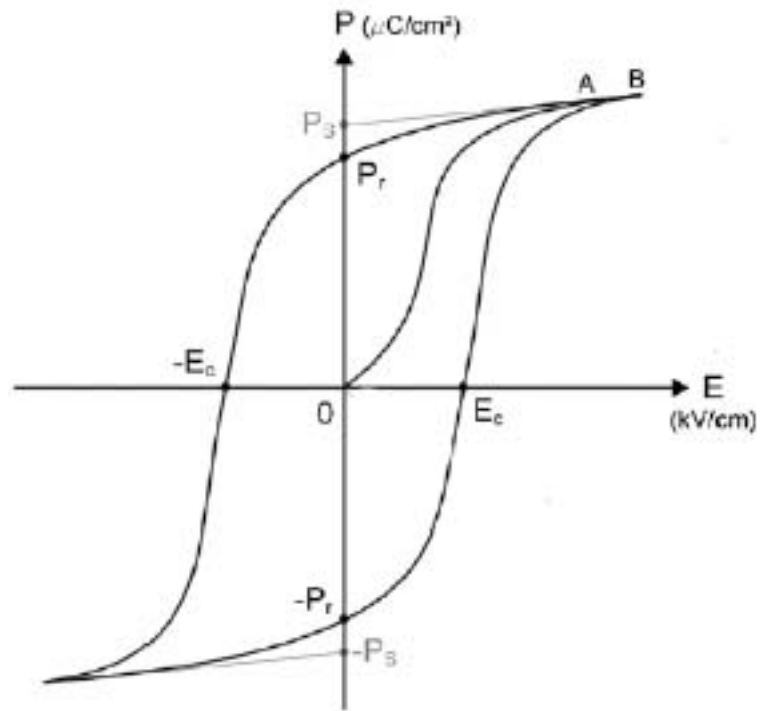


Figure 2.1 Hysteresis loop showing polarization switching in ferroelectric materials. Important parameters such as coercive field ( $E_c$ ), remnant polarization ( $P_r$ ) and saturation polarization ( $P_s$ ) are indicated in the figure.

### 2.1.2 Piezoelectricity

All ferroelectric crystals are necessarily piezoelectric. The piezoelectric effect is a phenomena resulting from a coupling between the electrical and mechanical properties of a material. When mechanical stress is applied to a piezoelectric material, an electric potential will be generated. Likewise, when an electric potential is applied to the material, a mechanical strain will occur.

The basic equations that describe these two effects in regard to electric and elastic properties are:

$$D_i = \varepsilon_{ij}^T E_j + d_{ijk} T_{jk}$$

$$S_{ij} = d_{ijk} E_k + S_{ijkl}^E T_{kl}$$

where,  $D$  is the dielectric displacement vector,  $E$  is the electric field vector,  $T$  is the mechanical stress tensor,  $S$  is the mechanical strain tensor,  $d$  is the tensor of piezoelectric constants,  $\varepsilon$  is the tensor of dielectric constants (superscript  $T$  indicates a constant stress),  $s$  is the tensor of mechanical compliance (superscript  $E$  indicates a constant electric field) [23].

Recently, a comprehensive study of the orientation dependence of piezoelectric properties in epitaxial ferroelectric thin films has been reported [24, 25], which included both theoretical and experiment results on the intrinsic and extrinsic piezoelectric properties of epitaxial ferroelectric films.

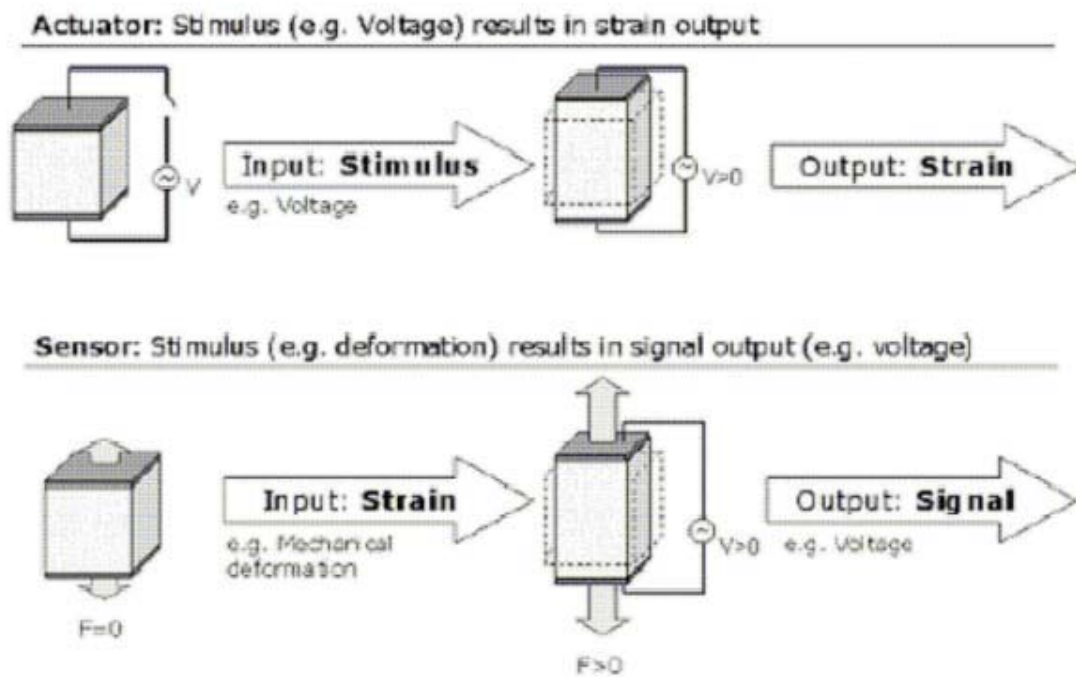


Fig.2.2 Schematic illustration of direct and converse piezoelectric effects. Figures adapted from ref. [26].

## ***2.2 Ferromagnetism and Magnetostriction***

### **2.2.1 Ferromagnetism**

Ferromagnetism is a phenomenon which describes materials exhibiting spontaneous magnetization. Electron spin and the Pauli Exclusion Principle are the physical origin of ferromagnetism. The spin of an electron combined with its orbital angular momentum, results in a magnetic dipole moment and creates a magnetic momentum. Only atoms with partially filled shells with unpaired spins can exhibit a net magnetic moment in the absence of an external field. According to the response to the external magnetic field, the material can be classified into: (i) paramagnetism (PM); (ii) ferromagnetism (FM); (iii) antiferromagnetism (AFM) and (iv) ferrimagnetism (FIM). Paramagnetic materials feature disordered orientations of the magnetic moments due to thermal fluctuations. Ferromagnetism is the strongest form of a magnetic response which is characterized by the parallel alignment of adjacent magnetic moments. In contrast, an antiferromagnetic behavior corresponds to an antiparallel alignment of equal moments. Finally, a ferrimagnetism is characterized by antiparallel moments having different magnitudes and thus yielding a non-zero net magnetization.

Both ferro- and ferrimagnetics exhibit a hysteretic response to an external magnetic field, as shown in Fig. 2.3. The saturation magnetization ( $M_s$ ), coercive field ( $H_c$ ) and remnant magnetization ( $M_r$ ) are all shown in the figure. Based on the value of a coercive field, magnetic materials are classified into hard (large  $H_c$ ) and soft (small  $H_c$ ) magnets.

To explain the spontaneous alignment of the spins and the hysteresis loops developed in the ferromagnetic materials, Weiss proposed that (1) there is a strong

internal magnetic field (proportional to the magnetic moment) which aligns the dipoles even without an external field; and (2) macroscopically, there are small regions, called domains, which are spontaneously magnetized. The magnetic moment of the entire specimen is then a vector sum of the magnetic moments in all domains. Since the directions of magnetization in different domains are not, certain domain configurations produce a zero net moment. The application of a relatively small external magnetic field changes the domain arrangement, and hence induces an appreciable change in net magnetization. Domain switching under external field produces hysteresis loops.

### **2.2.2 Magnetostriction**

Ferromagnetic materials respond mechanically to an external magnetic field, by changing length in the direction of the applied field. This phenomenon is called magnetostriction. A magnetostrictive material will change its shape when subjected to a magnetic field.

The mechanism of magnetostriction involves two separate processes: 1) Domain wall migration in response to an external magnetic field; 2) Domain rotation. These two mechanisms change the domain orientation which in turn causes a dimensional change as shown in Fig. 2.4.

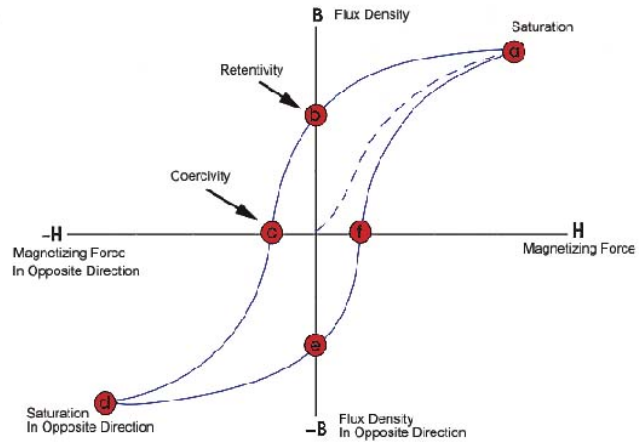


Fig.2.3 Hysteresis loop showing magnetization switching in ferromagnetic materials.

Figure adapted from ref. [27].

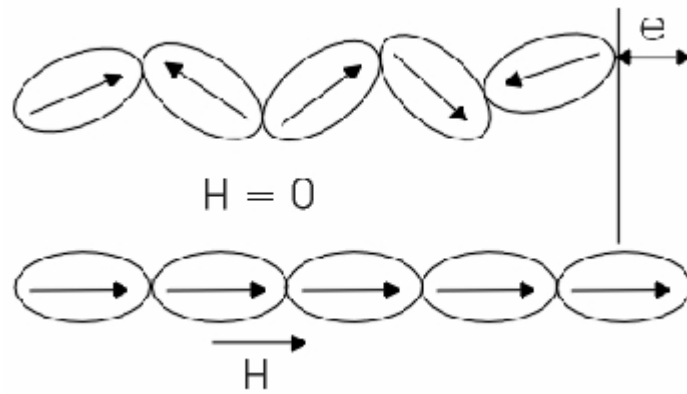


Fig.2.4 Schematic illustration of magnetostriction.

### ***2.3 Multiferroic and Ferroelectromagnetic Thin Films***

The term multiferroic is used to describe materials in which two or all three of the ferro-properties, ferroelectricity, ferro/ferrimagnetism, and ferroelasticity – occur simultaneously. Specific device applications that have been suggested for such materials include multiple-state memory elements, magnetic field sensors, electric-field-controlled ferromagnetic resonance devices, and transducers with magnetically modulated piezoelectricity. More of the possible applications of multiferroic materials can be found in the previous review articles [28, 29]. Ferroelectromagnetic material which features a coexistence of ferroelectric and ferromagnetic responses represents a subclass of multiferroics. A ferroelectric polarization can be switched by a magnetic field and a magnetization can be switched by an electric field.

#### **2.3.1 Single-Phase Multiferroic Thin Films**

Multiferroic thin films featuring single-phase compounds, such as  $\text{BiMnO}_3$ [30,31,32],  $\text{BiFeO}_3$ [33,34],  $\text{YMnO}_3$ [35-40], have been developed; however, none of them exhibited a combination of strong ferroelectric and ferromagnetic responses. Such weak multiferroic responses in single-phase compounds have been attributed to the mutually exclusive requirements for the d-electron configurations imposed by the ferroelectricity and ferromagnetism [41].

### 2.3.2 Composite Multiferroic Thin Films

Today, the advanced processing technology offers a possibility of implementing the multiferroic composites, consisting of the ferro/ferrimagnetic and ferroelectric phases, in thin films. The composite two-phase films can be realized in two distinct architectures:

#### a) Layered Heterostructures

Multiferroic layered heterostructures can be obtained using a layer-by-layer growth of the ferroelectric and ferromagnetic phases on a substrate. A series of composition spreads, consisting of ferroelectric BaTiO<sub>3</sub> and ferrimagnetic CoFe<sub>2</sub>O<sub>4</sub> layers of varying thicknesses modulated at the nanometer level have been reported [11]; however, no clear evidence of a multiferroic behavior was established. Attempts to generate multilayer compositional spreads in the PbTiO<sub>3</sub>-CoFe<sub>2</sub>O<sub>4</sub> system on (001) MgO [42] produced certain compositions with a pancake-like inclusions of PbTiO<sub>3</sub> in a matrix of CoFe<sub>2</sub>O<sub>4</sub> which exhibited substantial ME tunability; yet these results also remained largely inconclusive with respect to the mechanism of the ME coupling observed. Multilayers composed of ferromagnetic Pr<sub>0.85</sub>Ca<sub>0.15</sub>MnO<sub>3</sub> and ferroelectric Ba<sub>0.6</sub>Sr<sub>0.4</sub>TiO<sub>3</sub> layers on (100) SrTiO<sub>3</sub> substrates were grown [12,13,14] by Murugavel *et al* using a pulsed laser deposition technique. Both ferromagnetic and ferroelectric transitions were observed in these superlattices. The high magnetoresistance (40% at 80 K) observed for the superlattice with the ten unit cells of Pr<sub>0.85</sub>Ca<sub>0.15</sub>MnO<sub>3</sub> and nine unit cells of Ba<sub>0.6</sub>Sr<sub>0.4</sub>TiO<sub>3</sub> has been attributed to the coupling between ferromagnetic and ferroelectric layers, i.e., to the magnetoelectric effect [13]; however, the interpretations given in this work were

largely speculative. Currently, the only viable mechanism of ME coupling which can provide responses ME responses strong enough for practical applications is related to a strain-coupling among the piezoelectric and magnetostrictive components of a heterostructure [43]. The magnetoelectric effect was also observed in micrometer-size sputtered composites [44]. However, for the multilayer architecture the clamping effect of the substrate effectively suppresses any in-plane strain in the film. This clamping effect will be minimized in a transverse composite architecture with the inter-phase boundaries being perpendicular to the substrate, as described below.

#### b) Transverse Heterostructures

Recently, self-assembled epitaxial multiferroic  $\text{BaTiO}_3\text{-CoFe}_2\text{O}_4$  nanostructures grown on single-crystal (001)  $\text{SrTiO}_3$  have been reported.  $\text{CoFe}_2\text{O}_4$  (spinel) and  $\text{BaTiO}_3$  (perovskite) phases undergo spontaneous separation during heteroepitaxial growth and self-assemble on a  $\text{SrTiO}_3$  substrate. The resulting nanostructures featured arrays of  $\text{CoFe}_2\text{O}_4$  nanopillars distributed in a  $\text{BaTiO}_3$  matrix [17, 20]. The diameter of the pillars increased with the increasing growth temperature following the Arrhenius behavior. These nanostructures were confirmed to exhibit a strong ME coupling which was attributed to very efficient elastic interactions among the component phases due to (1) coherent interfaces and (2) reduced clamping by the substrate.

The  $\text{BaTiO}_3\text{-CoFe}_2\text{O}_4$  thin films grown on various substrates, such as  $\text{LaAlO}_3$  (001),  $\text{MgAl}_2\text{O}_4$  (001),  $\text{MgO}$  (001), and  $\text{SrTiO}_3$  (001), exhibited similar  $\text{CoFe}_2\text{O}_4$  nanopillars which indicated that the lattice mismatch with the substrate has no effect on the nanostructure morphologies [20].

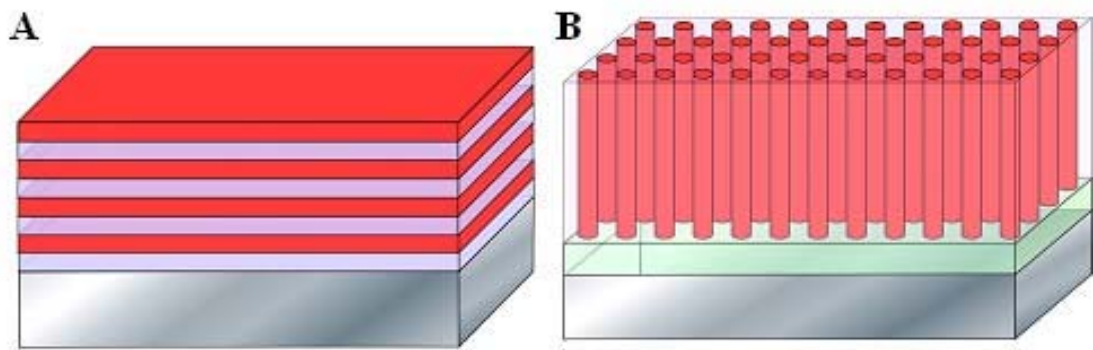


Fig.2.5 A) Schematic illustration of a heterostructures consisting of alternating ferroelectric and ferromagnetic layers on a substrate B) Schematic illustration of a transverse thin film heterostructure consisting of pillars of one phase embedded in a matrix of the other phase on a substrate Figure adapted from ref. [17].

Similar transverse nanostructures, featuring  $\text{CoFe}_2\text{O}_4$  nanopillars, have been demonstrated for the  $\text{BiFeO}_3\text{-CoFe}_2\text{O}_4$  films grown on (001)  $\text{SrTiO}_3$  substrates. Electric field-induced magnetization switching was studied in  $\text{BiFeO}_3\text{-CoFe}_2\text{O}_4$  system [45]. The results of this study provided the first direct evidence for the room-temperature magnetization reversal induced by an electric field in transverse nanostructure.

## ***2.4 $\text{PbTiO}_3\text{-CoFe}_2\text{O}_4$ system***

### **2.4.1 $\text{PbTiO}_3$ Structure and Property**

$\text{PbTiO}_3$  is a classical displacive ferroelectric material with a highly polar perovskite crystal structure [46, 47]. Its crystal structure is schematically shown in Figure. The  $\text{Pb}^{2+}$  cations are located at the corners of the unit cell,  $\text{O}^{2-}$  anions reside at the face centers; and  $\text{Ti}^{4+}$  cations, above the Curie temperature  $T_c$ , occupy the center of each unit cells. Below  $T_c = 490^\circ\text{C}$ ,  $\text{PbTiO}_3$  undergoes a cubic-to-tetragonal first-order phase transformation accompanied by off-center displacements of the  $\text{Ti}^{4+}$  cations being which generate a net dipole moment. Under ambient conditions,  $\text{PbTiO}_3$  acquired a tetragonal symmetry (space group  $P4mm$ ) with the spontaneous polarization vector being parallel to the  $c$ -axis. The properties of tetragonal  $\text{PbTiO}_3$  single crystal has been studied both theoretical and experimentally as shown in Table 2.1.

$\text{PbTiO}_3$  thin films have been studied intensively due to numerous applications which utilize their unique dielectric, pyroelectric, acousto-optic, and piezoelectric properties [48]. Examples of applications of the  $\text{PbTiO}_3$ -based thin films include

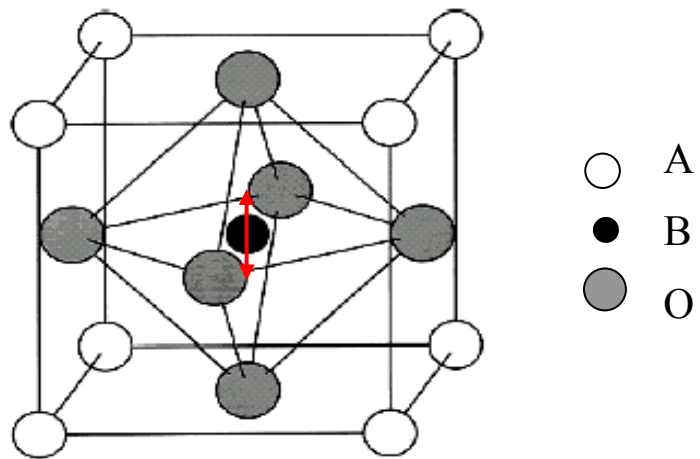


Fig.2.6 Schematic of the cubic perovskite structure. The large A cations (white) occupy the unit cell corners. The small B cation (in black) is at the center of an octahedron of oxygen anions (in gray). Picture adapted from ref. [20].

Table 2.1 Material constants for tetragonal  $\text{PbTiO}_3$  at room temperature

|  | This study            |                       | Literature values    |                      |                      |                      |                      |                      |
|--|-----------------------|-----------------------|----------------------|----------------------|----------------------|----------------------|----------------------|----------------------|
|  | Set A RMSD = 76.7 m/s | Set B RMSD = 79.1 m/s | Ref. 52 <sup>a</sup> | Ref. 53 <sup>b</sup> | Ref. 49 <sup>c</sup> | Ref. 54 <sup>d</sup> | Ref. 50 <sup>e</sup> | Ref. 51 <sup>f</sup> |
| <u>Elastic stiffness constants (GPa)</u>                                 |                       |                       |                      |                      |                      |                      |                      |                      |
| $C_{11}^E$   | 237 ± 3               | 237 ± 3               | 235 ± 3              | 133                  |                      |                      |                      |                      |
| $C_{33}^E$   | 60 ± 10               | 90 ± 10               | 105 ± 7              | 93                   |                      |                      |                      |                      |
| $C_{44}^E$   | 69 ± 1                | 69 ± 1                | 65 ± 1               | 80                   |                      |                      |                      |                      |
| $C_{66}^E$   | 104 ± 1               | 104 ± 1               | 104 ± 1              | 93                   |                      |                      |                      |                      |
| $C_{12}^E$   | 90 ± 5                | 90 ± 5                | 101 ± 5              | 85                   |                      |                      |                      |                      |
| $C_{13}^E$   | 70 ± 10               | 100 ± 10              | 99 ± 8               | 89                   |                      |                      |                      |                      |
| <u>Elastic compliance constants (<math>10^{-3}/\text{GPa}</math>)</u>    |                       |                       |                      |                      |                      |                      |                      |                      |
| $S_{11}^E$   | 6.5                   | 8.2                   | 7.1                  |                      | 7.2                  |                      |                      |                      |
| $S_{33}^E$   | 33.3                  | 34.7                  | 21.3                 |                      | 32.5                 |                      |                      |                      |
| $S_{44}^E$   | 14.5                  | 14.5                  | 15.4                 |                      | 12.2                 |                      |                      |                      |
| $S_{66}^E$   | 9.6                   | 9.6                   | 9.6                  |                      | 7.9                  |                      |                      |                      |
| $S_{12}^E$   | -0.35                 | 1.4                   | -0.4                 |                      | -2.1                 |                      |                      |                      |
| $S_{13}^E$   | -7.1                  | -10.6                 | -6.3                 |                      | ...                  |                      |                      |                      |
| <u>Piezoelectric strain constants (<math>10^{-11}</math> C/N)</u>        |                       |                       |                      |                      |                      |                      |                      |                      |
| $d_{15}$   | 6.38                  | 6.96                  | 6.0                  | 4.6                  | 6.5                  | 5.6                  |                      |                      |
| $d_{31}$   | -2.28                 | -4.99                 | -2.8                 | -1.5                 | -2.5                 | -2.3                 |                      |                      |
| $d_{33}$   | 13.66                 | 15.64                 | 8.4                  | 5.1                  | 11.7                 | 8.0                  |                      |                      |
| <u>Piezoelectric stress constants (<math>\text{C}/\text{m}^2</math>)</u> |                       |                       |                      |                      |                      |                      |                      |                      |
| $e_{15}$   | 4.4                   | 4.8                   | 3.9                  |                      |                      |                      |                      |                      |
| $e_{31}$   | 2.1                   | -0.67                 | 0.98                 |                      |                      |                      |                      |                      |
| $e_{33}$   | 5.0                   | 4.1                   | 3.4                  |                      |                      |                      |                      |                      |
| <u>Dielectric constants</u>  |                       |                       |                      |                      |                      |                      |                      |                      |
| $K_{11}^T$   | 134                   | 139                   | 130                  |                      | 210                  | 130                  | 135 ± 5              |                      |
| $K_{33}^T$   | 100                   | 114                   | 101                  |                      | 126                  | 120                  | 107 ± 3              |                      |
| $K_{11}^S$   | 102                   | 102                   | 80                   |                      | 115                  | 100                  | 102 ± 3              |                      |
| $K_{33}^S$   | 34                    | 34                    | 34                   |                      | 51                   | 35                   | 34 ± 1               |                      |

<sup>a</sup>Single-crystal Brillouin measurements.

<sup>b</sup>Lattice dynamics calculations using a rigid ion model.

<sup>c</sup>Single-crystal resonance measurements.

<sup>d</sup>Landau-Ginsburg-Devonshire thermodynamic model.

<sup>e</sup>Single-crystal, high-frequency measurements.

ultrahigh-capacity (i.e., Gbit), non-volatile dynamic random access memories (DRAM) and electro-optic waveguide modulators. Different methods were used to synthesize the  $\text{PbTiO}_3$  polycrystalline thin film, e.g., sol-gel, sputtering, laser ablation, metalorganic chemical-vapor deposition (MOCVD), and the resulting properties of the films have been studied extensively [55-62]. Careful studies of the domain structures in single crystalline  $\text{PbTiO}_3$  thin films grown on different substrates have been reported in ref. [63]. This study demonstrated that the film/substrate lattice mismatch has a critical effect on the thin film microstructure.

#### **2.4.2 $\text{CoFe}_2\text{O}_4$ Structure and Properties**

$\text{CoFe}_2\text{O}_4$  has a cubic inverse spinel structure with lattice parameter  $a = 8.38$  Å. The unit cell of spinel structure contains eight formula units per and consists of 32 oxygen anions and 24 cations. The oxygen atoms form a face-centered cubic array. In  $\text{CoFe}_2\text{O}_4$ , the 16 (out of 32) octahedral B-sites are occupied by the eight  $\text{Co}^{2+}$  and eight  $\text{Fe}^{3+}$  cations, whereas the 8 (out of 64) tetrahedral A-sites are occupied by the  $\text{Fe}^{3+}$  cations.

Cobalt ferrite ( $\text{CoFe}_2\text{O}_4$ ) thin films are considered as promising candidates for microwave devices and high-density recording media applications. Bulk  $\text{CoFe}_2\text{O}_4$  exhibits a relatively large magnetocrystalline anisotropy combined with a large magnetostriction. Epitaxial  $\text{CoFe}_2\text{O}_4$  thin films have been extensively studied. The magnetic behavior depends strongly on the film thickness and stress state. For the film thicknesses less than 7nm, the easy magnetization direction was normal to the film surface, whereas for thicker films, the easy axial was parallel to the film plane

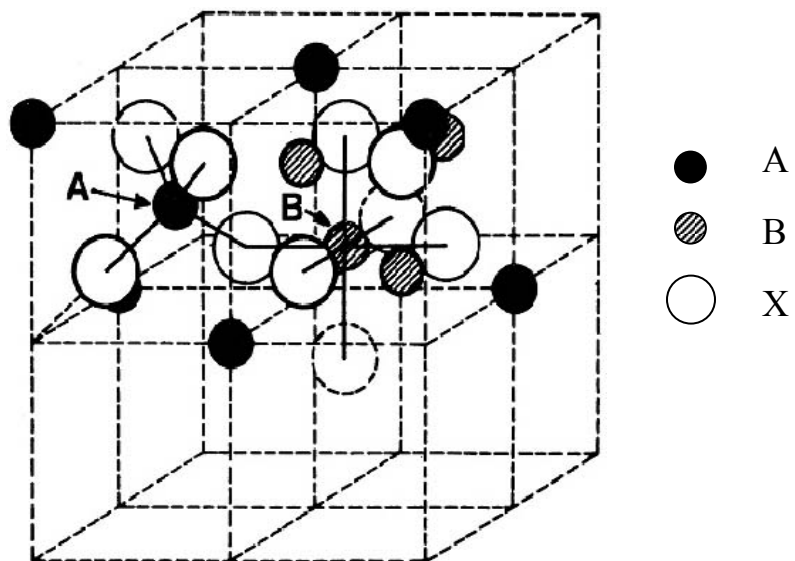


Fig.2.7 Schematic of the spinel structure, showing octahedral and tetrahedral sites occupied by A and B cations.

[64]. The magnetic anisotropy reorientation was also observed in single-crystal  $\text{CoFe}_2\text{O}_4$  thin films deposited on (100) MgO. The as-grown film exhibits an easy direction normal to the film surface, whereas the annealing causes the easy axis to be in the film plane. The origin of such spin reorientation has been attributed to the balance of the magnetoelastic and magnetocrystalline anisotropies. The film as-grown is under tensile stress, which induces a large perpendicular uniaxial anisotropy dominating the in-plane magnetocrystalline component. Annealing releases the stress, thus switching the direction of the easy axis.

### 2.4.3 $\text{PbTiO}_3$ - $\text{CoFe}_2\text{O}_4$ System

The room-temperature lattice parameters of  $\text{PbTiO}_3$  ( $a=3.904 \text{ \AA}$   $c=4.152 \text{ \AA}$ ) are reasonably close to a half of that for  $\text{CoFe}_2\text{O}_4$  ( $a=8.38 \text{ \AA}/2=4.19 \text{ \AA}$ ) as well as to the lattice parameter of  $\text{SrTiO}_3$  ( $a=3.905 \text{ \AA}$ ) which enables a 3-D heteroepitaxy in the  $(\text{PbTiO}_3+\text{CoFe}_2\text{O}_4)/\text{SrTiO}_3$  system. Bulk  $\text{PbTiO}_3$  exhibits a large value of piezoelectric coefficient  $d_{33}=84 \text{ pm/V}$ , whereas  $\text{CoFe}_2\text{O}_4$  features a large magnetostriction coefficient  $\lambda_{001}=-350\times 10^{-6}$ ; that is, the  $\text{PbTiO}_3$ - $\text{CoFe}_2\text{O}_4$  system is expected to yield a strong strain-mediated ME coupling.  $\text{SrRuO}_3$  was chosen as a lattice-matched bottom electrode to facilitate the electrical measurements.

Limited subsolidus phase equilibria data available for the quasi-binary join  $\text{PbTiO}_3$ - $\text{CoFe}_2\text{O}_4$  of the quaternary  $\text{PbO-TiO}_2\text{-CoO-Fe}_2\text{O}_3$  system at  $T=1150^\circ\text{C}$  indicates a three-phase mixture of  $\text{PbTiO}_3$ ,  $\text{CoFe}_2\text{O}_4$ , and  $\text{PbFe}_{12}\text{O}_{19}$ , with all phases featuring limited solid solutions. Yet, previous experiments with perovskite-spinel

systems suggest a possibility of obtaining a two-phase ( $\text{PbTiO}_3+\text{CoFe}_2\text{O}_4$ ) mixture in epitaxial thin films under the typical growth conditions.

# Chapter 3: Thin Film Deposition and Characterization

## *3.1 Pulsed Laser Deposition*

Pulsed Laser Deposition (PLD) is a powerful method for growing thin films and multilayers of complex materials. Figure 3.1 shows a schematic of the NIST PLD system which was used in this study. The system features a multiported stainless steel vacuum chamber with an oil-free pumping system. The chamber contains a target holder capable of rotating and translating the target so that the entire surface of the target is used during the deposition. A heater assembly not only holds the substrate in position, but also keeps the substrate at the required temperature during the deposition. The background gas can be maintained at a certain pressure in the chamber during the deposition. A high-power laser outside of the chamber is used as an external energy source to vaporize materials and grow thin films. Lasers that are commonly used include ArF, KrF excimer lasers (shorter wavelength yields higher energy and therefore a more effective ablation [65]). An excimer laser (KrF) operating at 248 nm was used as the ablating source in this project. The laser beam enters the chamber through a beam delivery system that includes an adjustable focus lens, dual beam path, variable aperture, and variable attenuator.

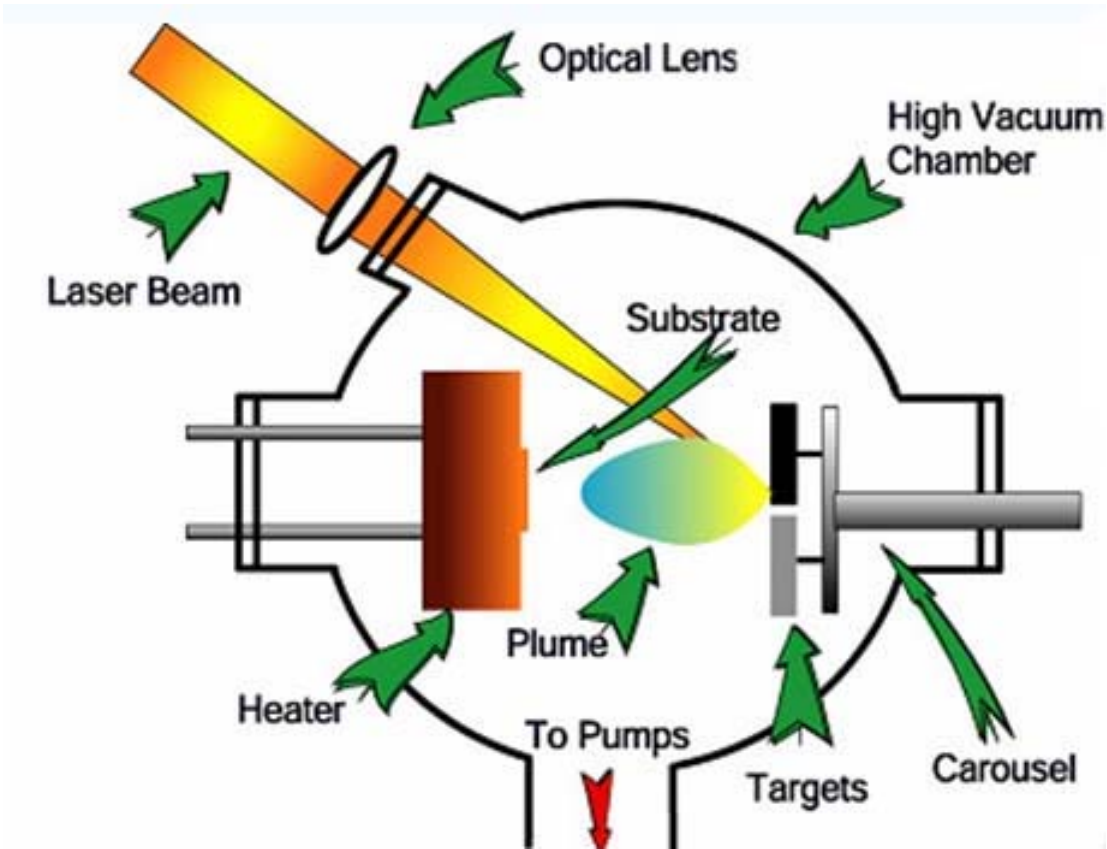


Fig. 3. 1 Schematic illustration of a Pulsed Laser Deposition system.

### 3.1.1 Mechanism of Pulsed Laser Deposition

Pulsed laser deposition is one kind of physical vapor deposition, in which film is formed by atoms directly transported from source to substrate through gas phase.

There are three major physical processes involved in the deposition.

#### 1. Laser beam and target surface interaction.

A pulsed laser beam is focused onto the surface of a metallic or ceramic target by an optical focus lens. The surface layer material of the target is evaporated when the laser energy density (energy per unit area at the target surface) is above a threshold value, forming a plasma plume with high energetic species.

#### 2. Dynamic of the ablation materials

The material evaporated from the target is highly energized and consists of excited and ionized species forming the plasma. The plasma expands away from the target with a strongly forward-directed trajectory toward a heated substrate placed directly in the line of the plume.

#### 3. Film condensation

The dissociated energetic species impinge onto the substrate surface and the mechanism of the interaction is illustrated in Fig. 3.2. An equilibrium is established between the incoming and re-evaporating species depending on the rate of the particles and substrate temperature, which in turn determines the film growth rate. The crystalline film growth depends on the surface diffusion of the atoms. Normally, the atom will diffuse through several atomic distances before sticking to a stable position within the newly formed film. High temperature gives atom high mobility which resulting in rapid and defect free crystal growth, whereas a crystal

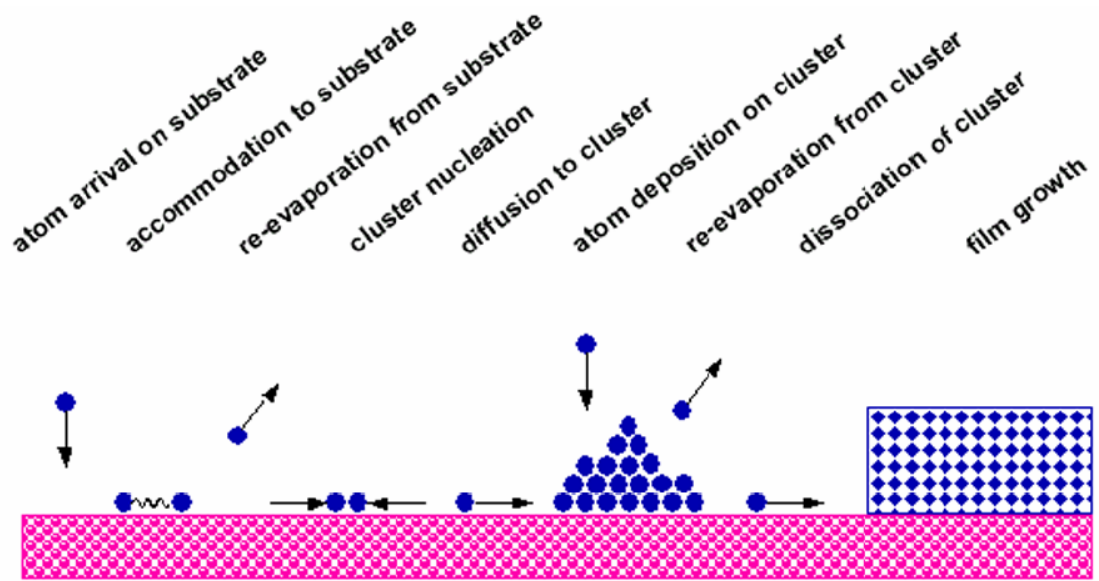


Fig.3.2 Schematic of nucleation and growth of crystals on a substrate.

growth at low temperatures or large super-saturations may be dominated by the energetic particle impingement, resulting in disordered or even amorphous structures.

Each stage in PLD is critical to the formation of high quality thin film in terms of epitaxy, stoichiometry, and surface roughness. Several parameters need to be optimized for specific material growth, such as temperature, laser energy density and frequency, background pressure, and target to substrate distance.

### **3.1.2 Features of Pulsed Laser Deposition**

#### **3.1.2.1 Advantages**

There are several distinct advantages that make the PLD so popular in the thin film research community. The first advantage of PLD is that the stoichiometry of the target can be retained in the deposited films. The laser intensity is on the order of  $10^8$ - $10^9$  W/cm<sup>2</sup> which results in extremely high heating rates of the target surface (108 K/s). The target elements evaporate simultaneously regardless of different evaporating points. The very short duration time of the laser pulse ensures negligible evaporation loss of the target, so that every component of the target phase has a similar deposition rate thus yielding thin films which replicate the target composition.

The second advantage of the PLD is its versatility as all kinds of materials, such as metals, oxide, semiconductor and polymer, can be grown by PLD as long as the laser energy density is high enough to dissociate the target surface material.

The third advantage is economical, because the diameter of the target discs can be very small as long as it is larger than the laser spot which is normally about 2-3 cm<sup>2</sup>.

A further advantage of the PLD process is a relatively low substrate temperature, as compared to other thin film growth techniques, because the dissociated target species are highly energetic. Consequently, even substrate materials with low melting points can be used.

#### 3.1.2.2 Drawbacks

Due to the small laser spot size, the generated plume cross section is very small such that only small size sample can be prepared, and the thickness is not uniform across the sample. Rotating and translating the substrate during growth alleviates this problem to a certain extent. Another drawback is associated with a laser-material ablation which has an intrinsic “splashing”. Droplets or large particles of the target material will be splashed on the substrate surface. This amount of these particulates can be reduced by placing a mechanical shutter in front of the substrate.

### ***3.2 X-Ray Diffraction (XRD)***

X-ray diffraction is a versatile, non-destructive technique to identify the crystalline phases present in solid materials and analyze the structure properties. X-rays are electromagnetic radiation, which is commonly emitted by copper. The characteristic wavelength for the copper  $K\alpha$  radiation is  $1.5418\text{\AA}$ , which is about the same size as an atom. X-ray diffraction is generated from a scattering process in which X-ray scattered by the electrons of the atoms. A diffracted beam is produced by such scattering only when certain geometrical conditions satisfied, which was discovered by Bragg in 1912, and designated as the 'Bragg law':

$$n\lambda = 2d \sin(\theta)$$

where,  $\lambda$  is the wavelength of x-rays  $\theta$  is the angle between the incident rays and crystal surface,  $d$  is the spacing between layers of atoms. The constructive interference occurs when  $n$  is an integer.

In the present project, X-ray diffraction was used extensively to analyze the crystalline and epitaxial quality of the nanostructures, as well as to determine the internal strains. The diffraction patterns were collected using a four-circle Bruker D8 Discover XRD system equipped with a single Gobel mirror and a scintillation counted. Cu  $K\alpha$  radiation was used. *In situ* high-temperature experiments were conducted to study the cubic-tetragonal ferroelectric phase transition in the  $\text{PbTiO}_3$  phase of the nanostructures and its effect on internal strains.

### ***3.3 Transmission Electron Microscopy (TEM)***

The optical principle of TEM is similar to that of the conventional optical microscopy. The only difference is that TEM uses electrons as source, and the electron beam is focused by a series of electromagnetic lenses. Samples for TEM must be specially prepared to very small thickness, normally thinner than 50 nm, to become sufficiently transparent for electrons. The attainable highest resolution is determined by the source wavelength. As the wavelength of electrons is in the order of an angstrom, the TEM, depending on a specific configuration, can reveal details as small as individual atoms.

TEM was used extensively in this study to analyze structure, defects, phase morphologies, and chemistry of the nanostructures. The samples for TEM were prepared using conventional slicing, grinding, and polishing followed by ion thinning until perforation in a Gatan Precision Polishing System (PIPS) operated at 5 kV and an angle of 5°. The samples were examined in a Philips EM 430 TEM operated at 200 Kv and a JEOL-3010 UHR TEM operated at 300 kV. The latter microscope is equipped with a Gatan Imaging Filter which was used to collect Electron Energy Loss Spectra for the compositional analysis. The EELS spectra were collected with the microscope operated in the imaging mode and the area to be analyzed was selected using the entrance aperture of the spectrometer. The spatial resolution of EELS in this mode is determined by chromatic aberration of the objective lens; that is, the spatial resolution varies with the energy loss. Therefore, the parts of EELS spectra containing the characteristic  $L_{2,3}$  absorption edges of Ti, Fe, and Co were recorded separately to maintain sufficiently high spatial resolution ( $\approx 1$  nm) for all three elements. Three to five spectra were recorded for each phase (i.e.  $\text{PbTiO}_3$  and  $\text{CoFe}_2\text{O}_4$ ).

### ***3.4 Scanning Electron Microscopy (SEM)***

Scanning Electron Microscopy was used in this project to reveal the nanostructure morphologies. SEM utilizes electron source to image the sample surface. The operating voltage used in SEM is much smaller than those TEM, so that the electron beam interacts with the sample surface layer about several microns deep.

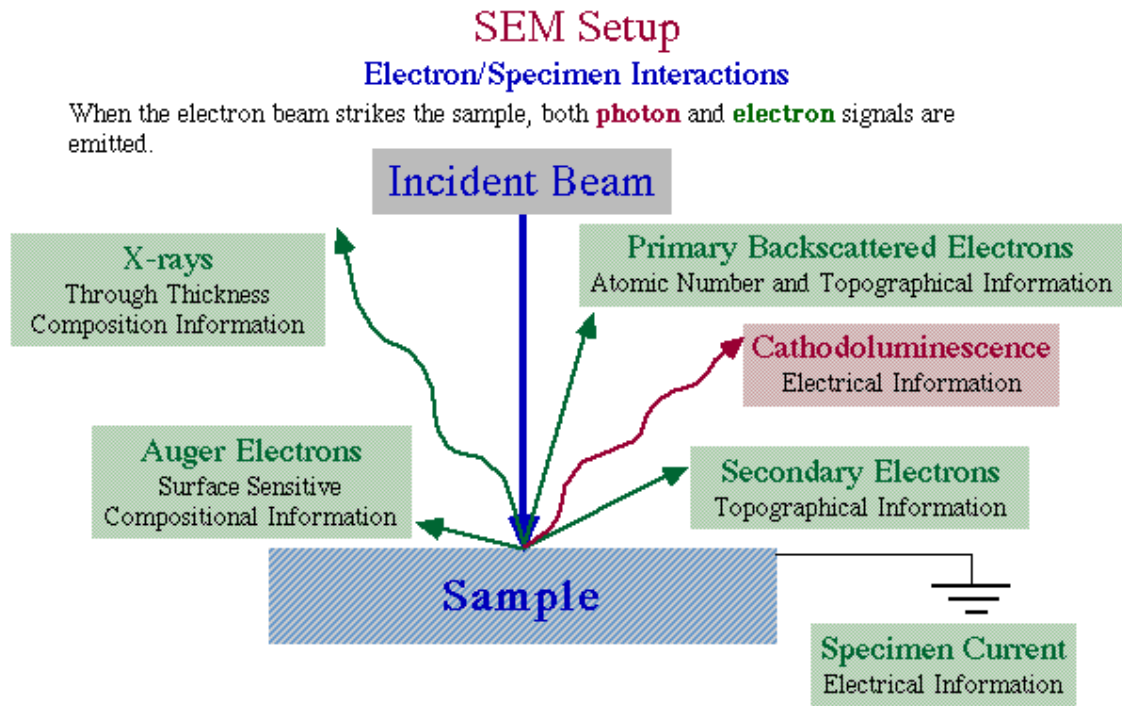


Figure 3.3 Schematic illustration of Electron/Specimen interactions. Figure adapted from ref. [66]

Different detectors are used to collect various sample-electron interaction signals to emphasize either sample topography or composition.

When the electron beam interacts with the sample, there are several kinds of electrons and photon is generated (Fig. 3.3). Secondary electrons, one of the most commonly used signals, are generated by the inelastic interaction of the incident energetic electron beam with weakly bonded conduction-band electrons in metals or the valence electrons of insulators and semiconductors. The energy of secondary electrons is very small (less than 50 eV). An electron detector is used convert the radiation of interest into an electrical signal, and display in image form after signal processing electronics. Backscattered electrons result from the elastic interaction between the incident electron beam and the atom nuclei in the sample. The changes in the energy of the incident electrons are very small ( $<1\text{eV}$ ). The backscattered electrons carrier the information about both topography and atomic number of the specimen.

### ***3.5 Atomic Force Microscopy (AFM)***

The atomic force microscope is one type of scanned-proximity probe microscopes which is used to measure various local properties of the sample, such as height, optical absorption, or magnetism [67-69]. AFM system consists of a tube-scanner, a position-sensitive photo-detector, and a cantilever with a probe located at the free end. There are numerous modes which are designed for specific

measurements including piezoelectric force mode (PFM) and magnetic force mode (MFM). Both of these modes were used in this study to perform ferroelectric and magnetic measurements respectively. The piezoelectric coefficient measurements can be conducted by adding a lock-in amplifier into the system. A schematic experimental setup for these techniques is illustrated in Fig. 3.4.

Piezoelectric force microscopy is a voltage modulated scanning probe microscopy. Small AC voltage with a frequency  $\omega$  is applied to the conductive probe which causes the ferroelectric domains under the electric field to vibrate at the same frequency due to the converse piezoelectric effect. This vibration forces the AFM tip to oscillate, and the modulated deflection signal is detected by a photo diode. The measured cantilever deflections are used to generate a map of surface topography. The AFM tips used in this study were standard silicon tips coated with a Pt/Ir alloy for electrical conduction. During measurements, the frequency of the applied voltage was much lower than the cantilever resonant frequency in order to avoid mechanical resonance of the cantilever. The typical force constant of these tips was 5 N/m, and the resonance frequency (as specified by the manufacturer) was 60-80 kHz. The contact force was  $\sim 70$  to 100 nN. The measurement frequency used was 6.39 kHz.

In quantitative  $d_{33}$  measurement, an external DC plus a small AC voltage are applied to the capacitor through the conductive tip and the Pt top electrode. This ensures a homogenous electric field under the electrode; it also prevents the build up of electrostatic interaction between the cantilever and the sample. A lock-in amplifier was connected to AFM system to lock in the signal with same frequency with AC

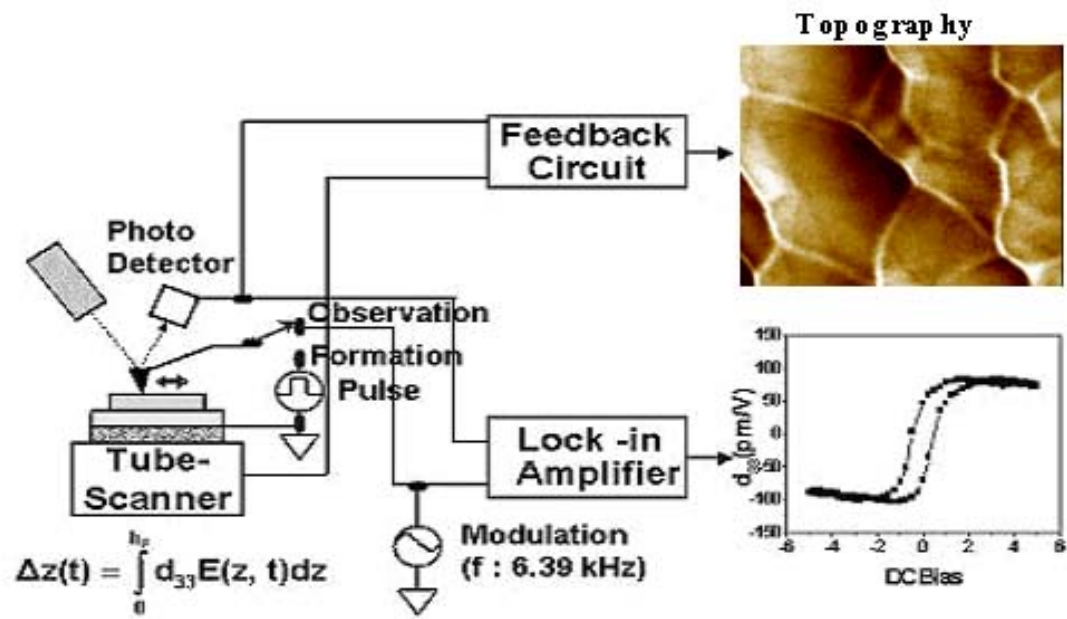


Fig.3. 4 Schematic illustration of the PFM setup.

driving voltage in order to screen out the noise. DC voltage was used to switch the domain structure inside the sample.

MFM is a variation of the Atomic Force Microscope (AFM), which is used to map out magnetic domains in the sample. The mode of operation is essentially non-contact imaging. Similar with an AFM, a sharp magnetized probe is attached to the bottom of a cantilever. The magnetic probe used in this study is standard silicon cantilever (or silicon nitride cantilever) coated with a magnetic thin film. The interaction of the tip with various magnetic domains in the sample results in cantilever deflection. The detector can sense the deflection of the cantilever, which will result in a force image in a static mode. Alternatively, it can detect the resonance frequency change of the cantilever, which will result in a force gradient image. The force gradient ( $F'$ ) detected contains information from both the surface structure and surface magnetization:

$$F' = F'_{surface} + F'_{magnetic}$$

where  $F'_{surface}$  is the surface component of the gradient and  $F'_{magnetic}$  is a magnetic component of the gradient. Signals from surface topography dominate at a distance close to the surface while, at a distance further away from the surface (typically beyond 100 nm), the magnetic signal dominates.

### ***3.6 Superconductor Quantum Interference Device (SQUID)***

A Superconductive Quantum Interface Device (SQUID) was used to measure the magnetic properties of the films. SQUID is the most sensitive magnetic flux

detector which can detect magnetic field less than  $1/50,000,000$  terrestrial magnetism. The system consists of superconductive material and Josephson junctions. In superconductors, current is carried by pairs of electrons, known as Cooper Pairs. Each pair can be treated as a single particle with a mass and charge twice that of a single electron. Unlike in normal conductor where electrons get scattered and have short wavelength, the superconductive electron pairs are not scattered, hence their wave functions are coherent over long distances. Josephson junction is the heart of SQUID technology which is a superconductor-insulator-superconductor (SIS) layer structure placed between two electrodes. When the insulator layer is thin enough, electron pairs can actually tunnel through the barrier with phase coherent. Two electrons form a Cooper pair through phonon exchange. All Cooper pairs are in the same quantum state (same momentum). SQUIDs generally use two Josephson junctions, as illustrated in Fig.3.5.

If there is no magnetic field, the current is divided evenly between the two junctions and there is no phase difference across the two junctions. But when the magnetic field is applied, the current in these two junctions are not equal any more, but their sum remains constant.

This kind of relationship gives a periodic dependence on the magnitude of the magnetic field. A maximum value occurs when the field is an integer number of fluxons, and a minimum value occurs at half integer values. A set of superconducting sensing loops is arranged in a configuration that only detects the magnetic flux from the magnetization of the sample (expels the uniform field applied to the sample by the superconducting magnet). The superconducting loops are detection gradiometer coils,

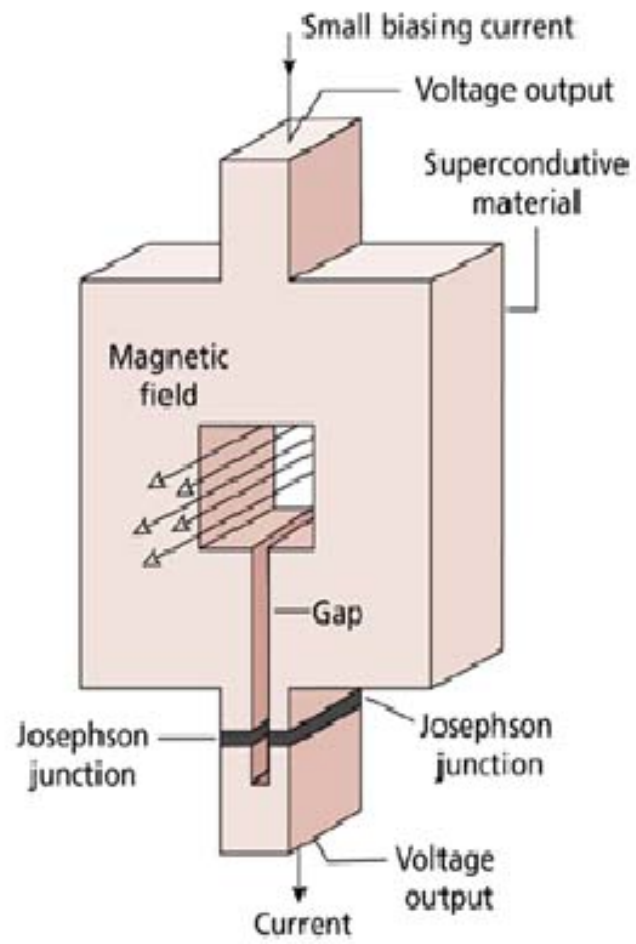


Fig.3. 5 Schematic illustration of the SQUID setup.

which are accurately balanced. As a sample moves through the coils, the magnetic moment of the sample induces an electric current in the detection coils. Since the coils, the connecting wires and the SQUID input coil form a closed superconducting loop, this current is not damped and any change in magnetic flux in the detection coils produces a proportional change in the persistent current in the detection circuit.

### ***3.7 Electrical Measurement***

Ferroelectric measurements were conducted using a commercial RT66 test system (Radiant Technologies). Fig. 3.6A shows the schematic of the electric set up used in this study. It consists of an Analog Data Precision model 2020 programmable pulse generator, load resistance and oscilloscope with an internal impedance of  $50\Omega$ . A series of square bipolar pulses train is generated and traverses to the test ferroelectric capacitor. The pulse sequence shown in is called PUND pulse series [70]. Polarization hysteresis loops were obtained for each test capacitor.

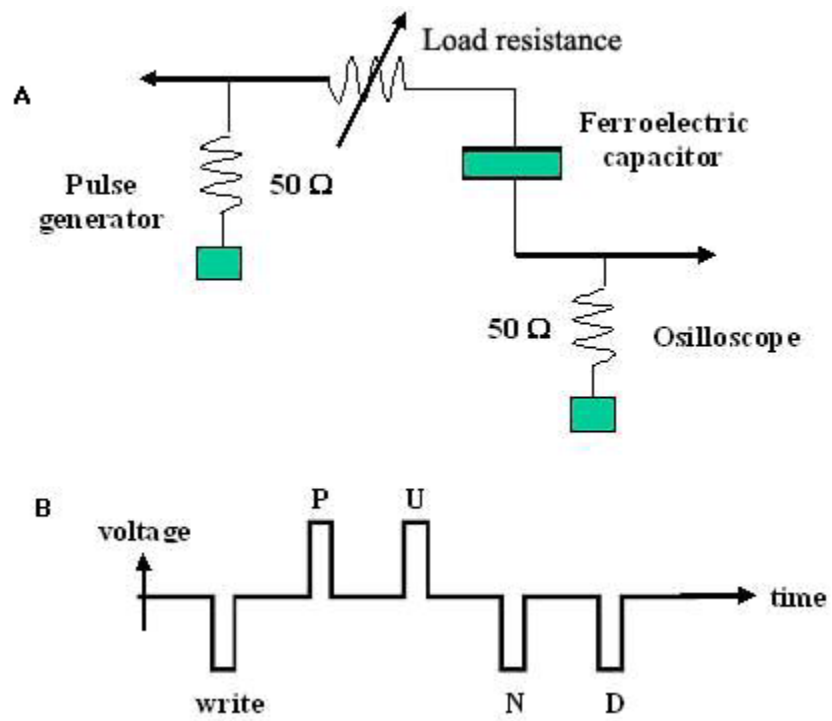


Fig.3.6 A. Schematic of electric measurement set-up; B. Pulse train for switching measurements.

# Chapter 4: Multiferroic Nanostructures in Epitaxial Films

## 4.1 *PbTiO<sub>3</sub>-CoFe<sub>2</sub>O<sub>4</sub> Film Growth*

The 3-D epitaxial PbTiO<sub>3</sub>-CoFe<sub>2</sub>O<sub>4</sub> films were grown using PLD on SrTiO<sub>3</sub> substrates having (001), (110), and (111) orientations. Composite ceramic targets were used to grow the films with fixed pre-selected phase fractions: 0.67PbTiO<sub>3</sub>-0.33CoFe<sub>2</sub>O<sub>4</sub> and 0.33PbTiO<sub>3</sub>-0.67CoFe<sub>2</sub>O<sub>4</sub>.

The growth conditions (substrate temperature, laser energy density and frequency, background gas pressure, and target to substrate distance) were optimized to create 3-D epitaxial heterostructures. The growth temperatures used in this study were in the range of 610°C-680°C. Lower temperature limit was determined to provide a well-defined two-phase mixture exhibiting sufficient crystallinity as inferred from the width of the X-ray reflections for the PbTiO<sub>3</sub> and CoFe<sub>2</sub>O<sub>4</sub> phases. Higher temperature limit was determined primarily by the Pb-loss. Laser energy density (laser energy divided by the spot size), which is crucial for dissociating a surface material from the target, depends on the target melting temperature and density. Materials with high melting points and densities normally require higher laser energy densities. PbTiO<sub>3</sub>-CoFe<sub>2</sub>O<sub>4</sub> is a composite ceramics with a relatively high melting temperature of 1570 °C, so the laser energy density used in this study was of about 1.6mJ/cm<sup>2</sup>. Film thickness uniformity is affected by the laser spot size, since larger spot sizes yield larger plums thus covering larger size substrates. Target-to-substrate distance is a parameter that determines the angular spread of the ablated

materials, normally target-to-substrate distance used in PLD technique is around 3-4cm. For the oxide growth, small amount of oxygen is always introduced into the chamber as a background gas to compensate for the oxygen loss during the target ablation process. The background pressure also affects the momentum of ablated species. The processing factors are not independent variables, so that the optimized processing parameters should be found interactively.

The processing parameters used to grow the  $\text{PbTiO}_3$ - $\text{CoFe}_2\text{O}_4$  films in the present study are detailed below:

(i) Substrate cleaning and target polishing.

The substrates were thoroughly cleaned to remove the organic and inorganic residuals on the surface before it was introduced into the vacuum chamber. The substrates were cleaned by soaking them in trichloroethylene (TCE), followed by acetone and isopropanol, for about 3 minutes each, under ultrasonic agitation. The target surfaces were polished using fine sandpaper prior to each growth.

(ii) Pumping the deposition chamber.

The growth chamber was evacuated to a base pressure less than  $1\text{E}-5$  Torr.

(iii) Target surface pre-cleaning

The laser was used to ablate the outer surface layer of the target to keep the target fresh; the substrates were kept covered during this target pre-cleaning.

(iv) The deposition parameters

After substrate pre-cleaning the oxygen was introduced into the deposition chamber with a dynamic pressure of 100mTorr. The substrate was heated to the

selected growth temperature (Table 4.1) with the heating rate of 1200°C/hour. The laser energy used was around 140mJ yielding about 40mJ on the target surface.

(iiv) Post-deposition annealing in oxygen.

After the deposition, the chamber was backfilled with the oxygen (1atm) and the films were cooled down to room-temperature at the rate of 5°C/min.

Selected films were grown on the SrRuO<sub>3</sub> as a bottom electrode to facilitate the electrical property measurements. The typical processing parameters used in this study are summarized in Table 4.1. A simultaneous growth on (001), (110), and (111) SrTiO<sub>3</sub> substrates was used to ensure similar growth conditions.

Table 4.1. Typical processing parameters used in the thin film deposition

|  | Deposition Temperature | Energy Density        | Laser Frequency | O <sub>2</sub> partial Pressure |
|--|------------------------|-----------------------|-----------------|---------------------------------|
| SrRuO <sub>3</sub>                                       | 630°C                  | 1.2mJ/cm <sup>2</sup> | 3Hz             | 100mTorr                        |
| PbTiO <sub>3</sub> -<br>CoFe <sub>2</sub> O <sub>3</sub> | 630°C                  | 1.6mJ/cm <sup>2</sup> | 5Hz             | 100mTorr                        |

## ***4.2 Structure Characterization***

### **4.2.1 XRD Characterization**

Typical XRD  $\theta$ -2 $\theta$  scans reveal distinct PbTiO<sub>3</sub> and CoFe<sub>2</sub>O<sub>4</sub> diffraction peaks as well as the SrTiO<sub>3</sub> reflection. No reflections corresponding to other phases were detected suggesting a two-phase mixture in the film. A combination of  $\theta$ -2 $\theta$

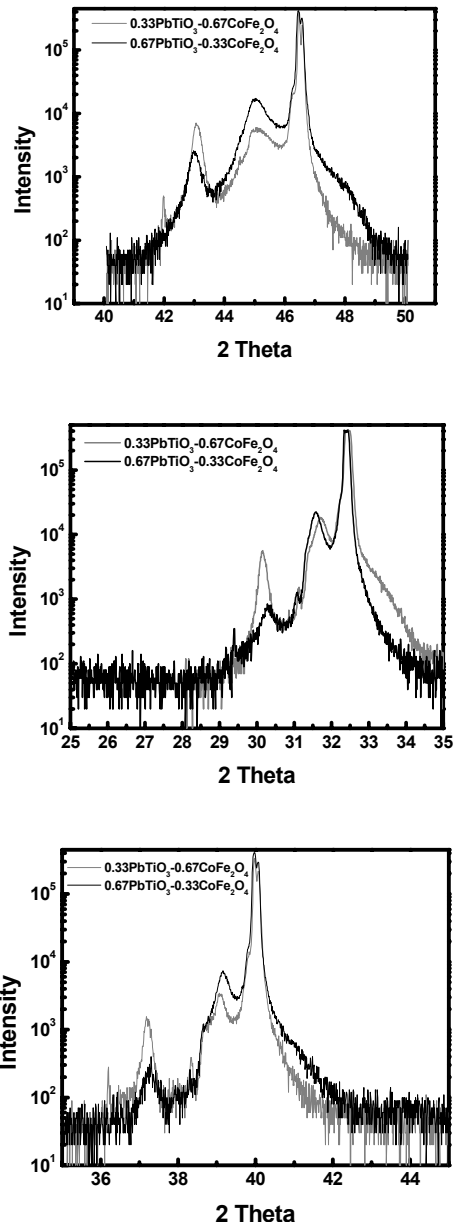


Fig. 4.1 X-ray diffraction patterns of CoFe<sub>2</sub>O<sub>4</sub>- PbTiO<sub>3</sub> thin film

- A) (001) orientation of the SrTiO<sub>3</sub> substrate
- B) (110) orientation of the SrTiO<sub>3</sub> substrate
- C) (111) orientation of the SrTiO<sub>3</sub> substrate

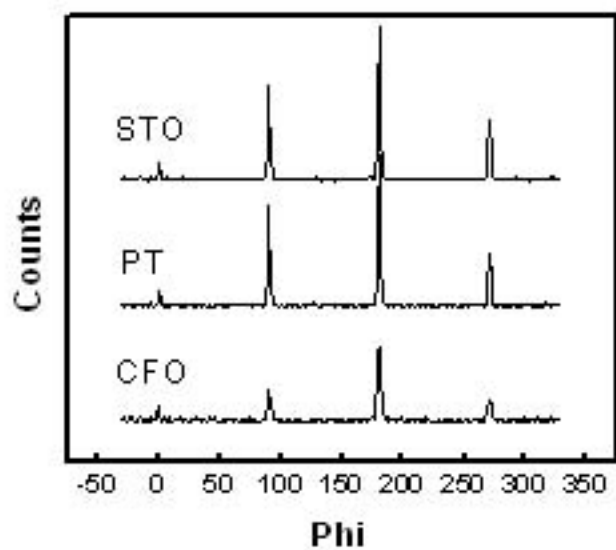


Fig. 4.2 Phi scan of the  $0.33\text{CoFe}_2\text{O}_4\text{-}0.67\text{PbTiO}_3$  thin film grown on (001)  $\text{SrTiO}_3$  substrate

(Fig. 4.1) and  $\phi$ -scans (Fig. 4.2) confirmed a 3-D cube-on-cube epitaxy in these two-phase films regardless of substrate orientation and film composition.

Fig.4.1 describes the  $\theta$ - $2\theta$  scan of the films with two different compositions  $0.33\text{PbTiO}_3$ - $0.67\text{CoFe}_2\text{O}_4$  and  $0.67\text{PbTiO}_3$ - $0.33\text{CoFe}_2\text{O}_4$ , grown under similar conditions on (001), (110), and (111)  $\text{SrTiO}_3$ . All the films have similar thickness of about 230 nm. The relative peak heights for the reflections of the two phases vary in accordance with the phase fractions. The full widths at half maximum (FWHM) measured for the  $\text{PbTiO}_3$  and  $\text{CoFe}_2\text{O}_4$  002 rocking curves are of about  $0.5^\circ$ , indicating a reasonable epitaxial quality. The out-of-plane lattice spacings calculated from the peak positions (the  $\text{SrTiO}_3$  reflection was used as a reference) are shown in Table 4.2.

Table 4.2 Out-of-plane d-spacing of  $\text{CoFe}_2\text{O}_4$ -  $\text{PbTiO}_3$  thin film

|                                      | (001)  | (110)  | (111)  |
|--------------------------------------|--------|--------|--------|
| $\text{PbTiO}_3$ (PTO-rich)          | 4.0250 | 2.8200 | 2.2991 |
| $\text{CoFe}_2\text{O}_4$ (PTO-rich) | 8.4156 | 5.9284 | 4.8232 |
| $\text{PbTiO}_3$ (CFO-rich)          | 4.0226 | 2.8322 | 2.3045 |
| $\text{CoFe}_2\text{O}_4$ (CFO-rich) | 8.4082 | 5.8966 | 4.8320 |
| $\text{PbTiO}_3$ (bulk)              | 4.152  | 2.8496 | 3.2943 |
| $\text{CoFe}_2\text{O}_4$ (bulk)     | 8.3919 | 5.9331 | 4.8451 |

During the deposition process, the epitaxial strains develop due to a lattice misfit with the component phases in the film and the lattice misfits with the substrate. At the growth temperatures, the lattice parameter of cubic  $\text{CoFe}_2\text{O}_4$  is larger than that

of the cubic  $\text{PbTiO}_3$  so that the compressive and tensile out-of-plane epitaxial strains are expected to develop in the  $\text{CoFe}_2\text{O}_4$  and  $\text{PbTiO}_3$ , respectively. These epitaxial stresses can be relaxed, for example, by formation of interfacial dislocations leading to semi-coherent or incoherent interfaces. Cooling the  $\text{PbTiO}_3$ - $\text{CoFe}_2\text{O}_4$  films from the growth temperature is accompanied by the cubic-to-tetragonal phase transition in  $\text{PbTiO}_3$  which occurs (in the bulk) at  $T=490\text{ }^\circ\text{C}$ . This phase transition is expected to be accompanied by a large tetragonal distortion and thus is expected to induce significant internal strains in the composite film.

According to the XRD measurements (Table 4.2), the (001)-oriented films feature significant compressive and tensile out-of-plane strains in the  $\text{PbTiO}_3$  and  $\text{CoFe}_2\text{O}_4$  phases, respectively. Thus, the resulting internal stresses in the composite films are determined by those associated with the phase transition in  $\text{PbTiO}_3$ . *In situ* variable-temperature measurements of the out- ( $a_\perp$ ) and in-plane ( $a_\parallel$ ) lattice parameters of  $\text{CoFe}_2\text{O}_4$  and  $\text{PbTiO}_3$  were conducted for the (001)  $0.33\text{CoFe}_2\text{O}_4$ - $\text{PbTiO}_3$  film (Fig. 4.3). The results revealed that the ferroelectric Curie temperature  $T_c=450\text{ }^\circ\text{C}$  in the  $\text{PbTiO}_3$  in the nanostructure is relatively close to bulk value of  $T_c=490\text{ }^\circ\text{C}$ . However, the constraint from  $\text{CoFe}_2\text{O}_4$  effectively suppresses the 1<sup>st</sup> order character of the cubic→tetragonal transition in  $\text{PbTiO}_3$  and results in a much smaller tetragonality ( $a_\perp/a_\parallel$ ) than expected for the bulk. At the same time, expansion of  $a_\perp$  in  $\text{PbTiO}_3$  upon phase transition causes the  $a_\perp$  of  $\text{CoFe}_2\text{O}_4$  to expand as well thus generating a tensile out of plane strain in  $\text{CoFe}_2\text{O}_4$ . Unfortunately, a fully quantitative strain analysis in these nanostructures is limited by the uncertainty about the reference (strain-free) lattice parameters for the constituent phases, which is partly

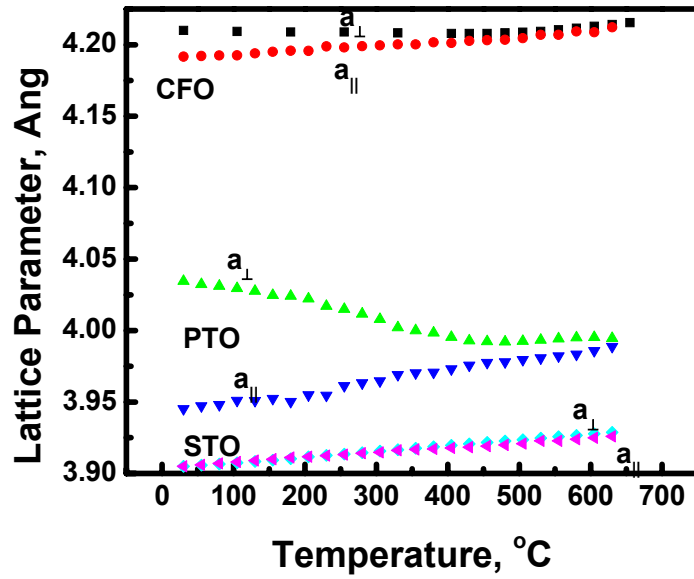


Fig. 4.3 Effective out-of-plane lattice spacing as function of temperature for the (001) film  $0.33\text{CoFe}_2\text{O}_4\text{-}0.67\text{PbTiO}_3$

caused by the mutual solubility of transition metal cations in both phases, as discussed below.

#### 4.2.2 TEM Characterization

Fig. 4.4 shows typical electron diffraction patterns recorded from the  $0.33\text{CoFe}_2\text{O}_4\text{-}0.67\text{PbTiO}_3$  films grown on (001), (110), and (111)  $\text{SrTiO}_3$ ; the reflections associated with both phases are indicated. The electron diffraction confirms a 3-D epitaxy for all composite films. The  $\langle 110 \rangle$  zone axis diffraction patterns from all films additionally featured weak but well-defined superlattice reflections. These reflections match the hexagonal unit cell of magnetoplumbite  $\text{PbFe}_{12}\text{O}_{19}$ , which is expected to occur in equilibrium with the  $\text{PbTiO}_3$  and  $\text{CoFe}_2\text{O}_4$  for all  $x\text{CoFe}_2\text{O}_4\text{-(}1-x\text{)PbTiO}_3$  compositions.

Fig. 4.5 summarizes plane-view and cross-sectional images for the  $0.33\text{CoFe}_2\text{O}_4\text{-}0.67\text{PbTiO}_3$  film grown on (001), (110), and (111) substrates. As seen in cross-sectional images, transverse nanostructures with the  $\text{CoFe}_2\text{O}_4/\text{PbTiO}_3$  interfaces aligned perpendicular to the substrate were obtained for all substrate orientations. However, the morphologies of these nanostructures vary strongly with a substrate orientation. In particular, the rod-like pillars of  $\text{CoFe}_2\text{O}_4$  are replaced by lamellar-like  $\text{CoFe}_2\text{O}_4$  on going from (001) to (110) orientation, whereas the labyrinth-like morphology is observed for the (111) substrate. In the plane-view images, the  $\text{CoFe}_2\text{O}_4$  rods in the (001) nanostructures appear faceted on the  $\{110\}$  planes perpendicular to the substrate. However, cross-sectional samples reveal that the  $\text{CoFe}_2\text{O}_4/\text{PbTiO}_3$  interfaces are strongly faceted on the  $\{111\}$  planes alternating



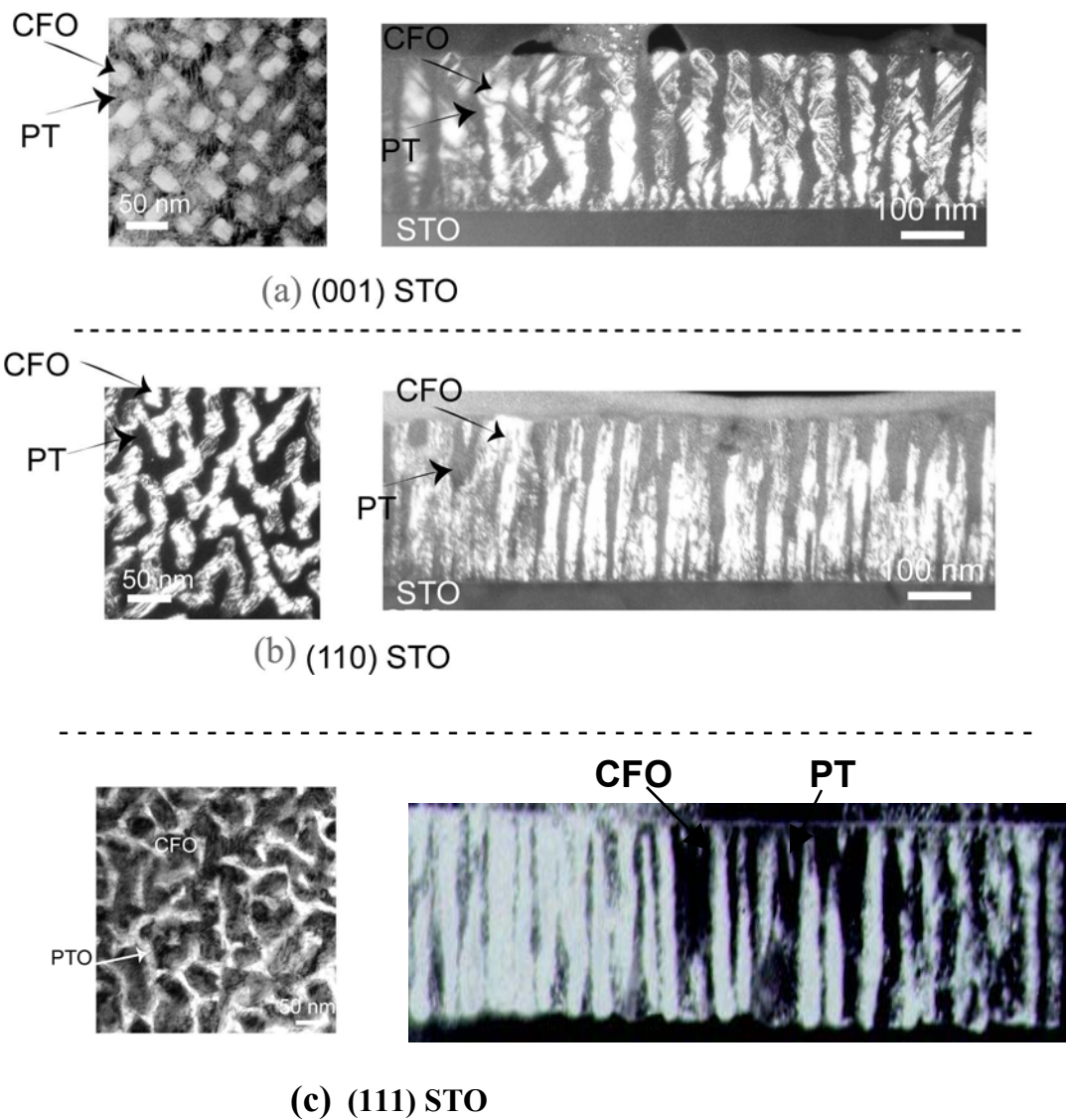


Fig. 4.5 TEM plane view and cross-section dark field images of the  $0.33\text{CoFe}_2\text{O}_4$ - $0.67\text{PbTiO}_3$  films grown on differently oriented  $\text{SrTiO}_3$  substrates: a) (001); b) (110); c) (111)

around the average vertical  $\{110\}$  orientation (Fig. 4.6a). The  $\text{CoFe}_2\text{O}_4/\text{PbTiO}_3$  interfaces in the (110) oriented nanostructures reside on the two sets of  $\{111\}$  planes perpendicular to the substrate. The resulting nanostructures feature two sets of vertical  $\text{CoFe}_2\text{O}_4$  lamellae which are preferentially ( $\pm 35^\circ$ ) aligned with the [100] direction in the film plane.

For all substrate orientations,  $\text{CoFe}_2\text{O}_4$  exhibited a high incidence of planar defects on the  $\{111\}$  planes. For the (100) substrate, these defects occurred primarily on the (111) planes inclined at  $35^\circ$  to the substrate surface, whereas for the (110) substrate, the defects resided on the (111) planes perpendicular to the surface as seen in Fig.4.6b. Some of these defects were confirmed to be twins and stacking faults commonly encountered in spinel-type phases. Other defects represented coherent intergrowths of the  $\text{CoFe}_2\text{O}_4$  with the thin lamellae of a  $\text{PbFe}_{12}\text{O}_{19}$ -like structure (Fig. 4.6c) which gave rise to the superlattice reflections observed in the  $\langle 110 \rangle$  zone axis electron diffraction patterns (Fig. 4.4.b). Dislocation arrays were observed at both  $\text{CoFe}_2\text{O}_4/\text{PbTiO}_3$  and film/substrate interfaces indicating that the interfaces are at least semi-coherent. The  $\text{PbTiO}_3$  was observed to wet the  $\text{SrTiO}_3$  presumably due a smaller (compared to  $\text{CoFe}_2\text{O}_4$ ) lattice misfit with a substrate; that is, the footprint of  $\text{CoFe}_2\text{O}_4$  on the  $\text{SrTiO}_3$  is much smaller than that of  $\text{PbTiO}_3$ .

Qualitative compositional analyses of the nanostructures using EELS suggested mutual solubility of Fe and Ti in the  $\text{PbTiO}_3$  and  $\text{CoFe}_2\text{O}_4$ , respectively (Fig. 4.7); some contribution of Ti from the residual  $\text{SrTiO}_3$  can not be ruled out, though no indications of  $\text{SrTiO}_3$  overlapping with  $\text{CoFe}_2\text{O}_4$  could be detected in the HRTEM images of the areas analyzed.

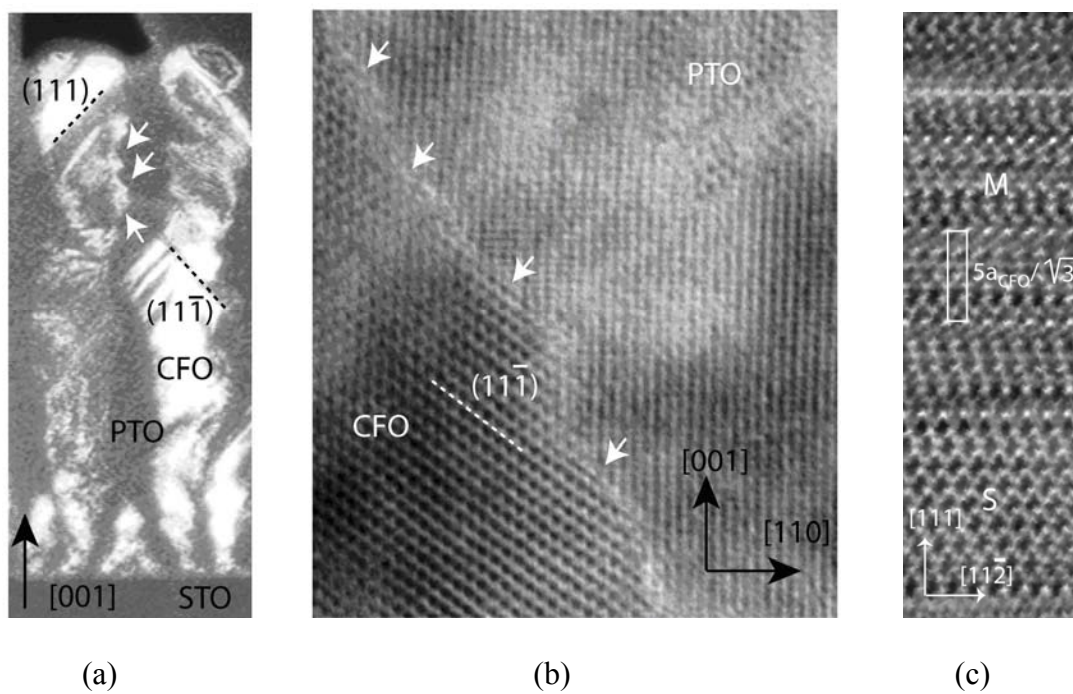


Fig. 4.6 a) Magnified TEM cross-sectional image of the  $0.33\text{CoFe}_2\text{O}_4\text{-}0.66\text{PbTiO}_3$  film grown on (001)  $\text{SrTiO}_3$  ; b) HRTEM image of the  $\text{CoFe}_2\text{O}_4/\text{PbTiO}_3$  interface in the same cross-sectional sample; c) HRTEM image of  $\text{CoFe}_2\text{O}_4$

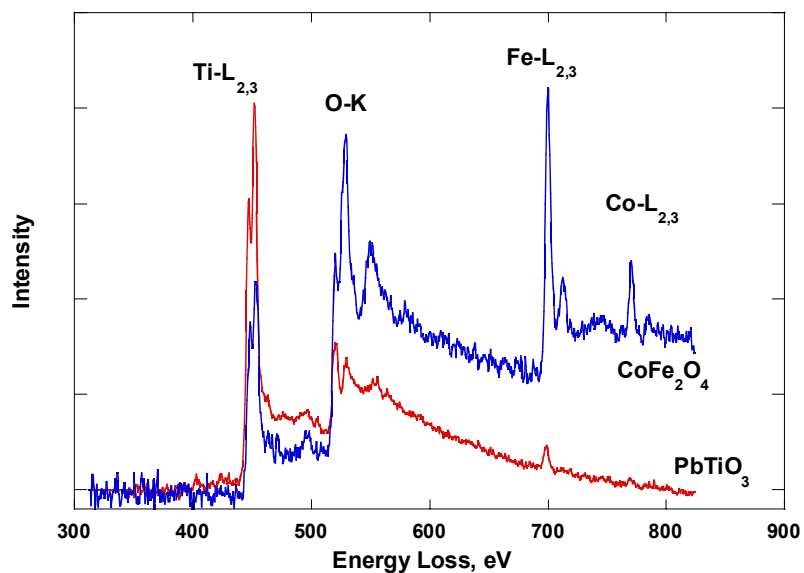


Fig. 4.7 Representative EELS spectra recorded from the  $\text{CoFe}_2\text{O}_4$  and  $\text{PbTiO}_3$  phases. The presence of Ti in the  $\text{CoFe}_2\text{O}_4$  and of Fe in the  $\text{PbTiO}_3$  was additionally confirmed by recording separate EELS spectra with the microscope energy offsets corresponding to the Ti-L<sub>2,3</sub> (450 eV) and Fe-L<sub>2,3</sub> (710 eV) edges, respectively.

Fig. 4.8 summarizes plane view TEM dark-field images for the  $0.67\text{CoFe}_2\text{O}_4\text{-}33\text{PbTiO}_3$  films. For the (001) orientation, no obvious rod $\leftrightarrow$ matrix reversal, as compared to the  $\text{PbTiO}_3$ -rich composition, was observed: the film still featured rectangular-shaped  $\text{CoFe}_2\text{O}_4$  rods (70-80 nm) in a continuous  $\text{PbTiO}_3$  matrix. In contrast, for the (110) and (111) orientations, the films featured isolated  $\text{PbTiO}_3$  nanorods embedded into the  $\text{CoFe}_2\text{O}_4$  matrix. For the (110) orientations the  $\text{PbTiO}_3$  rods exhibited an irregular shape with neighboring rods, occasionally, being connected to each other. The (111) films contained well-separated cylindrical  $\text{PbTiO}_3$  nanorods (Fig.4.8c).

#### **4.2.3 SEM Topography Characterization**

The nanostructure morphologies can be imaged using a high-resolution SEM which provides a non-destructive high-throughput alternative to the TEM, bearing in mind that the contrast in SEM reflects the surface topography and compositional differences. Fig. 4.9 summarizes secondary electrons SEM images of nanostructure surfaces for several film compositions grown on differently oriented substrates. The contrast is dominated by the large differences in the average atomic numbers for the two phases, with the  $\text{PbTiO}_3$  and  $\text{CoFe}_2\text{O}_4$  appearing as bright and dark regions, respectively. Systematic changes in the nanostructure morphologies are observed consistent with the TEM. The non-destructive SEM imaging was used to verify the morphologies of the samples before electrical/magnetic characterization.

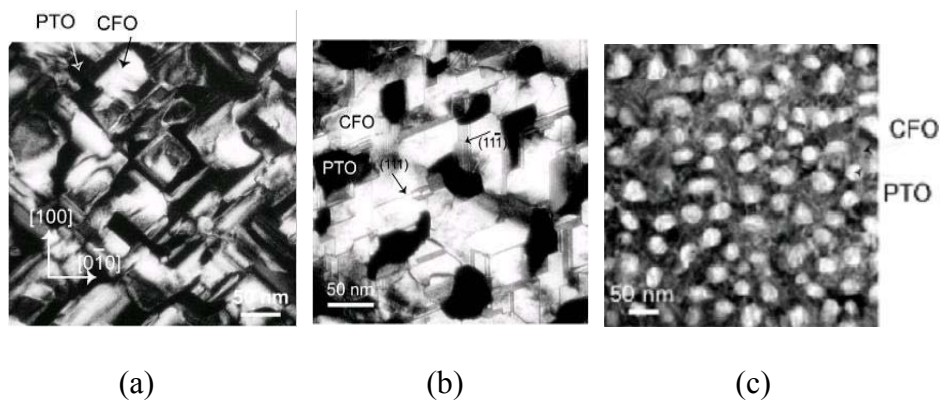


Figure 4.8 TEM dark field images of the  $0.33\text{PbTiO}_3\text{-}0.67\text{CoFe}_2\text{O}_4$  films on differently oriented  $\text{SrTiO}_3$  substrates a) (001); b) (110); c) (111)

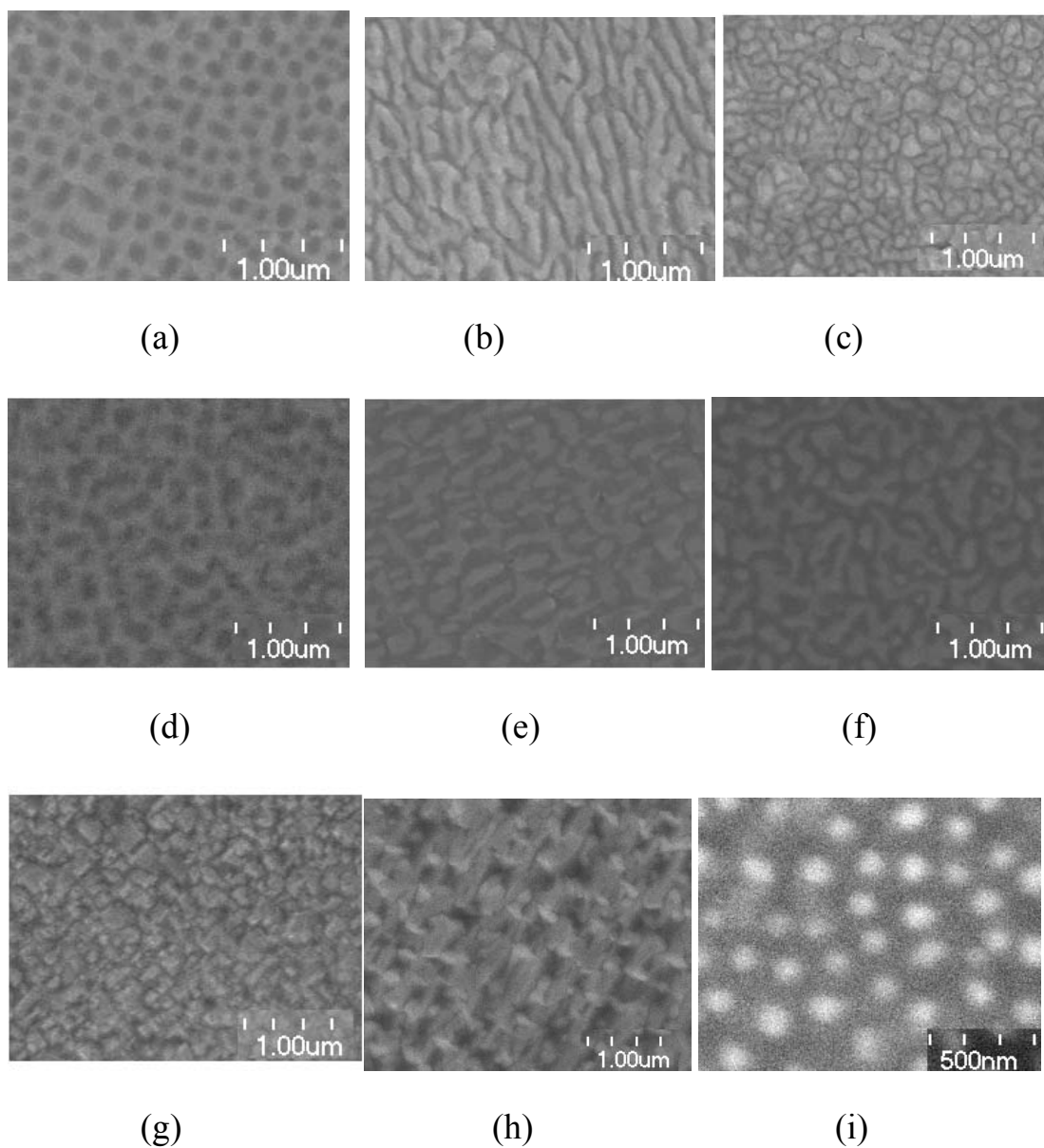


Fig. 4.9 SEM plane-view images: a)-c)  $0.67\text{PbTiO}_3\text{-}0.33\text{CoFe}_2\text{O}_4$  on a)-(001), b)-(110) and c)-(111)  $\text{SrTiO}_3$ ; d)-f)  $0.57\text{PbTiO}_3\text{-}0.43\text{CoFe}_2\text{O}_4$  on d)-(001), e)-(110), and f)-(111)  $\text{SrTiO}_3$ ; g)-i)  $0.33\text{PbTiO}_3\text{-}0.67\text{CoFe}_2\text{O}_4$  on g)-(001), h)-(110), and i)-(111)  $\text{SrTiO}_3$

### ***4.3 Discussion of Formation of Self-Assembling Two-Phase Nanostructures***

The experimental study of morphology of multiferroic nanostructures proves that there is a 3-D epitaxial relationship between phases and each phase and a substrate for all studied substrate orientations and different phase fractions. The presence of an internal stress in nanostructures demonstrates that the interfaces are coherent or semi-coherent. Our experimental approach is based on the idea that through the change of substrate orientation and fractions of the phases we can manipulate stress state in epitaxial nanostructures and control their morphologies. In this section we compare the experimentally obtained nanostructures with results of modeling of formation of two-phase nanostructures in epitaxial films on differently oriented substrates.

The theoretical model is based on the assumption that the morphology of the nanostructure is determined by the minimum of the interface energy and elastic energy of epitaxial stresses which arise due to a nanoscale of a multiphase film. The individual phases in the nanostructure can be considered as elastic domains which self-assemble to minimize the long-range elastic field in the film [71,72]. This approach allows one to consider analytically the effect of substrate orientations on morphologies of nanostructures [73] and to develop a phase-field model for the analysis and prediction of their architectures and stress conditions [74].

Elastic interactions arise in multiphase nanostructures due to epitaxy, resulting in formation of coherent or semi-coherent inter-phase boundaries and film/substrate interfaces. The stress state in the coherent multiphase film/substrate system can be described using the self-strains of the component phases, as determined from the differences in the lattice parameters of the undistorted phases and a substrate, the latter being used as a reference state [65,66]. For a coherent two-phase nanostructure consisting of  $\text{PbTiO}_3$  ( $a_1=3.96 \text{ \AA}$ ) and  $\text{CoFe}_2\text{O}_4$  ( $a_2=8.38 \text{ \AA}/2=4.19 \text{ \AA}$ ) on a  $\text{SrTiO}_3$  ( $a_s=3.95 \text{ \AA}$ ) substrate can be described by a distorted cubic lattice (Fig.4.10a, b).

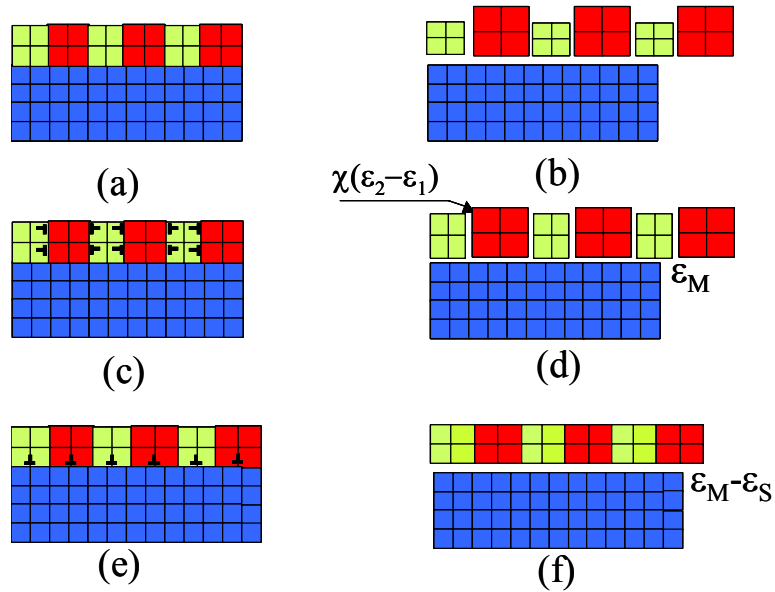


Fig.4.10. Schematic drawings of a)-b) a coherent two-phase structure on a substrate, c)-d) semi-coherent structure with the inter-phase boundaries partially relaxed along the normal to the substrate, e)-f) semi-coherent structure with a partially relaxed film/substrate interface.

Since both phases are cubic at the growth temperature, the self-strains correspond to a pure dilatation,  $\varepsilon_1 = (a_1 - a_s)/a_s = 0.0025$  and  $\varepsilon_2 = (a_2 - a_s)/a_s = 0.061$ . However, the nanostructures grown experimentally are semi-coherent and feature misfit dislocations (Fig.4.10, c-f). Therefore, the strain relaxation along the interfaces (both inter-phase boundaries and film/substrate interface) needs to be considered. Two types of relaxation is considered in the model: one relaxation along vertical interfaces ( $\chi$ ):

$$\Delta\varepsilon = \varepsilon_0 \begin{pmatrix} 1 & 0 & 0 \\ 0 & 1 & 0 \\ 0 & 0 & \chi \end{pmatrix}; \quad \chi = 1 - \frac{b\rho}{\varepsilon_0}$$

where  $\rho$  is a misfit dislocation density at the interfaces normal to the substrate with the Burgers vector  $b = a_2 - a_1$ . Another, relaxation along film substrate interfaces, which can be described by an effective change in the substrate lattice parameter,  $a_s^{\text{eff}} = a_s(1 - \rho_m b)$ , where  $\rho_m$  is the misfit dislocation density and  $b$  is the dislocation Burgers vector [75,76].

Near equilibrium, the arrangement of phases, their morphologies, and the relaxation parameters of the interfaces ( $\chi, a_s^{\text{eff}}$ ) can be found by minimizing the sum of the elastic and interfacial energies for a given phase fraction. Since for the equilibrium semi-coherent systems, the phase fraction is explicitly related to the relaxation parameters, phase-field modeling which assumes fixed values of the relaxation parameters can be used to find the equilibrium morphologies and phase fractions for semi-coherent nanostructures.

In the phase-field model, a multiphase system is described as a continuous field of the order parameter,  $\eta(\mathbf{r})$ . Unconstrained equilibrium phases correspond to the two minima ( $\eta_0^1, \eta_0^2$ ) of the specific free energy  $f(\eta)$  with a self-strain is a linear function of order parameter. The equilibrium two-phase nanostructure can be determined by minimizing the free energy functional along  $\eta(\mathbf{r})$ :

$$F = \int_V \left[ f(\eta) + \frac{1}{2} \beta_{ij} \frac{\partial \eta}{\partial x_i} \frac{\partial \eta}{\partial x_j} + \frac{1}{2} C_{ijkl} (\varepsilon_{ij}(\mathbf{r}) - \varepsilon_{ij}^0(\mathbf{r})) (\varepsilon_{kl}(\mathbf{r}) - \varepsilon_{kl}^0(\mathbf{r})) \right] dV \quad (4)$$

The first and second terms in the integrand determine the interfacial energy, where  $\beta_{ij}$  is a gradient coefficient. The third term represents elastic energy, where  $C_{ijkl}$  is the elastic modulus,  $\varepsilon_{ij}(\mathbf{r})$  denotes total strain, and  $\varepsilon_{ij}^0(\mathbf{r})$  is the transformation self-strain.

The order parameter of the substrate,  $\eta_S$ , is fixed. Since  $\varepsilon_{sij}^{eff} = \frac{a_s^{eff} - a_s}{a_s} = \varepsilon_{ij}^0 \cdot \eta_S + \bar{\varepsilon}_{ij}^0$ , the value of  $\eta_S$  describes the relaxation of the film/substrate interface.

The phase fractions, periodicity, and arrangement in the equilibrium nanostructure can be obtained for any given relaxation parameters,  $\eta_S$  and  $\chi$ , using

$$\frac{\delta F}{\delta \eta(\mathbf{r})} = 0 \quad (5)$$

where  $\delta \dots / \delta \eta(\mathbf{r})$  is a variational derivative. To solve Eq. (5), the relaxation procedure, which considers a virtual phase transformation from the unstable initial phase ( $\eta=0$ ) to a two-phase state corresponding to the two minima of  $f(\eta)$  has been employed.

The function

$$f(\eta) = f_0 (1 - \eta^2)^2 \quad (6)$$

satisfies these conditions with the minima at  $\eta_0^1 = -1$ ,  $\eta_0^2 = 1$ . The time evolution of the phase-field of the order parameter  $\eta(\mathbf{r}(t))$  is described by the equation:

$$\frac{\partial \eta}{\partial t} = -L \frac{\delta F}{\delta \eta} + \xi \quad (7)$$

where  $L$  is a kinetic coefficient and  $\xi$  is the Langevin noise term. The Eq.(7) has been solved using Khachaturyan's microelasticity approach in phase-field modeling [77, 78, 79].

The phase field modeling has been performed for elastically homogenous film with positive elastic anisotropy ( $\zeta = \frac{C_{11} - C_{12} - 2 \cdot C_{44}}{C_{44}}$ ) corresponding to average elastic properties of the  $\text{PbTiO}_3\text{-CoFe}_2\text{O}_4$  films ( $\text{CoFe}_2\text{O}_4$  has large positive elastic

anisotropy). Different crystallographic orientations of the film were introduced by rotating the elastic moduli tensor  $C_{ijkl}$ ,  $C_{mnop} = a_{mi}a_{nj}a_{ok}a_{pl}C_{ijkl}$ ,  $a_{\alpha\beta}$  are the rotation matrix elements. The comparison of results of phase field modeling with experimental results is presented in Fig.4.11. The inter-phase boundaries in all structures are perpendicular to the substrate surface. According to the simulations, the dissimilar in-plane morphologies in differently oriented films are determined by the in-plane elastic anisotropy of the film which varies with the film/substrate orientation. The phase field modeling predicts the change of morphologies of nanostructures at changing fractions of  $\text{CoFe}_2\text{O}_4$  as well as changing film orientation. Thus, for  $\text{PbTiO}_3$ -rich composition, isolated vertical nanorods/nanoplates of  $\text{CoFe}_2\text{O}_4$  faceted on  $\{110\}$  planes (Fig. 4.11a) are obtained on an (001) substrate, whereas vertical  $\text{CoFe}_2\text{O}_4$  nanoplates faceted on  $\{111\}$  planes (Fig. 4.11c) are obtained on a (110) substrate; these  $\{111\}$  nanoplates merge to form two sets of stripes preferentially ( $\pm 35^\circ$ ) aligned along the in-plane [100] direction (Fig. 4.11c). The labyrinth-like nanostructure of the  $\text{PbTiO}_3$ -rich films grown on (111) substrates (Fig.4.11e) transforms into well-organized  $\text{PbTiO}_3$  nanorods embedded in a  $\text{CoFe}_2\text{O}_4$  matrix with increasing fraction of the  $\text{CoFe}_2\text{O}_4$  phase (Fig.4.11f). According to theoretical and experimental results, nanostructures containing isolated magnetic nanorods in a ferroelectric matrix (Fig. 4.11a) or vice versa (Fig. 4.11f) can be obtained by varying the substrate orientation and phase fraction.

Comparison of the simulated and experimental nanostructures (Fig. 4.11) demonstrates that the phase-field modeling successfully reproduced even fine morphological details observed in the experimentally grown films and suggests that this approach can be used to predict the architecture of multiferroic nanostructures. Thus, the results of modeling justify the basic ideas of our experimental study, that elastic interactions play the dominant role in formation of nanostructures.

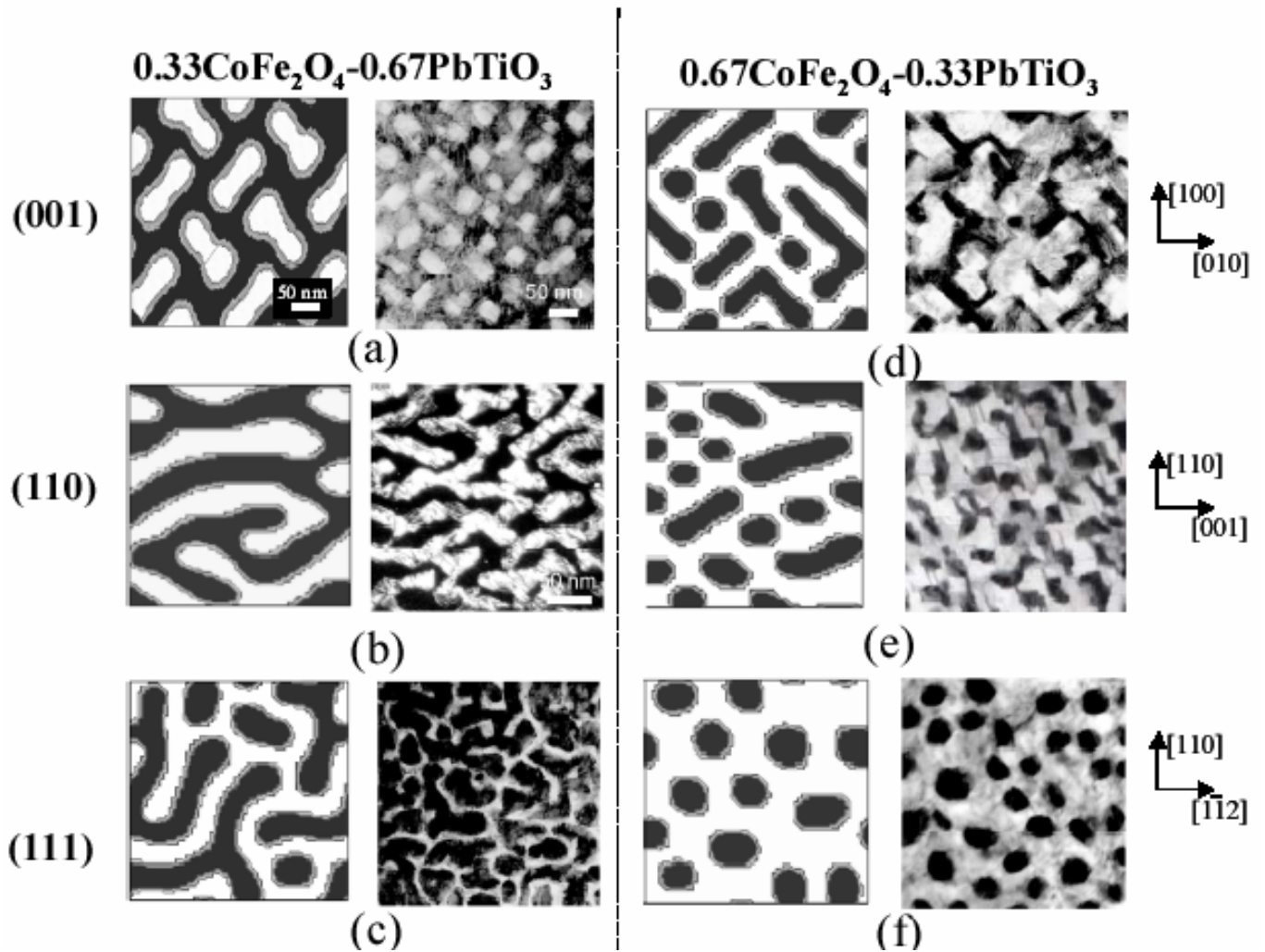


Fig.4.11 Top-view of TEM images of the epitaxial  $0.33\text{CoFe}_2\text{O}_4\text{-}0.67\text{PbTiO}_3$  (a-c) and  $0.67\text{CoFe}_2\text{O}_4\text{-}0.33\text{PbTiO}_3$  (e-f) films grown on  $\text{SrTiO}_3$  substrates having the following orientations: a), d)-(001), b), e)-(110), and c), f)-(111). Two images are shown for each combination of composition and orientation. The images on the left are results of the phase-field modeling, whereas the images on the right are experimental TEM micrographs. In all the images, the  $\text{CoFe}_2\text{O}_4$  and  $\text{PbTiO}_3$  phases appear as *bright* and *dark* regions, respectively.

# Chapter 5: Property Characterization

## 5.1 *Ferroelectric Properties*

The ferroelectric and piezoelectric measurements of the nanostructured thin films were conducted on films deposited on (001), (110) and (111) SrTiO<sub>3</sub> substrates with SrRuO<sub>3</sub> bottom electrodes and platinum top electrodes to facilitate the electric measurement.

### 5.1.1 Polarization Measurement

The polarization measurements of thin film were performed on RT66 set-up. Top electrodes have circular shape with 30nm diameter, which are patterned by standard photolithographic technique. A resistivity more than  $\sim 6 \times 10^8 \Omega\text{-cm}$  at zero field bias enables high field polarization and piezoelectric measurements of the films. These measurements are impossible for films with resistivity below  $1 \times 10^7 \Omega\text{-cm}$ . Only 0.67PbTiO<sub>3</sub>-0.33CoFe<sub>2</sub>O<sub>4</sub> films with orientations (001) satisfy this condition.

Fig.5.1 shows the ferroelectric P-E hysteretic loops obtained from a 0.66PbTiO<sub>3</sub>-0.33CoFe<sub>2</sub>O<sub>4</sub> film grown on (001) SrTiO<sub>3</sub> substrate at 630°C with a film thickness of 350 nm. The measurements were conducted with different applied voltages at a frequency of 15 kHz. The normalized saturated polarization value is about  $50 \mu\text{C}/\text{cm}^2$  on SrTiO<sub>3</sub> (001) substrate, which is less than the bulk value  $75 \mu\text{C}/\text{cm}^2$  due to the substrate clamping and constraint by CoFe<sub>2</sub>O<sub>4</sub> phase. The remnant polarization  $P_r$  is  $40 \mu\text{C}/\text{cm}^2$  and the coercive field  $E$  equals to 6mV/m.

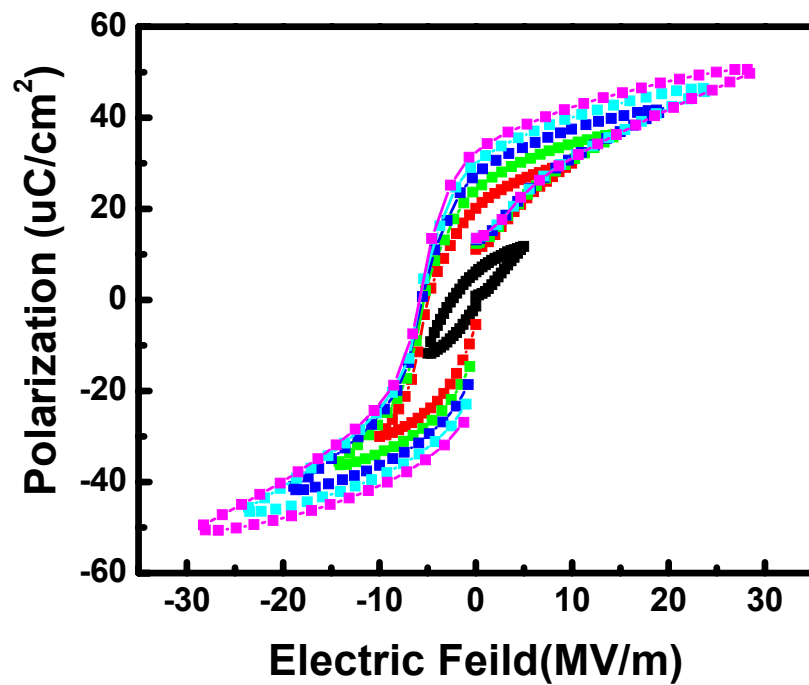


Fig. 5.1 Polarization hysteresis loop of the  $0.67\text{PbTiO}_3\text{-}0.33\text{CoFe}_2\text{O}_4$  thin film grown on (001)  $\text{SrTiO}_3$ .

The measured ferroelectric loop indicates that the multiferroic films grown on (001) substrate have ferroelectric properties. The films grown on (110) and (111) substrate orientations as well as films with larger fraction of  $\text{CoFe}_2\text{O}_4$  phase have high leakage due to high conductivity of a ferrite phase.

### 5.1.2 Piezoelectric Properties

Piezoelectric measurement of the film with mole fraction of  $0.67\text{PbTiO}_3$ - $0.33\text{CoFe}_2\text{O}_4$  was performed on Atomic Force Microscopy (AFM) based set up. Quantitative measurements of out-of-plane piezoelectric constant,  $d_{zz}$  reveal a clear hysteretic loop as shown in Fig.5.2. The hysteresis in the piezoresponse signal is directly associated with the polarization switching and ferroelectric properties of the sample.

$d_{zz}$  hysteresis loops were asymmetric and shift either to the right or to the left side. Because the films normally have a platinum top electrode and a  $\text{SrRuO}_3$  bottom electrode, this asymmetry may be due to different barrier potential between electrodes and the film. To eliminate the electrode effect  $30\mu\text{m}$  round shape  $\text{SrRuO}_3$  pattern was deposited on film top surface. However, the hysteresis loops remained to be asymmetric. The possible explanation for  $d_{zz}$  hysteresis loop shift is the presence of an internal electric field inside the film or pinning of domain walls by defects.

The values of piezoresponce,  $d_{zz} = 45, 20$  and  $13$  pm/V were obtained in the out plane piezoelectric coefficient measurement on  $\text{SrTiO}_3$  (100), (110) and (111) substrates, respectively. The measured piezoresponse of films were compared with

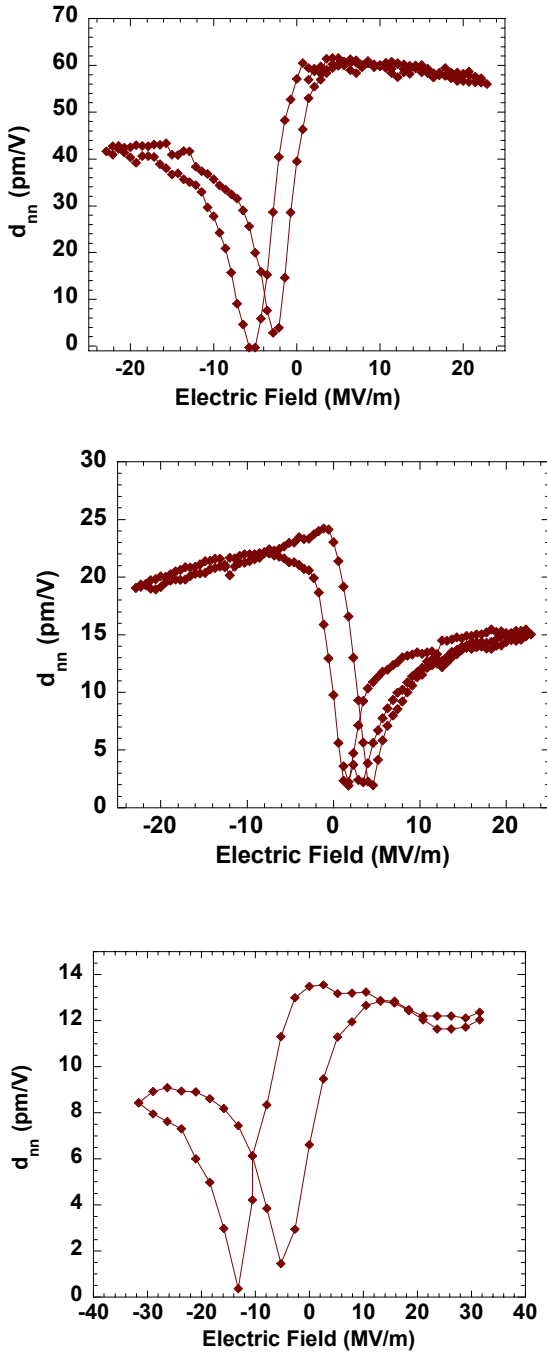


Fig. 5.2  $d_{zz}$  loop for the  $0.67\text{PbTiO}_3\text{-}0.33\text{CoFe}_2\text{O}_4$  thin film grown on differently oriented  $\text{SrTiO}_3$  substrates: a) (001), b) (110), c) (111)

bulk values, with theoretical calculations in continuous films as well as with theoretical calculations in multiferroic films.

The effective piezoelectric coefficient of a substrate-constrained single domain film as the function of crystallographic orientation has been studied theoretically in [25]. It has been concluded that the  $d_{zz}$  has maximum in a direction of tetragonal axis [001] and it progressively decreases for [011] and [111]. The calculated piezoelectric coefficients of  $\text{PbTiO}_3$  single domain thin films on (001), (110) and (111) substrates are  $\sim 70\text{pm/V}$ ,  $\sim 50\text{pm/V}$  and  $40\text{pm/V}$ . For multiferroic films consisting of  $\text{CoFe}_2\text{O}_4$  and  $\text{PbTiO}_3$  the piezoresponse,  $d_{33}^f = \frac{d\varepsilon_{33}^{\text{tot}}}{dE}$ , has been calculated using phase field modeling. The total strain due to applying electrical field,  $E$ , is calculated taking into account that the self-strain in  $\text{PbTiO}_3$  phase is:

$$\varepsilon_0 = \begin{pmatrix} Q_{31}P_s^2 + d_{31}E & 0 & 0 \\ 0 & Q_{31}P_s^2 + d_{31}E & 0 \\ 0 & 0 & Q_{33}P_s^2 + d_{33}E \end{pmatrix}$$

where  $d_{31} = -28 \text{ pm/V}$ ,  $d_{33} = 84 \text{ pm/V}$  [52],  $Q_{31} = -0.026 \text{ m}^4/\text{C}^2$ ,  $Q_{33} = 0.089 \text{ m}^4/\text{C}^2$  and  $P_s = 75 \text{ C/N}$  (bulk  $\text{PbTiO}_3$ ). The strain distributions corresponding to multiferroic films of different orientations are shown in Fig.5.3.

Theoretical and experimental results are presented in Fig.5.4. The orientation dependence of piezoresponce of multiferroic films demonstrates the same trend as a piezoresponce of single crystals and continuous films. There is a reasonable agreement between experimental and calculated values of  $d_{zz}$ . The small

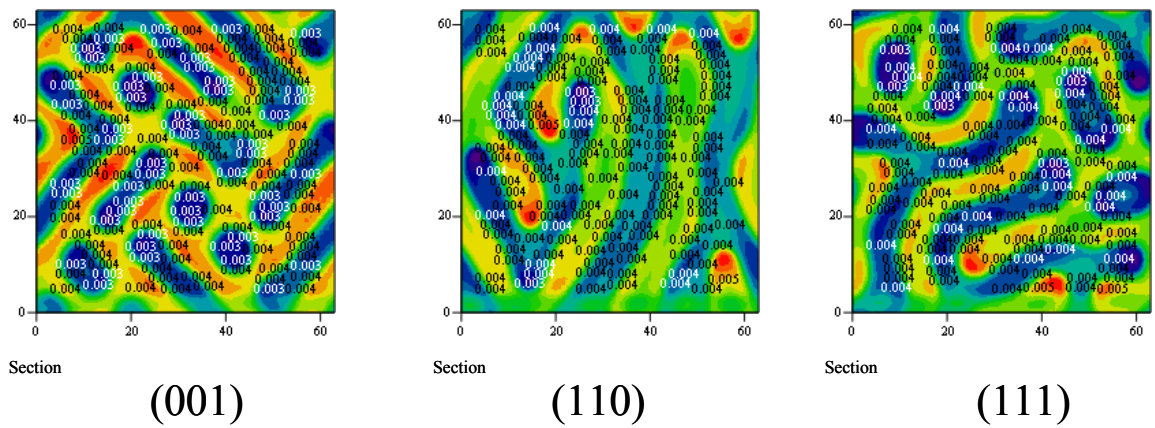


Fig.5.3 The color maps showing the strain distributions in multiferroic nanostructures in  $0.33\text{CoFe}_2\text{O}_4-0.67\text{PbTiO}_3$  on differently oriented substrates.

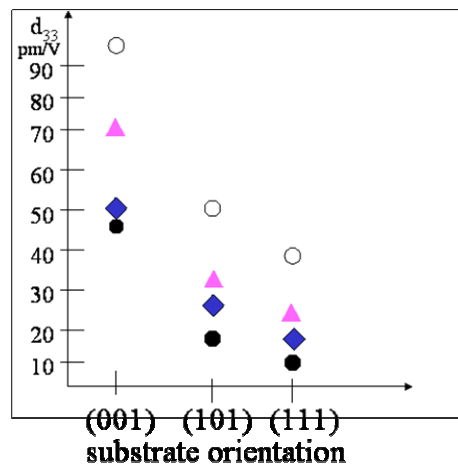


Fig.5.4 Piezoresponce of differently oriented  $\text{PbTiO}_3$ : single crystal (bulk) (white circles), theoretic calculations for continue film (triangles) [25], phase field modeling results for multiferroic films ( $0.33\text{CoFe}_2\text{O}_4-0.67\text{PbTiO}_3$ ) (rhombus), experimental measurements of the multiferroic films with the same composition (black circles).

discrepancies can be attributed to neglecting of elastic inhomogeneity in the phase field modeling.

## ***5.2 Ferromagnetic Properties***

Ferromagnetic measurements were carried out on superconducting quantum interference device magnetometer measurement (SQUID) and the characterization of magnetization hysteresis loop is listed in table 5.1. The different thin film orientations have different magnetization behavior in terms of easy axial orientation, coercive field, remnant magnetization. The magnetic hysteresis loops of 0.67PbTiO<sub>3</sub>-0.33CoFe<sub>2</sub>O<sub>4</sub> films and 0.33PbTiO<sub>3</sub>-0.67CoFe<sub>2</sub>O<sub>4</sub> differently oriented films with thickness 230 nm are shown in Figs.5.5 and 5.6, respectively. In Fig.5.7 the magnetization loops for 0.67PbTiO<sub>3</sub>-0.33CoFe<sub>2</sub>O<sub>4</sub> (001) oriented films with ferrite rods of very small diameter are presented.

Comparison of hysteresis loops for in-plane and out-of-plane directions of magnetic films for films with larger fraction of CoFe<sub>2</sub>O<sub>4</sub> phase shows that the in-plane magnetization of the film is easiest. It can be explained that in this case the magnetic properties of the film are similar to the magnetic properties of continuous films which usually have the in-plane easy axis.

For the films with smaller fraction of CoFe<sub>2</sub>O<sub>4</sub> the properties of the films are more determined by the magnetization of individual rods of lamellas. Particularly, in case of (001) oriented films, direction of easy magnetization depends on the aspect ratio of ferromagnetic rods. For large aspect ratio it is expected that easy direction of the film magnetization will be along the rods, i.e.[001]. However, due to negative

effect of tensile stress created by ferroelectric matrix, this direction can be changed to in-plane magnetization for smaller aspect ratio of the rods. Our experiments support this conclusion. In the films containing rods with diameter  $\sim 20\text{-}30$  nm the easy direction of magnetization lies in the film plane (Fig.5.5a), while in the films containing rods with diameter  $\sim 10\text{nm}$  and correspondingly aspect ratio more than 20, the easy axes of the film magnetization is out-of-plane (see section 5.3 ).

It is difficult to estimate preferred direction of magnetization for the case of (011) and (111) oriented films because of complex interactions between stress state, magnetic and shape anisotropy. However, the analysis of magnetization curves of (110) films allow us to conclude that the magnetization almost isotropic in-plane of ferrite (1-10) platelets (Fig.5.5b). The magnetic anisotropy of  $0.33\text{CoFe}_2\text{O}_4\text{-}0.66\text{PbTiO}_3$  (110) thin film has been investigated by applying in-plane magnetic field along both the (100) and (110) directions, which was done by rotating the sample by  $45^\circ$  as well as with field applied in-plane field along (100) and out-of-plane field along (001).

The saturation magnetization  $M_s$  for all the films is lower than the bulk value of the  $\text{CoFe}_2\text{O}_4$  ( $\sim 410$  emu/cm<sup>3</sup>). The decrease of saturation magnetization is due to constraints of the magnetic phase by the ferroelectric phase and the substrate. This reduction further supports that the functional response and consequently magneto-electric coupling of multiferroic nanostructures is governed by elastic interactions between phases.

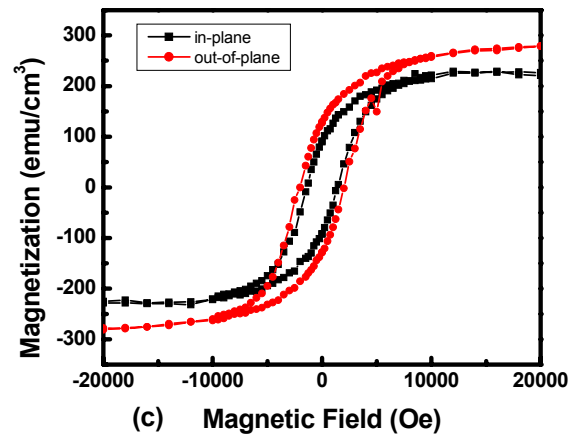
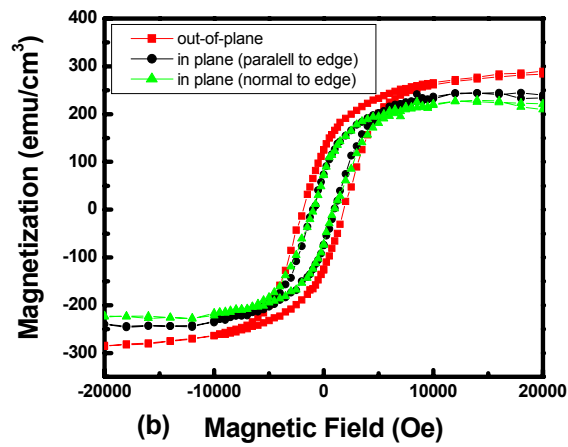
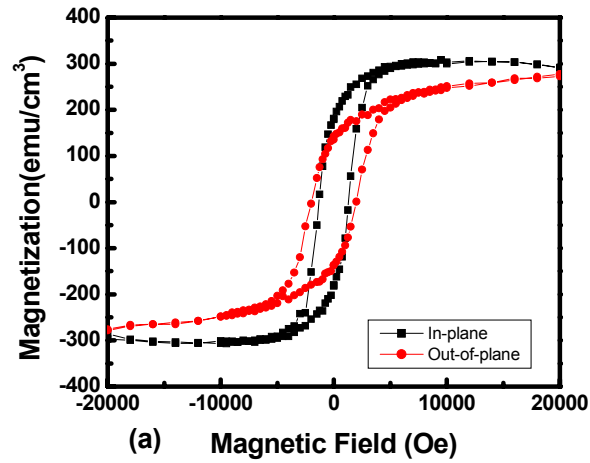
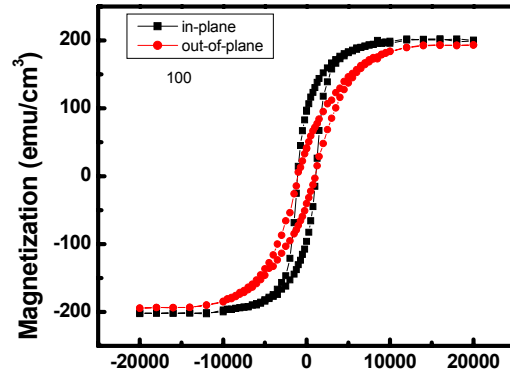
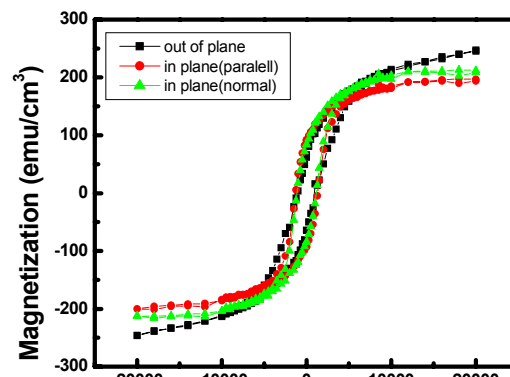


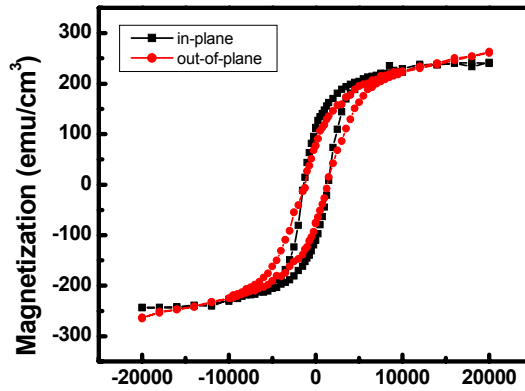
Fig. 5.5 Magnetization hysteresis loop for the  $0.67\text{PbTiO}_3\text{-}0.33\text{CoFe}_2\text{O}_4$  film grown on differently oriented  $\text{SrTiO}_3$ : a) (001), b) (110), c) (111)



(a) Magnetic Field (Oe)



(b) Magnetic Field (Oe)



(c) Magnetic Field (Oe)

Fig. 5.6 Magnetization hysteric loop for the  $0.33\text{PbTiO}_3\text{-}0.67\text{CoFe}_2\text{O}_4$  film grown on differently oriented  $\text{SrTiO}_3$ : a) (001), b) (110), c) (111)

Table. 5.1 Parameters of magnetic hysteresis loop

| <b>Sample</b>   |                           | <b>H<sub>c</sub> (Oe)</b> | <b>M<sub>R</sub> (emu/cm<sup>3</sup>)</b> | <b>M<sub>S</sub>(emu/cm<sup>3</sup>)</b> | <b>M<sub>R</sub>/M<sub>S</sub></b> |
|---|---------------------------|---------------------------|---|--|------------------------------------|
| <b>0.67PbTiO<sub>3</sub>-<br/>0.33CoFe<sub>2</sub>O<sub>4</sub></b> | <b>[100] in-plane</b>     | <b>1250</b>               | <b>207</b>                                | <b>300</b>                               | <b>0.69</b>                        |
|   | <b>[100] out-of-plane</b> | <b>2000</b>               | <b>142</b>                                | <b>300</b>                               | <b>0.47</b>                        |
|   | <b>[110] in-plane</b>     | <b>750</b>                | <b>110</b>                                | <b>245</b>                               | <b>0.45</b>                        |
|   | <b>[110] out-of-plane</b> | <b>2000</b>               | <b>150</b>                                | <b>283</b>                               | <b>0.53</b>                        |
|   | <b>[111] in-plane</b>     | <b>1500</b>               | <b>112</b>                                | <b>226</b>                               | <b>0.50</b>                        |
|   | <b>[111] out-of-plane</b> | <b>2000</b>               | <b>148</b>                                | <b>279</b>                               | <b>0.53</b>                        |
| <b>0.33PbTiO<sub>3</sub>-<br/>0.67CoFe<sub>2</sub>O<sub>4</sub></b> | <b>[100] in-plane</b>     | <b>1000</b>               | <b>124</b>                                | <b>200</b>                               | <b>0.66</b>                        |
|   | <b>[100] out-of-plane</b> | <b>1000</b>               | <b>66</b>                                 | <b>192</b>                               | <b>0.34</b>                        |
|   | <b>[110] in-plane</b>     | <b>1000</b>               | <b>94</b>                                 | <b>195</b>                               | <b>0.48</b>                        |
|   | <b>[110] out-of-plane</b> | <b>1000</b>               | <b>94</b>                                 | <b>248</b>                               | <b>0.38</b>                        |
|   | <b>[111] in-plane</b>     | <b>1250</b>               | <b>127</b>                                | <b>234</b>                               | <b>0.54</b>                        |
|   | <b>[111] out-of-plane</b> | <b>1250</b>               | <b>82</b>                                 | <b>260</b>                               | <b>0.32</b>                        |

### ***5.3 Tuning magnetic easy axial from in-plane to out-of-plane***

The multiferroic magnetic nano-pillars structure is a promising candidate for the future multifunctional storage technology. As longitudinal recording storage has reached the areal density limit, perpendicular storage opens the opportunity to achieve much higher density recording. We demonstrate here the possibility to switch the easy axis from in-plane to out-of-plane for the film with pillar-in-matrix nanostructure.

Since the magnetic anisotropy is determined by crystallographic, shape and stress anisotropy, then if we keep crystallographic and shape anisotropy the same, we should expect tuning magnetic hysteresis behavior by varying the stress state in  $\text{CoFe}_2\text{O}_4$  nano-pillars and switch the magnetic easy axis from in-plane to out-of-plane by changing the tensile stress to compressive stress. On the other hand, we can keep crystallographic and stress anisotropy the same, increase the out-of-plane shape anisotropy, or combine these two to obtain the out-of-plane easy axis of magnetization.

The film with thickness of about 350nm, and the diameter of nano-pillar is about 10nm has been grown on (001) substrate. The in-plane and out-of-plane magnetization loops are presented in Fig.5.6. Fig.5.7 shows the plane view dark field image of the film. TEM plane view shows round shape  $\text{CoFe}_2\text{O}_4$  pillars distributed in  $\text{PbTiO}_3$  matrix. The nano-pillars grow through the whole thickness of the film as it is seen at TEM cross-section. The aspect ratio of the rods is larger than 30 and shape anisotropy dictated out-of-plane easy direction the film magnetization.

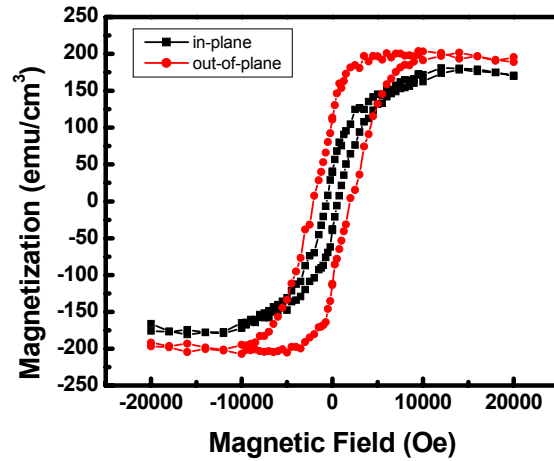


Fig.5.7 Magnetization hysteresis loop of  $0.67\text{PbTiO}_3\text{-}0.33\text{CoFe}_2\text{O}_4$  with the  $\text{CoFe}_2\text{O}_4$  pillars having the aspect ratio of  $\sim 35$  as compared to  $\sim 5$ , as shown in Fig. 5.5

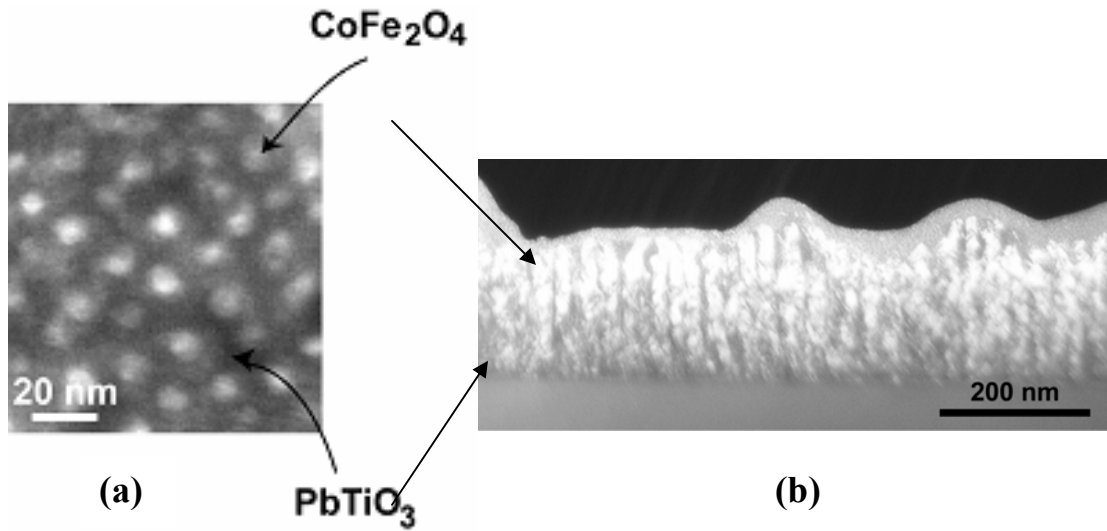


Fig.5.8 TEM dark-field images of the  $0.67\text{PbTiO}_3\text{-}0.33\text{CoFe}_2\text{O}_4$  film with the  $\text{CoFe}_2\text{O}_4$  nano-pillars, having a height-to-diameter ratio of 35, embedded in the  $\text{PbTiO}_3$  matrix. a) plane view; b) cross-section

# CONCLUSIONS

1. We successfully fabricate self-assembling multiferroic nanostructure films of  $\text{CoFe}_2\text{O}_4\text{-PbTiO}_3$  by PLD deposition on  $\text{SrTiO}_3$  substrates of different orientations. X-ray and TEM characterization show that all films have columnar architecture and 3D epitaxial relationships between phases and each phase and substrates.
2. The morphology of nanostructures has been controlled by changing orientation of a substrate. It has been shown that it is possible to obtain the ferrimagnetic ( $\text{CoFe}_2\text{O}_4$ ) rods with a diameter about 10-20 nm in the ferroelectric  $\text{PbTiO}_3$  matrix in (001) films of composition 0.67  $\text{PbTiO}_3\text{-0.33 CoFe}_2\text{O}_4$ , and vice versa: ferroelectric rods in ferrimagnetic matrix in (111) films of composition 0.33  $\text{PbTiO}_3\text{-0.67 CoFe}_2\text{O}_4$ . The lamellate morphology with a specific crystallographic orientation of lamellae corresponding to  $\{111\}$  planes has been obtained in (110) films.
3. The measurement of lattice parameters of constitutive phases at different temperature allows us to determine the level of internal stresses due to misfit between phases.
4. The measurements of piezo and magnetic responses of the films prove that the films are ferroelectric and ferromagnetic simultaneously. The piezo- and magnetic responses are considerable suppressed due to mutual constraints between phases. This suppression indicates the strong elastic interactions between the phases which allows us to suggest the strong electro-magnetic coupling in the films.

5. Combining theoretical and experimental studies of self-assembled multiferroic nanostructures in epitaxial films have revealed that the elastic interactions caused by epitaxial stresses play the dominate role in defining the morphology of the nanostructures and their magnetic and electric responses.

## Journal paper:

- **Jianhua Li**, Igor. Levin, Julia Slutsker, Alelander L Roytburd, et al, *Functional Properties in the CoFe<sub>2</sub>O<sub>4</sub>-PbTiO<sub>3</sub> Multiferroic Nanostructures*, Journ.. Appl. Phys. (to be submitted)
- Julia Slutsker, Igor Levin, **Jianhua Li**, Andrei Artemev and Alexander L.Roytburd, *Effect of Elastic Interactions on the Self-Assembly of Multiferroic Nanostructures in Epitaxial Films*, submitted to Phys. Rev. Lett.
- **Jianhua Li**, Igor. Levin, Julia Slutsker, Virgil Provenzano, and Peter K. Schenck, R. Ramesh, Jun Ouyang Alexander. L. Roytburd, *Self-assembled multiferroic nanostructures in the CoFe<sub>2</sub>O<sub>4</sub>-PbTiO<sub>3</sub> system*, Appl. Phys. Lett. 87, 072909 (2005).
- **Jianhua Li**, Lang. Chen, V. Nagarajan, R. Ramesh, Alexander L Roytburd et al, *Finite element modeling of piezoresponse in nanostructured ferroelectric films*, Appl. Phys. Lett. 84, 2626 (2004).
- Lang. Chen, **Jianhua Li**, Julia. Slutsker, Jun. Ouyang, and Alexander L. Roytburd, *Contribution of substrate to converse piezoelectric response of constrained thin films*, Journal of Materials Research, 19, 2853(2004)

## Conference presentation:

- *Multiferroic self-assembly nanostructures in epitaxial films*, US-Japan Seminar on Piezoelectric and Ferroelectric Materials. (Annapolis, November, 2005)
- *Tailoring Epitaxial Multiferroic Self-Assembled Nanostructures: CoFe<sub>2</sub>O<sub>4</sub>-PbTiO<sub>3</sub> Case Study*, 2005 Materials Research Society Winter Meeting. (Boston, MA - 2005)
- *Multiferroic PbTiO<sub>3</sub>-CoFe<sub>2</sub>O<sub>4</sub> Nanostructures in Constrained Epitaxial Films on SrTiO<sub>3</sub> Substrate*, 2004 Materials Research Society Winter Meeting. (Boston, MA - 2004)
- *Finite element modeling of piezoresponse in nanostructured ferroelectric films*, Materials Research Society Winter Meeting. (Boston, MA - 2003)

## APPENDIX

- **Jianhua Li**, Lang. Chen, V. Nagarajan, R. Ramesh, Alexander L Roytburd et al, *Finite element modeling of piezoresponse in nanostructured ferroelectric films*, Appl. Phys. Lett. 84, 2626 (2004).
- Lang. Chen, **Jianhua Li**, Julia. Slutsker, Jun. Ouyang, and Alexander L. Roytburd, *Contribution of substrate to converse piezoelectric response of constrained thin films*, Journal of Materials Research, 19, 2853(2004)

## Finite element modeling of piezoresponse in nanostructured ferroelectric films

J.-H. Li, L. Chen, V. Nagarajan, R. Ramesh, and A. L. Roytburd<sup>a)</sup>

Materials Research Science and Engineering Center, Department of Materials Science and Engineering, University of Maryland, College Park, Maryland 20742

(Received 22 September 2003; accepted 9 February 2004)

Patterning thin ferroelectric films into discrete islands is an effective way to release the constraint imposed by a substrate and the unpoled nonpiezoactive surrounding film to enhance the film piezoresponse. The converse piezoresponse measured by the surface displacement of ferroelectric islands, with lateral size changing from a nanoscale to a continuous film, has been modeled using three-dimensional finite element method. The modeling has shown that piezodeformation of the islands results in a local deformation of a substrate in the vicinity of island. The deformation is larger when the substrate is softer. The deformation, together with clamping strain in the film, decreases the effective  $d_{33}$  of the film island. The effect of the top electrode on  $d_{33}$  measured by surface displacement is also modeled. The piezoresponse of different size island capacitors with  $\text{PbZr}_{0.5}\text{Ti}_{0.5}\text{O}_3/\text{SrTiO}_3/\text{Si}$  and  $\text{PbZr}_{0.2}\text{Ti}_{0.8}\text{O}_3/\text{SrTiO}_3$  heterostructures has been calculated. The results of modeling are in good agreement with experimental data on  $d_{33}$  obtained by piezoresponse force microscopy. © 2004 American Institute of Physics. [DOI: 10.1063/1.1695641]

Large piezoelectric coefficients of  $\text{PbZr}_{1-x}\text{Ti}_x\text{O}_3$  (PZT) family compared to other materials make them very attractive as functional materials for a variety of applications, such as sensors and actuators. However, due to the clamping effects of surrounding media, i.e., the substrate, the unpoled nonpiezoactive surrounding film (in cases that only parts of the film were covered by the top electrode) and the top electrode, PZT thin films display a piezoelectric coefficient significantly smaller than the calculated intrinsic single crystal value.<sup>1-3</sup> It has been predicted theoretically<sup>4</sup> and demonstrated experimentally<sup>4-6</sup> that patterning the ferroelectric thin film into discrete islands greatly enhanced the piezoresponse of the films. It is the purpose of this letter to investigate quantitatively the converse piezoresponse of ferroelectric film islands on a substrate by three-dimensional finite element method (FEM) analysis. It is demonstrated that the local deformation of the substrate plays a significant role in the piezoresponse of ferroelectric films clamped by the substrate and therefore cannot be ignored. The piezoresponse of different size island capacitors with  $\text{PbZr}_{0.5}\text{Ti}_{0.5}\text{O}_3/\text{SrTiO}_3$  (STO)/Si and  $\text{PbZr}_{0.2}\text{Ti}_{0.8}\text{O}_3/\text{STO}$  heterostructures has been calculated. The results of the FEM simulation are in good agreement with experimental data on  $d_{33}$  obtained by piezoresponse force microscopy.

Consider an epitaxial heterostructure consisting of an island of a ferroelectric thin film and a substrate with lateral size and thickness much larger than those of the island [ $H \gg h$  and  $L \gg l$ , Fig. 1(a)]. The electric field  $E$  is applied along the polarization normal to the film. The boundary conditions for the field-induced strain and stress can be summarized as: (1) The tractions on all free surfaces are zero at  $\Omega_2$ ,  $\Omega_3$ , the displacement vector  $u_k^s = 0$  at  $\Omega_1$  because the bottom of the substrate is fixed on the sample plate, (2) the in-plane strain should be compatible at the film/substrate interface  $\Omega_4$ ,  $\epsilon_{ij}^f$

+  $\epsilon_{ij}^0 = \epsilon_{ij}^s$  ( $i, j = 1, 2$ ), the superscript  $s$  and  $f$  represent the substrate and film, respectively,  $\epsilon_{ij}$  is the strain and  $u_k$  is the displacement.

The commercial software ANSYS is used to model the converse piezoresponse of ferroelectric thin films with the aspect ratio ( $l/h$ ) from 80 down to 0.5. The electromechanical constitutive equations are  $\epsilon_i = S_{ij}\sigma_j + d_{ki}E_k$ ,  $D_k = d_{ki}\sigma_i + \eta_{kl}E_k$ , where  $D_k$  is electric displacement vector,  $S_{ij}$  is elastic compliance coefficient,  $\eta_{kl}$  is the dielectric constant, and  $d_{ki}$  is the piezoelectric constant. For simplicity, the Voigt matrix notation is employed in this FEM calculation hereafter. Couple field element SOLID 5 is employed to mesh the model. The finite element grid size is nonuniform with a larger density of grid points placed in the film and the nearby region of the substrate. Because of the symmetry of the model, only one-quarter of the model was analyzed. The film, the substrate, and the top electrode are approximately treated as elastically isotropic materials. The scanning electron microscopy images and the corresponding FEM simulations are presented in Fig. 2.

To investigate the influence of substrate on the converse piezoresponse of ferroelectric films, different substrates with the relative ratio  $\gamma = Y_f(1 - \nu_s)/Y_s(1 - \nu_f)$  (the film elastic

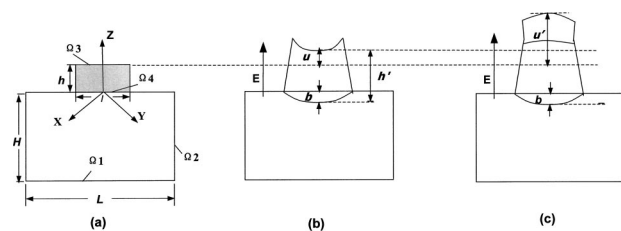


FIG. 1. Schematic diagram of a ferroelectric thin film and a substrate: (a) Initial state, (b) the film and the substrate under the electric field, and (c) the deformations of top electrode and the film/substrate interface under the electric field.

<sup>a)</sup>Electronic mail: royttburd@wam.umd.edu

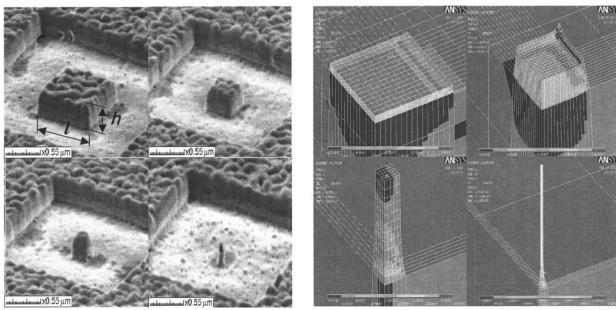


FIG. 2. Scanning electron microscopy images and FEM modeling of the piezodeformation of different size ferroelectric thin-film islands: (a)  $l/h = 80$ , (b)  $l/h = 20$ , (c)  $l/h = 5$ , and (d)  $l/h = 1$ .

modulus to the substrate modulus) ranges from 0.1 to 2.5 are studied, representing rigid and soft substrates compared with films, where  $Y$  is Young's modulus,  $\nu$  is the Poisson ratio, and subscripts  $s$  and  $f$  stand for substrate and film. Under the electric field, the film is bended into the substrate since the constraint from the film compresses the upper level of the substrate as shown in Fig. 1(b). Due to the large substrate size compared with the film, only the region in a vicinity of the film is deformed. The film/substrate interface deflection  $b$  due to the elastic deformation and the top surface displacement of film  $u$  are feasibly to be read from the simulation result and so does the film thickness change  $\Delta h = u - b$ . Here,  $u$  is measured at the center point of the film. The converse piezoelectric coefficient  $d_{33}^f$  can be calculated from the measured surface displacement:  $d_{33}^f = u/Eh$ .

Figure 3(a) demonstrates the surface displacement (being normalized with respect to the displacement of free standing film  $u_0 = d_{33}Eh$ ) as a function of the aspect ratio  $l/h$ . When  $l/h$  is small, the surface displacement approaches the intrinsic piezoresponse  $u_0$ . As  $l/h$  increases, the surface displacement decreases and finally approaches a constant value, which depends on the relative elasticity ratio  $\gamma$ . For different substrates, the surface displacement is smaller for softer substrates with larger  $\gamma$ .

The two contributions to the film surface displacement are the deflection of the film/substrate interface and the change of the film thickness. Being normalized with respect to  $u_0$ , they are plotted in Figs. 3(b) and 3(c). Both the deflection of the film/substrate interface and the thickness change are results of a strain field, which is induced by the substrate clamping. When  $l/h < 1$ , the strain field is located only in a very small region near the interface so that the film is almost stress free, the deflection and additional thickness change due to the clamping can be ignored<sup>4</sup> and  $u \approx u_0$ . As  $l/h$  increases, the film becomes more constrained by the

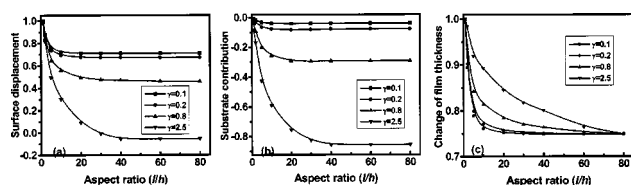


FIG. 3. Surface displacement  $u$ , film/substrate interface deflection  $b$ , and change of thickness  $\Delta h$  normalized with respect to  $u_0$  are plotted as functions of  $l/h$ : (a) The variation of surface displacement vs  $l/h$ , (b) the variation of film/substrate interface deflection  $b$  vs  $l/h$ , and (c) the change of thickness vs  $l/h$ .

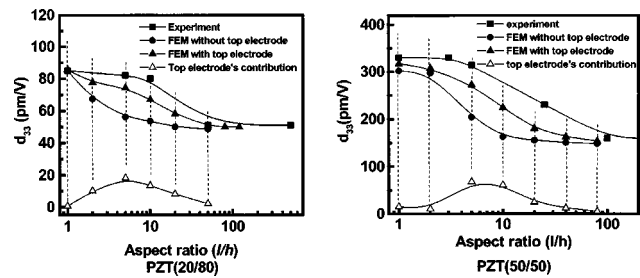


FIG. 4. Comparison of FEM modeling with experiment: (a)  $\text{PbZr}_{0.2}\text{Ti}_{0.8}\text{O}_3$  (PZT 20/80) and (b)  $\text{PbZr}_{0.5}\text{Ti}_{0.5}\text{O}_3$  (PZT 50/50). The solid squares, triangles, and circles represent results of the experiment, simulation with and without the contribution of the top electrode, respectively; the open triangles plot the contribution of top electrode.

substrate, the elastic strains in films and substrates increase, which reduces the piezostain and enlarges the interface deflection. When  $l/h \gg 1$ , the film is fully constrained by the substrate, the constraint confines both the film thickness change and the film/substrate interface deflection. The film thickness change approaches the same level independent on  $\gamma$ , which corresponds to the strain in the film on ideally rigid substrate,<sup>1</sup> i.e.,  $d_{33}^f = d_{33} + 2\nu_f d_{31}/(1 - \nu_f)$ . The displacement of a film/substrate interface obtains different levels depending on the relative elasticity ratio  $\gamma$  and the stiffness of the film and the substrate. The soft substrate demonstrates larger deflection than the rigid one. The comparison of Figs. 3(b) and 3(c) shows that the local deformation of the substrate cannot be omitted when the surface displacement of the film is considered, especially for the soft substrates. For example, when  $\gamma$  is 0.8, the surface displacement is reduced by one third due to the local deformation of the substrate; when  $\gamma$  is 2.5, the surface displacement becomes negative due to the large deflection downward into the substrate. From the FEM simulation above, it was concluded that the total surface displacement  $u$  is determined by three factors shown in Fig. 1(b): Piezostain corresponding to the intrinsic  $d_{33}$ , elastic strain in the film due to the constraint imposed by the substrate, and local nonuniform deformation of the substrate  $b$ .

The effect of local substrate deformation considered here is different from the effect of the whole substrate bending, which has been discussed in Refs. 2 and 7. The strain field spreads through small area under a piezodeformed island in depth approximately equal to the length of the in-plane size of the island. So the bottom surface of the substrate remains undistorted, and the surface displacement does not depend on boundary condition of the substrate.

The converse piezoresponse of  $\text{PbZr}_{0.2}\text{Ti}_{0.8}\text{O}_3/\text{STO}$  and  $\text{PbZr}_{0.5}\text{Ti}_{0.5}\text{O}_3/\text{STO}/\text{Si}$  is calculated, and  $d_{33}$  is calculated through the surface displacement is compared with the experimental results obtained by piezoresponse force microscopy,<sup>4-6</sup> presented in Figs. 4(a) and 4(b). The 100 nm  $\text{PbZr}_{0.2}\text{Ti}_{0.8}\text{O}_3$  and 200 nm  $\text{PbZr}_{0.5}\text{Ti}_{0.5}\text{O}_3$  thin films are deposited on the STO and Si substrates using pulsed laser deposition, where the thickness of the substrates is around 5 mm. The focus ion-beam milling technique is employed to make small size capacitors down to 0.1  $\mu\text{m}$ . The details of these experiments have been reported elsewhere.<sup>6</sup> In FEM analysis, the elastic constants are:  $Y = 148$  GPa,  $\nu = 0.3$  for  $\text{PbZr}_{0.2}\text{Ti}_{0.8}\text{O}_3$ ,  $Y = 118$  GPa,  $\nu = 0.2$  for  $\text{PbZr}_{0.5}\text{Ti}_{0.5}\text{O}_3$ , and

the piezoelectric constants  $d_{33}$  and  $d_{31}$  are 90 and  $-27$  pm/V for  $\text{PbZr}_{0.2}\text{Ti}_{0.8}\text{O}_3$ ; 325 and  $-156$  pm/V for  $\text{PbZr}_{0.5}\text{Ti}_{0.5}\text{O}_3$ , respectively.<sup>8</sup> The observation for the fully clamped film ( $l/h=80$ ) agrees very well with the experimental measurements, which are the result of strain in a thin piezoelectric film clamped by a thick substrate<sup>1</sup> and the additional contribution from substrate local deformation. Figures 4(a) and 4(b) show that the simulation predictions qualitatively agree with the experiment results, as  $l/h$  increases, however the calculated  $d_{33}$  values drop faster than the experimental ones.

To improve the accuracy of the simulation, the effect of a top electrode should be taken into account if the thickness of the top electrode is comparable with the thickness of a thin film.<sup>2</sup> With the 120 nm thick top electrodes, the simulation results are presented in solid triangle symbols in Figs. 4(a) and 4(b). The in-plane piezoelectric contraction of the film compresses the top electrode and increases its thickness as seen in Fig. 1(c), which contributes to the surface displacement.<sup>2,9</sup> The contribution of the top electrode to the effective  $d_{33}$  is determined by two factors: (1) The electric-field-induced in-plane deformation of the film which induces the in-plane deformation of the top electrode. (As the lateral size of the film becomes larger, the constraint of the film by a substrate increases resulting in decrease of in-plane deformation of the film. Therefore, the in-plane deformation of the electrode decreases as well as the contribution to the normal displacement decrease) and (2) the constraint between the film and the top electrode that determines the influence of the film on the top electrode. As the aspect ratio  $l/h$  increases, the interaction between the film and the electrode increases, resulting in an increase in the thickness of the top electrode due to Poisson's effect. Due to these two competing effects, the top electrode contribution has a maximum at the aspect ratio  $l/h$  equals 5–6 (Fig. 4). When the film is fully constrained by the substrate, there is no in-plane deformation, accordingly, the top electrode does not deform at all. The FEM simulating results including the effect of top electrode

agree well with the experiments with minor inconsistency. One possible cause of this minor disagreement is the elastic isotropic approximation used in the FEM calculation.

In summary, the FEM analysis presented explains the lateral size dependence of piezoelectric responses in constrained ferroelectric thin films. The analysis reveals that the  $d_{33}$  measured through the surface displacement should include four parts: (1) The intrinsic piezostain, (2) the strain induced by substrate constraint, (3) the substrate local deformation, and (4) the top electrode deformation. The local deformation of the substrate significantly reduces the measured  $d_{33}$ . The contribution of the top electrode can compensate for the bending effect when  $1 < l/h < 40$ , however, it is negligible when the film is free from constraint ( $l/h < 1$ ) or the film is fully clamped by the substrate ( $l/h > 80$ ). The piezoresponse force microscopy experimental measurements for two heterostructures  $\text{PbZr}_{0.2}\text{Ti}_{0.8}\text{O}_3/\text{STO}$  and  $\text{PbZr}_{0.5}\text{Ti}_{0.5}\text{O}_3/\text{STO}/\text{Si}$  agree well with the FEM predications.

This work is sponsored by the NSF-MRSEC under Grant No. 008-0008 and the NSF under Grant No. DMR 0210512.

<sup>1</sup>K. Lefki and G. J. M. Dormans, *J. Appl. Phys.* **76**, 1764 (1994).

<sup>2</sup>R. Steinhausen, T. Hauke, W. Seifert, V. Müller, H. Beige, S. Seifert, and P. Löbmann, *Proceedings of the 11th IEEE International Symposium on Applications of Ferroelectrics* (IEEE, New York, 1998), p. 93.

<sup>3</sup>F. Xu, F. Chu, and S. Trolier-McKinstry, *J. Appl. Phys.* **86**, 588 (1999).

<sup>4</sup>A. L. Roytburd, S. P. Alpay, V. Nagarajan, C. S. Ganpule, S. Aggarwal, E. D. Williams, and R. Ramesh, *Phys. Rev. Lett.* **85**, 190 (2000).

<sup>5</sup>S. Buhlmann, B. Dwir, J. Baborowski, and P. Muralt, *Appl. Phys. Lett.* **80**, 3195 (2002).

<sup>6</sup>V. Nagarajan, A. Stanishevsky, L. Chen, T. Zhao, J. Melngailis, A. L. Roytburd, and R. Ramesh, *Appl. Phys. Lett.* **81**, 4215 (2002).

<sup>7</sup>A. Barzegar, D. Damjanovic, N. Ledermann, and P. Muralt, *J. Appl. Phys.* **93**, 4756 (2003).

<sup>8</sup>It is difficult to obtain reliable data on the elastic properties of PZT films. Here, isotropic elastic approximations from bulk PZT data were used in the FEM modeling, which still qualitatively demonstrated the local bending effects.

<sup>9</sup>A. L. Roytburd, *Integr. Ferroelectr.* **38**, 119 (2001).

# Contribution of substrate to converse piezoelectric response of constrained thin films

Lang Chen, J-H. Li, J. Slutsker, J. Ouyang, and A.L. Roytburd<sup>a)</sup>

Materials Research Science and Engineering Center, Department of Materials Science and Engineering, University of Maryland, College Park, Maryland 20742

(Received 7 November 2003; accepted 26 April 2004)

The converse piezoelectric response of a thin film constrained by a substrate is analyzed in different geometries under various boundary conditions. We consider the effects of elastic deformation of the substrate on the total displacement of the film surface induced by the electric field. The change of film thickness and the bending curvature of a film/substrate couple are calculated. For a thin film island clamped on a large thick substrate, the theoretical estimation of the piezoresponse, including a local bending in the vicinity of the island/substrate interface, is in agreement with the finite element calculation.

## I. INTRODUCTION

Understanding of the piezoresponse of piezoelectric thin films is essential in the design and fabrication of microsensors, actuators, and other electromechanical devices.<sup>1-9</sup> In principle, the converse piezoresponse may be characterized by applying a voltage (field) and measuring the field-induced strain. For example, if a thin film has a tetragonal structure with the polarization along the  $c$  axis normal to the film (along the  $z$  direction), and epitaxially oriented on a cubic substrate layer with the interface along  $(001)_T // (001)_C$ , the field-induced strain in the film is

$$\hat{\epsilon}_0 = \begin{bmatrix} d_{31}E & 0 & 0 \\ 0 & d_{31}E & 0 \\ 0 & 0 & d_{33}E \end{bmatrix}, \quad (1)$$

where  $d_{33}$  and  $d_{31}$  are the longitudinal and transverse piezoelectric coefficients of a free-standing piezoelectric film, and  $E$  is the applied electric field normal to the film. From the calculation of the total strain in the film clamped by a substrate, it has been concluded that the effective piezoelectric coefficient of the thin film follows<sup>1</sup>

$$d_{33}^f = d_{33} - \frac{2d_{31} S_{13}^f}{(S_{11}^f + S_{12}^f)}, \quad (2)$$

where  $S_{ij}^f$  are the mechanical compliances of the film under constant electric field. Equation (2) demonstrates

that  $d_{33}^f$  measured by the strain in the film is independent of elastic properties of a substrate if the film is completely clamped by the substrate.

However, the piezostain of a constrained thin film cannot be directly measured by the standard resonance method due to the substrate clamping.<sup>2</sup> Most of the static or quasi-static techniques such as cantilever deflection,<sup>3</sup> laser interferometry<sup>4,5</sup> and atomic force microscopy<sup>5-9</sup> provide the effective piezoelectric coefficients through the measurement of the displacement of the film or the thickness change of the sample (from the top surface of the film to the bottom surface of the substrate) instead of the strain in the film. To understand the experimental measurements, we studied the total piezoresponse of a film/substrate couple, including changes of thickness of the film and the substrate, as well as a bending deflection of the film/substrate couple. The theoretical calculation shows that  $d_{33}^f$  measured through the surface displacement still depend on the substrate elastic compliances and the boundary conditions. Equation (2) is correct to describe effective piezoresponse measured from the surface displacement only if the substrate boundaries are fixed as shown in Fig. 1(a) or if the substrate is ideally rigid without any elastic deformation. The results of calculation of the film island/substrate heterostructure piezoresponse are in good agreement with the finite element method (FEM) simulations.<sup>10</sup>

## II. THIN FILM/SUBSTRATE COUPLE

For a two-layer plate with a thickness much smaller than the in-plane dimension  $L$ , which consists of a piezoelectric layer with thickness  $h$  and a substrate with thickness  $H$  [Fig. 1(b)], the elastic problem on the

<sup>a)</sup>Address all correspondence to this author.

e-mail: royburd@wam.umd.edu

DOI: 10.1557/JMR.2004.0367

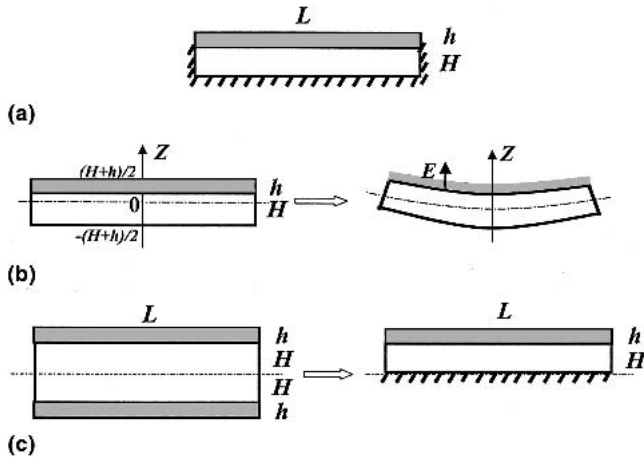


FIG. 1. Different boundary conditions of a thin film ( $h$ ) on a much thicker substrate ( $H$ ): (a) fixed bottom and side surfaces of the substrate; (b) bending of two-layer plates consisting of a piezoelectric thin film and a substrate, initial state of the film and substrate (left) and the thin film and substrate under the electric field along  $z$  coordinates (right); and (c) symmetrical three-layer film/substrate/film stack (left), corresponding to the fixed bottom surface of the substrate (right).

deformation of a film/substrate couple becomes one-dimensional.<sup>11,12</sup> To elucidate the role of the substrate in the total piezodisplacement, we choose a simple case commonly used in experiments and applications: the thin film has a tetragonal structure with the polarization along the  $c$  axis normal to the film, and it is epitaxially oriented on the cubic substrate layer.

The out-of-plane stress of the film is zero due to the conditions of no traction at free top surface. The in-plane stresses of the film and substrate are

$$\begin{aligned} \sigma_{11}^f &= \sigma_{22}^f = G^f (\bar{\epsilon} + kz - d_{31}E) \\ \sigma_{11}^s &= \sigma_{22}^s = G^s (\bar{\epsilon} + kz) \end{aligned} \quad (3)$$

where the planar elastic modulus of the film and/or substrate is  $G^{f,s} = 1/(S_{11}^{f,s} + S_{12}^{f,s})$ , the superscripts  $f$  and  $s$  stand for the film and the substrate respectively,  $\bar{\epsilon}$  and  $k$  are the average strain and the curvature. The constants  $\bar{\epsilon}$  and  $k$  can be determined by the requirement that both the average internal stress and the average momentum of internal stress should be equal to zero<sup>11,12</sup>

$$\int_{-(h+h)/2}^{+(H+h)/2} \sigma(z)dz = 0 \text{ and } \int_{-(H+h)/2}^{+(H+h)/2} z\sigma(z)dz = 0 \quad (4)$$

The solution of Eq. (4) is

$$\begin{aligned} k &= 12d_{31}E\alpha(1 - \alpha)\gamma/HN \quad , \\ \bar{\epsilon} &= \alpha d_{31}E\{[1 - (1 - 2\alpha)^3] \\ &\quad + \gamma[1 + (1 - 2\alpha)^3] - 6\alpha(1 - \alpha)^2 \\ &\quad (1 - \gamma)\}/N \quad . \end{aligned} \quad (5)$$

where  $N = [\alpha + (1 - \alpha)\gamma]\{[1 - (1 - 2\alpha)^3] + \gamma[1 +$

$(1 - 2\alpha)^3]\} - 6\alpha^2(1 - \alpha)^2(1 - \gamma)^2$ ,  $\alpha = h/(H + h)$  is the fraction of film in the film/substrate couple,  $\gamma = G^f/G^s$  is the ratio of planar elastic modulus between the film and the substrate, respectively.

When the thickness of the thin film is much smaller than the thickness of the substrate ( $h \ll H$ ), the curvature and the average strain can be simplified as

$$\begin{aligned} k &= 6d_{31}E\alpha\gamma/H \quad , \\ \bar{\epsilon} &= \alpha d_{31}E\gamma \quad . \end{aligned} \quad (6)$$

The limit of  $\alpha \rightarrow 0$  is corresponding to a completely clamped thin film. The stress in the substrate is negligible compared with that of the film. The in-plane stress in the film is  $\sigma_{11} = \sigma_{22} = -G^f d_{31}E$ ; therefore the out-of-plane strain in the film is

$$\epsilon_3^f = d_{33}E - S_{13}^f(\sigma_{11} + \sigma_{22}) = d_{33}E - 2S_{13}^f G^f d_{31}E \quad , \quad (7)$$

which corresponds exactly to Eq. (2).

However, Eq. (2) is not sufficient when the surface displacement instead of the strain of the film is measured. The total displacement of the top surface of the film  $u$  consists of contributions from the thickness changes of both the thin film and the substrate  $\Delta h$  and the bending deflection  $b$ .

The total thickness change  $\Delta h$  can be integrated from the displacements of the film and the substrate as

$$\begin{aligned} \Delta h &= d_{33}Eh + \int_{(H-h)/2}^{(H+h)/2} \frac{2S_{13}^f(\bar{\epsilon} + kz - d_{31}E)dz}{(S_{11}^f + S_{12}^f)} \\ &\quad + \int_{-(H+h)/2}^{(H-h)/2} \frac{2S_{13}^s(\bar{\epsilon} + kz)dz}{(S_{11}^s + S_{12}^s)} \quad , \end{aligned} \quad (8)$$

where the in-plane strain has been transformed into the out-of-plane strain by Poisson effect. Thus the effective  $d_{33}^f$  measured through thickness change is equal to  $\Delta h$  divided by  $Eh$  (voltage)

$$d_{33}^f = d_{33} - \frac{2d_{31}S_{13}^f}{(S_{11}^f + S_{12}^f)} + \frac{2d_{31}S_{13}^s}{(S_{11}^s + S_{12}^s)} \gamma \quad , \quad (9)$$

where the first term on the right side is the intrinsic piezodeformation of a free-standing film, the second term is a negative contribution due to the clamping effect, and the last term is an additional positive contribution due to the elastic deformation of the substrate because the compliance  $S_{13}^s$  has a negative value generally. It also proves that Eq. (2) is correct for describing the effective piezoresponse based on the thickness change of the film if the substrate boundaries are fixed as in Fig. 1(a) or if the substrate is ideally rigid, where the contribution from the substrate disappears.

In general, Eq. (9) demonstrates that the elastic deformation of the substrate contributes to the total thickness change of the film/substrate couple and partially compensates the effect of clamping imposed by the substrate: (i) if the elastic properties of the substrate are the same with that of the thin film  $S_{13}^s = S_{13}^f$ , the elastic deformation of the substrate exactly compensates the clamping effects of the thin film, which means that the total thickness change of the film/substrate couple is equal to the thickness change of the film without constraint; (ii) the substrate elastic deformation may exceed the clamping effect if a substrate is much softer than the film,  $|S_{13}^s| > |S_{13}^f|$ , which means that the third term on the right side of Eq. (9) becomes much larger than the second term. Therefore, even if a film is thinner than a substrate, the total displacement of the film on the substrate still depends on the elastic properties of the substrate.

The bending of the film/substrate couple leads to a deflection that is considerably large if the in-plane size of a substrate or a film  $L$  is much larger than the thickness of the substrate,  $H$ . When  $h \ll H$ , the curvature of the bending is described as  $1/\rho = k = 6hd_{31}E\gamma/H^2$  [Eq. (6)], which corresponds to the commonly used Stoney approximation. The bending deflection is

$$b = \frac{(L/2)^2}{2\rho} = \frac{3hd_{31}E\gamma}{4} \left(\frac{L}{H}\right)^2, \quad (10)$$

which depends on the square of the substrate aspect ratio  $L/H$ . Thus for  $L/H > 10$ , the bending contribution to the surface displacement of the film/substrate couple can be more than an order of magnitude greater than the intrinsic piezoelectric effect of the film.<sup>4,14</sup> Note that the bending deflection results in a displacement that has an opposite sign with the electric field induced displacement of the film, because  $d_{31}E$  is negative when  $d_{33}E$  is positive. Therefore, the effective piezoelectric coefficient can be much less than the fully clamped coefficient predicted by Eq. (2) or can even have a large negative

value if the piezoresponse is measured through the surface displacement.

For a symmetrical three-layer stack consisting of two piezoelectric thin films and an inactive substrate layer, as illustrated in the left part of Fig. 1(c), the bending is eliminated. When  $h \ll H$ , the film/substrate couple with fixed bottom surface (right) can be treated as a symmetrical case (left) as shown in Fig. 1(c). The effective  $d_{33}^f$  measured through the total thickness change in the symmetrical case coincides with Eq. (9).<sup>15</sup> It means that the effective  $d_{33}^f$  measured through the thickness change of the bent film/substrate couple is equal to the thickness change of the film/substrate couple with a fixed bottom surface.

### III. THIN FILM ISLAND ON A LARGE SUBSTRATE

It is of practical interest to consider the case of patterning ferroelectric (piezoelectric) thin films into discrete islands (Figs. 2 and 3). It has been shown theoretically and experimentally that the patterning of the epitaxial films reduces the degree of constraint, so that the submicron islands of thin films have a much larger  $d_{33}^f$  than that of the completely clamped films.<sup>7-9</sup> Note that the patterned thin film islands also reduce the clamping by the surrounding unpoled film.<sup>13</sup>

Three-dimensional FEM simulation was used to model the converse piezoresponses of ferroelectric islands measured through the top surface displacement (Fig. 3). It has been shown that the top surface displacement of the film  $u$  and the substrate contribution (characterized as the displacement of the film/substrate interface)  $u_s$ , both of which are normalized with respect to the piezodisplacement of a free-standing film,  $u_0 = d_{33}Eh$ , are functions of the aspect ratios of the film islands  $l/h$  (Fig. 4).<sup>10</sup> The FEM simulation has also shown that the piezodeformation of the island results in a local deformation of a substrate in the vicinity of the island (Fig. 3). The effect of local substrate deformation considered here is different from the effect of the whole substrate bending.<sup>4,14</sup>

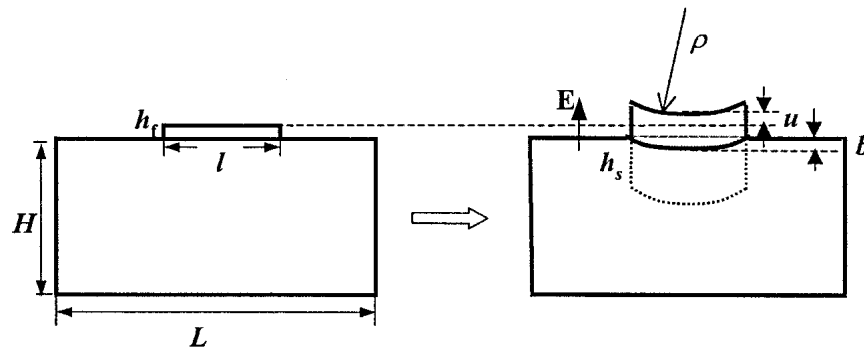


FIG. 2. Island of a piezoelectric thin film on a large thick substrate: (a) the initial state, (b) the deformations of the film and the substrate under the electric field. The local bending curvature radius is  $\rho$ , the film lateral size is  $l$ , and the film thickness is  $h_f$ . The substrate lateral size  $L$  and thickness  $H$  is much larger than those of the film island ( $H \gg h_f$  and  $L \gg l$ ). The substrate effective thickness is  $h_s$ .

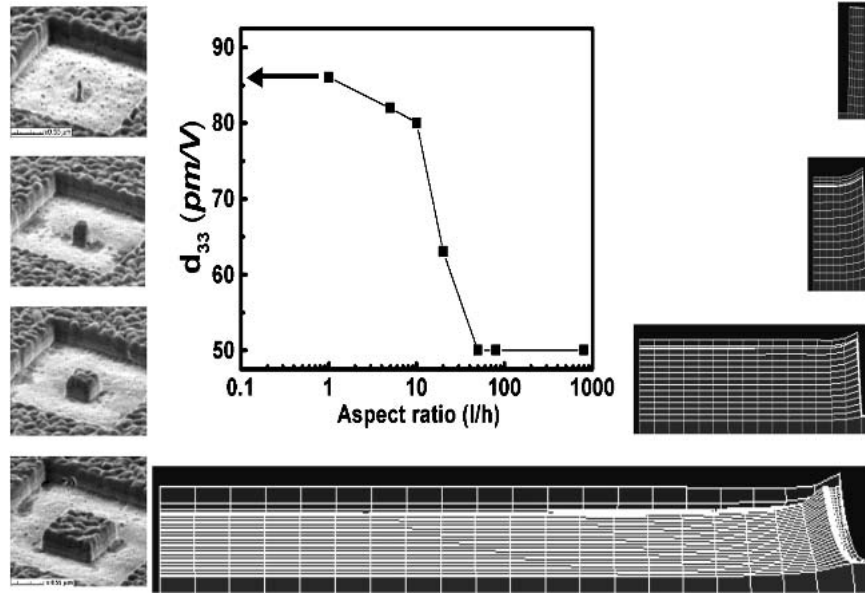


FIG. 3. SEM images of the thin film islands with aspect ratio  $l/h = 1, 5, 20,$  and  $80$  (from up to bottom) and the corresponding FEM simulations (right), which present the bending interfaces. The inset picture is an example of piezoresponse microscopy measurement results for different size thin film islands.

The strain field spreads through the area under a piezo-deformed island in a distance that is approximately equal to the length of the in-plane size of the island. So the bottom surface of substrate remains undistorted, and the surface displacement does not depend on boundary condition of the substrate. This local deformation becomes larger when the substrate is softer. The local deformation, together with the clamping strain in the film, decreases the effective  $d_{33}^f$  of the film island.

When the aspect ratio of the film island  $l/h$  is small, the surface displacement approaches the intrinsic piezodisplacement  $u_0$ , because the strain field spreads only through a small region near the film/substrate interface so that the film is almost stress free, and the bending deflection can be ignored. As  $l/h$  increases, the effective  $d_{33}^f$  decreases and finally approaches a constant value depending on the relative elasticity ratio  $\gamma$ . The surface displacement  $u$  is smaller for softer substrates with smaller  $\gamma$ . When  $l/h$  increases, the film becomes more constrained by the substrate, and the elastic strain in the film and the substrate increases, reduces the film thickness change  $\Delta h_f$ , and enlarges the interface deflection. When the film becomes fully constrained by the substrate, the constraint stress reaches the maximum, which confines the film/substrate interface deflection with the saturation level depending on  $\gamma$ , and the thickness change of the film with the same saturation level independent with  $\gamma$  (Fig. 4).

To estimate the saturation levels in Fig. 4, we assume that the local bending near the film island can be considered as the bending of the film on a substrate with an effective thickness,  $h_s = \eta l$  ( $\eta$  is a fitting parameter to be

determined), because the stress field inside the substrate diminishes at the depth larger than the film lateral size  $l$ . The local bending curvature is  $1/\rho = 6h_f d_{31} E \gamma / (\eta^2 l^2)$  and the local bending displacement at the center point of the film island is  $b = (3h_f d_{31} E \gamma) / (4\eta^2)$  when  $l \gg h_f$  ( $l/h_f \geq 80$ ). Thus the effective  $d_{33}^f$ , measured through the total surface displacement including the thickness change of the film, the elastic deformation of the substrate, and the local bending deflection, being normalized to  $d_{33}$ , can be written as

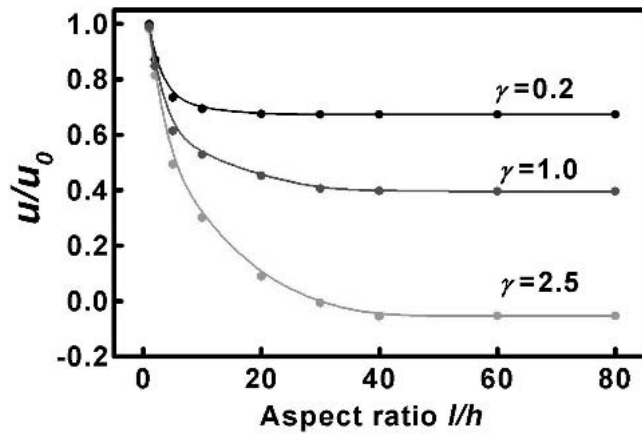
$$\frac{d_{33}^f}{d_{33}} = 1 - \frac{d_{31}}{d_{33}} \frac{2S_{13}^f}{(S_{11}^f + S_{12}^f)} + \frac{d_{31}}{d_{33}} \frac{2S_{13}^s \gamma}{(S_{11}^s + S_{12}^s)} + \frac{d_{31}}{d_{33}} \frac{3\gamma}{4\eta^2} \quad (11)$$

Compared with Eq. (9), the local bending displacement gives an additional negative contribution, which appears as the last term on the right side of Eq. (11).

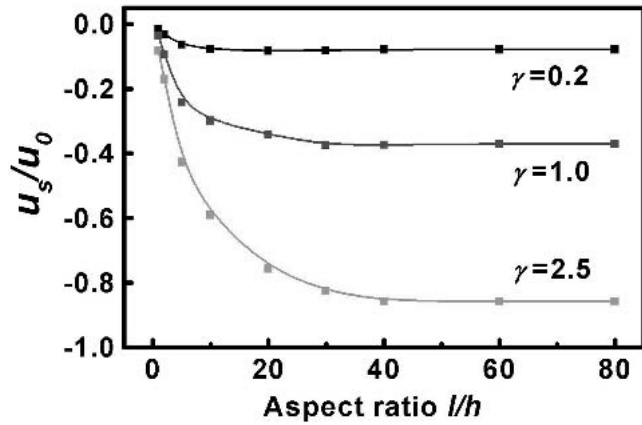
To find the fitting parameter  $\eta$ , we compared Eq. (11) with the results of the FEM calculation (Fig. 5). Since the elastic isotropic approximation has been used in the FEM simulation, Eq. (11) can be reduced to

$$\frac{d_{33}^f}{d_{33}} = 1 + \frac{d_{31}}{d_{33}} \frac{2\nu^f}{(1 - \nu^f)} + \frac{d_{31}}{d_{33}} \left[ -\frac{2\nu^s}{(1 - \nu^s)} + \frac{3}{4\eta^2} \right] \gamma \quad (12)$$

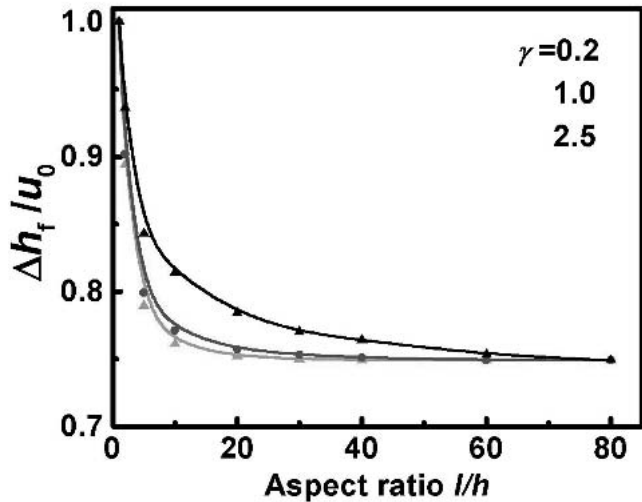
where  $\gamma = [Y^f / (1 - \nu^f)] / [Y^s / (1 - \nu^s)]$ ,  $Y$  is the Young's modulus, and  $\nu$  is Poisson's ratio. Different substrates with the relative ratio  $\gamma$  ranging from 0.1 to 2.5 are studied, representing relatively rigid and soft substrates.



(a)



(b)



(c)

FIG. 4. FEM simulation results of surface displacement  $u$ , film/substrate interface deflection  $b$ , and change of film thickness  $\Delta h_f$  normalized with respect to  $u_0$  are plotted as functions of the film aspect ratio  $l/h$ : (a) variation of surface displacement versus  $l/h$ , (b) variation of film/substrate interface deflection  $b$  versus  $l/h$ , and (c) change of thickness versus  $l/h$ , which all approach saturations at different levels depending on the relative planar elastic modulus  $\gamma$ .

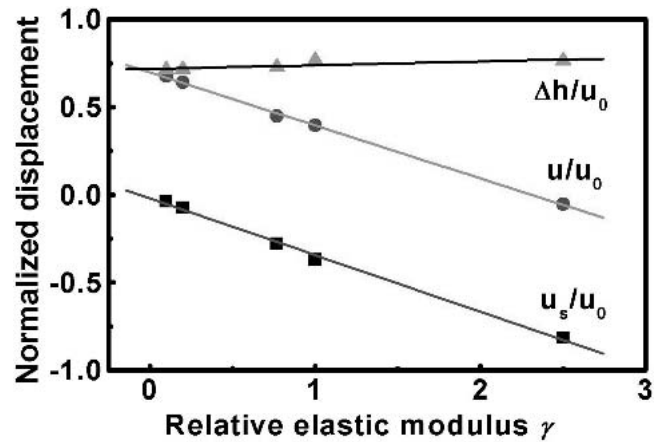


FIG. 5. Saturation points (when  $l/h = 80$ ) of the surface displacement  $u$  (circles), substrate contribution  $u_s$  (squares), and film thickness change  $\Delta h_f$  (triangles) normalized with respect to  $u_0$  are plotted as functions of  $\gamma$ . The least square fitting lines were presented as well.

In the plotting of dependences of the normalized surface displacement ( $u/u_0$ ) and the normalized total substrate contribution ( $u_s/u_0$ ) on the relative elastic modulus  $\gamma$ , the slope  $\theta$  is equal to

$$\frac{d_{31}}{d_{33}} \left[ -\frac{2\nu^s}{(1-\nu^s)} + \frac{3}{4\eta^2} \right]. \quad (13)$$

In the FEM simulations,  $d_{31}/d_{33} = -1/3$ ,  $\nu^f = \nu^s = 0.3$  were used. The results of the slopes after the least square fittings in Fig. 5 are:  $\theta = -0.30, -0.32$ , and  $0.02$ , respectively, for the normalized surface displacement  $u/u_0$ , substrate contribution  $u_s/u_0$ , and thin film thickness change  $\Delta h_f/u_0$ , with respect to  $\gamma$ . It proves that  $u$  and  $u_s$  have almost the same dependence with the relative elastic modulus  $\gamma$  according to Eq. (13), while  $\Delta h_f$  is almost constant and independent of  $\gamma$  according to Eqs. (2) and (7). This comparison of the FEM calculation results with the theoretical predictions justifies the approximation used for local bending effect. The fitting parameter is  $\eta = 0.65$  calculated from the slopes. For the saturation points at aspect ratio  $l/h$  from 80 to 100, the thickness of the effective substrate is 52–65 times larger than the thickness of the thin film, which means it still obeys the prerequisite conditions of Eqs. (6)–(9). Although the edge effect<sup>16</sup> of the film island was not considered theoretically, the boundary conditions of the thin film island on the large thick substrate were different from that of a film/substrate couple without lateral constraint; the results of piezodisplacement in the center point of the island based on the effective substrate model were still in good agreement with FEM calculations.

#### IV. CONCLUSION

In summary, the theoretical analysis based on different geometries and boundary conditions has demonstrated

that the effects of the substrate contribution play a significant role in the converse piezoelectric response of the piezoelectric thin film on a substrate and therefore cannot be neglected. The elastic deformation of the substrate contributes positively to the total piezodisplacement. However, the film/substrate bending can give much larger negative deflections. Therefore the optimum approach to maximize the piezodisplacement is to either use stacks consists of alternating piezoelectric thin film layers and soft substrate layers or use a thin film/substrate couple with large bending deflection. The local bending of a piezoelectric film island on a large substrate still presents a negative contribution to the total displacement of the film island/substrate heterostructure. The analysis of the total piezoresponse versus aspect ratio of thin film indicates that to obtain large displacement in small patterned devices (islands), it is necessary to keep the aspect ratio as small as possible to eliminate the clamping effects and reduce the local bending effects. All the results presented above are based on the electromechanical analysis only and therefore are valid for all piezoelectric films.

## ACKNOWLEDGMENTS

This work is supported by the National Science Foundation under Grant No. DMR 0210512 and the NSF-Material Research Science & Engineering Center program under Grant No. DMR 00-80008.

## REFERENCES

1. K. Lefki and G.J.M. Dormans: Measurement of piezoelectric coefficients of ferroelectric thin films. *J. Appl. Phys.* **76**, 1764 (1994).
2. F. Xu, F. Chu, and S. Trolier-McKinstry: Longitudinal piezoelectric coefficient measurement for bulk ceramics and thin films using pneumatic pressure rig. *J. Appl. Phys.* **86**, 588 (1999).
3. M-A. Dubois and P. Muralt: Measurement of the effective transverse piezoelectric coefficient  $e_{31,f}$  of AlN and Pb(Zr<sub>x</sub>Ti<sub>1-x</sub>)O<sub>3</sub> thin films. *Sens. Actuators A* **77**, 106 (1999).
4. A.L. Kholkin, C. Wüthrich, D.V. Taylor, and N. Setter: Interferometric measurements of electric field-induced displacements in piezoelectric thin films. *Rev. Sci. Instrum.* **67**, 1935 (1996).
5. H. Maiwa, J.A. Christman, S.H. Kim, D.J. Kim, J.P. Maria, B. Chen, S.K. Streiffer, and A.I. Kingon: Measurement of piezoelectric displacements of Pb(Zr, Ti)O<sub>3</sub> thin films using a double-beam interferometer. *Jpn. J. Appl. Phys. Part 1*, **38**, 5402 (1999).
6. J.A. Christman, R.R. Woolcott, A.I. Kingon, and R.J. Nemanich: Piezoelectric measurements with atomic force microscopy. *Appl. Phys. Lett.* **73**, 3851 (1998).
7. A.L. Roytburd, S.P. Alpay, V. Nagarajan, C.S. Ganpule, S. Aggarwal, E.D. Williams, and R. Ramesh: Measurement of internal stresses via the polarization in epitaxial ferroelectric films. *Phys. Rev. Lett.* **85**, 190 (2000).
8. S. Buhlman, B. Dwir, J. Baborowski, and P. Muralt: Thermodynamic theory of stress distribution in epitaxial Pb(Zr, Ti)O<sub>3</sub> thin films. *Appl. Phys. Lett.* **75**, 3195 (2002).
9. V. Nagarajan, A. Stanishevsky, T. Zhao, L. Chen, J. Melngailis, A.L. Roytburd, and R. Ramesh: Realizing intrinsic piezoresponse in epitaxial submicron lead zirconate titanate capacitors on Si. *Appl. Phys. Lett.* **81**, 4215 (2002).
10. J-H. Li, L. Chen, V. Nagarajan, R. Ramesh, and A.L. Roytburd: Finite element modeling of piezoresponse in nanostructured ferroelectric films. *Appl. Phys. Lett.* **84**, 2626 (2004).
11. A.L. Roytburd and J. Slutsker: Theory of multilayer SMA actuators. *Mater. Trans.* **43**, 1023 (2002).
12. M. Finot and S. Suresh: Small and large deformation of thick and thin-film multi-layers: Effects of layer geometry, plasticity and compositional gradients. *J. Mech. Phys. Solids* **44**, 683 (1996).
13. R. Steinhausen, T. Hauke, W. Seifert, V. Müller, H. Beige, S. Seifert, and P. Löbmann: Clamping of piezoelectric thin films on metallic substrates: Influence on the effective piezoelectric Modulus  $d_{33}$ . In *Proceedings of the 11th IEEE ISAF 98*, edited by Enrico Colla, Dragan Damjanovic, and Nava Setter (The Institute of Electrical and Electronic Engineers, Ferroelectrics and Frequency Control Society), Piscataway, NJ (1998), p. 93.
14. A. Barzegar, D. Damjanovic, N. Ledermann, and P. Muralt: Piezoelectric response of thin films determined by charge integration technique: Substrate bending effects. *J. Appl. Phys.* **93**, 4756 (2003).
15. A.L. Roytburd: Piezoresponse of constrained ferroelectric films. *Integr. Ferroelectr.* **38**, 119 (2001).
16. C-H. Hsueh: Analyses of edge effects on residual stresses in film strip/substrate systems. *J. Appl. Phys.* **88**, 3022 (2000).

## REFERENCE

- [1] Ascher E, Rieder H, Schmid H and Stössel H 1966 *J. Appl. Phys.* **37** 1404
- [2] Smolensky G A, Agranovskaya A I and Isupov V A 1959 *Sov. Phys.—Solid State* **1** 149
- [3] Smolensky G A, Isupov V A, Krainik N N and Agranovskaya A I 1961 *Isv. Akad. Nauk SSSR, Ser Fiz.* **25** 1333
- [4] Brixel W, Rivera J P, Steiner A and Schmid H 1988 *Ferroelectrics* **79** 201
- [5] Astrov D N, Alshin B I, Tomashpolski Y Y and Venevtsev Y N 1969 *Sov. Phys.—JETP* **28** 1123
- [6] Drobyshev L A, Alshin B I, Tomashpolski Y Y and Venevtsev Y N 1970 *Sov. Phys.—Crystallogr.* **14** 634
- [7] Van Suchtelen J 1972 *Philips Res. Rep.* **27** 28.
- [8] Van de Boomgaard J, Terell D R and Born R A J 1974 *J. Mater. Sci.* **9** 1705.
- [9] Van de Boomgaard J and Born R A J 1978 *J. Mater. Sci.* **13** 1538.
- [10] Van de Boomgaard J, van Run A M J G and van Suchtelen J 1976 *Ferroelectrics* **14** 727.
- [11] Chang K S, Aronova M A, Lin C-L, Murakami M, Yu M H, Hattrick-Simpers J, Famodu O O, Lee S Y, Ramesh R, Wuttig M, Takeuchi I, Gao C and Bendersky L A 2004 *Appl. Phys. Lett.* **84** 3091.
- [12] Murugavel P, Saurel D, Prellier W, Simon Ch and Raveau B 2004 *Appl. Phys. Lett.* **85** 4424.
- [13] Murugavel P, Padhan P and Prellier W 2004 *Appl. Phys. Lett.* **85** 4992.
- [14] Murugavel P, Singh M P, Prellier W, Mercey B, Simon Ch and Raveau B 2005 *J. Appl. Phys.* **97** 103914.
- [15] Singh M P, Prellier W, Simon Ch and Raveau B 2005 *Appl. Phys. Lett.* **87** 022505.
- [16] Ueda K, Tabata H and Kawai T 1998 *Science* **290** 1064.

- [17] Zheng H, Wang J, Lofland S E, Ma Z, Mohaddes-Ardabili L, Zhao T, Salamanca-Riba L, Shinde S R, Ogale S, B, Bai F, Viehland D, Jia Y, Schlom D G, Wuttig M, Roytburd A and Ramesh R 2004 *Science* **303** 661.
- [18] Zheng H, Wang J, Mohaddes-Ardabili L, Wuttig M, Salamanca-Riba L, Schlom D G and Ramesh R 2004 *Appl. Phys. Lett.* **85** 2035.
- [19] Roytburd A, and Sung G, 1993 MRS Symp., Proc. **311**, 143.
- [20] Zheng H, Thesis, 2004.
- [21] Roytburd A, 1999 *The Japan Institute of Metals*, Proc. of the Intern. Conf. on Solid-Solid Phase transformation'99 (JMIC-3) 1275.
- [22] Lines M. E. and Glass A. M, *Ferroelectrics and related materials*, Oxford, 1977.
- [23] Lines M. E. and Glass A. M., *Principles and Applications of Ferroelectrics and Related Materials*, Oxford, 1977.
- [24] Ouyang J, Yang S.Y, Chen L, Ramesh R, and Roytburd L A, 2004 *Appl. Phys. Lett.* **85** 278.
- [25] Ouyang J., Ramesh R and Roytburd L A., 2005 *Advanced Engineering Materials*, **7**, 229.
- [26] [www.intellimat.com](http://www.intellimat.com)
- [27] Kittel C, *Introduction to Solid State Physics*, 1976.
- [28] Wood E Van, and Austin E A, *Magnetoelectric interaction phenomena in crystals*, edited by A. J. Freeman and H. Schmid, Gordon and Breach Science Publishers, 1975
- [29] Smolenskii A G, and Chupis E I, 1982 *Sov. Phys. Usp.* **25**, 475.
- [30] Sharan A, An I, Chen C, Collins R W, Lettieri J, Jia Y, Schlom D G and Gopalan V 2003 *Appl. Phys. Lett.* **83** 5169
- [31] Sharan A, Lettieri J, Jia Y, Tian W, Pan X, Schlom D G and Gopalan V 2004 *Phys. Rev. B* **69** 214109
- [32] Son J Y, Kim B G, Kim C H and Cho J H 2004 *Appl. Phys. Lett.* **84** 4971
- [33] Palkar V R, John J and Pinto R 2002 *Appl. Phys. Lett.* **80** 1628
- [34] Wang J, Neaton J B, Zheng H, Nagarajan V, Ogale S B, Liu B, Viehland

- D, Vaithyanathan V, Schlom D G, Waghmare U V, Spaldin N A, Rabe K M, Wuttig M and Ramesh R 2003 *Science* **299** 1719
- [35] Imada S, Shouriki S, Tokumitsu E and Ishiwara H 1998 *Japan. J. Appl. Phys.* **37** 6497
- [36] Imada S, Kuraoka T, Tokumitsu E and Ishiwara H 2001 *Japan. J. Appl. Phys.* **40** 666
- [37] Ito D, Fujimura N, Yoshimura T and Ito T 2003 *J. Appl. Phys.* **94** 4036
- [38] Ito D, Fujimura N and Ito T 2000 *Japan. J. Appl. Phys.* **39** 5525
- [39] Yoshimura T, Fujimura N and Ito T 1998 *Appl. Phys. Lett.* **73** 414
- [40] Lee H N, Kim Y T and Park Y K 1999 *Appl. Phys. Lett.* **74** 3887
- [41] Neaton J B, Ederer C, Waghmare V U, Spaldin A N, and Rabe M K 2005 *Phys. Rev. B* **71**, 014113.
- [42] Murakami M, Chang K-S, Aronova A M, Lin C-L, Yu Ming H, Simpers Hatrick J, Wuttig M, Takeuchi I, Gao C, Hu B, Lofland E S, Kanuss A L and Bendersky A L, 2005 *Appl. Phys. Lett.* **87** 112901.
- [43] Baettig P and Spaldin N A 2005 *Appl. Phys. Lett.* **86** 012505
- [44] Stein S, Wuttig M, Viehland D and Quandt E, 2005 *J. Appl. Phys.* **97** 10Q301.
- [45] Zavaliche F, Zheng H, Mohaddes A L, Yang S Y, Zhan Q, Shafer P, Reilly E, Chopdekar R, Jia Y, Wright P, Schlom D G, Suzuki Y, Ramesh R, 2005 *Nano Lett.* **5** 1973.
- [46] Jona F, and Shirane G, *Ferroelectric Crystals*, Pergamon Press, New York, 1962.
- [47] Smolenskii A G, *Ferroelectric and Related Materials*, Gordon and Breach, New York, 1984.
- [48] Foster M C, Li Z, Buckett M, Miller D, Baldo M P, Rehn E L, Bai R G, Guo D, You H, and Merkle L K, 1995 *J. Appl. Phys.* **78** (4), 15.
- [49] Gavrilyachenko G V, and Fesenko G E, 1971 *Sov. Phys. Crystallogr.* **16**, 549.
- [50] Turik V. A, Fesenko G. E Gavrilyachenko G V, and Khasabova I. G, 1975 *Sov. Phys. Crystallogr.* **19**, 677.

- [51] Turik.V A, Shevchenko B N, Gavriyachenko G V., and Fesenko G E, 1979 *Phys. Status Solidi B* **94**, 525.
- [52] Li Z, Grimsditch H., Xu X, and Chan S-K, 1993 *Ferroelectrics* **141**, 313.
- [53] Freire D J. and Katiyar S R, 1988 *Phys. Rev. B* **37**, 2074.
- [54] Haun J M, Furman E, Jang J S., McKinstry A H, and Cross E L, 1987 *J. Appl. Phys.* **62**, 3331.
- [55] Okada M, Tominaga K, At&i T, Katayama S, and Sakashita Y, 1990 *Jpn. J.Appl. Phys.* **29**, 718.
- [56] Horwitz S J, Grabowski S K, Chrisey B D, and Leuchtner E R, 1991 *Appl.Phys. Lett.* **59**, 1565.
- [57] Okamura T, Ada&i M, Shiosaki T, and Kawabata A, Jpn. 1991 *J. Appl. Phys.* **30**, 1034.
- [58] Kawano T, Sei T, and Tsuckiya T, 1991 *Jpn. J. Appl. Phys.* **39**, 2178.
- [59] Xiao K, Zhu J, Wan D, Guo H, Xie B, and Yuan H, 1991 *Appl. Phys. Lett.* **58** 36.
- [60] Tominaga K, Miyajima M, Sakashita Y, Segawa H, and Okada M, 1990 *Jpn.J. Appl. Phys.* **29**, 1874.
- [61] Abe K, Tomita H, Toyoda H, Imai M, and Yokote Y, 1991 *Jpn. J. Appl. Phys.***30**, 2152.
- [62] Larsen K P, Dormas J. M G, Taylor J D, and van Veldhoven J P, 1994 *J. Appl. Phys.* **76**, 2405.
- [63] Foster C. M, Li Z, Buckett M, Miller D, Baldo M P, Rehn E L, Bai R G, D. Guo, You H, and Merkle L K, 1995 *J. Appl. Phys.*, **78** (4), 2607 August 1995
- [64] Lisfi A, Williams M C, Johnson A, Nguyen T L , Lodder C J , Corcoran H, Chang P and Morgan W J . 2005 *Phys.: Condens. Matter* **17** 1399.
- [65] Jackson J T, Palmer B S, 1994 *J. Phys. D: Appl. Phys.* **27**, 1581.
- [66] <http://mse.iastate.edu/microscopy/beaminteraction.html>
- [67] Maiwa H. and Ichinose N, 2000 *Jpn. J. Appld. Phys Part 1-Regular papers, short notes and review papers* **39**, 5403.
- [68] Buhlman S, Dwir B, Baborowski J, and Muralt P, 2002 *Appl. Phys. Lett.*

- 75**, 3195.
- [69] Nagarajan V., et al., 2002 *Appl. Phys. Lett.* **81**, 4215.
- [70] Traynor D S, Hadnagy D T., and Kammerdiner L, 1997 *Integrated Ferroelectrics* **16**, 63.
- [71] Roytburd L A, 1976 *Phys.Stat. Solidi A* **37**, 329.
- [72] Roytburd L A, *J. Appl. Phys.*, **83**, 238, (1998)
- [73] Li J, Levin I., Slutsker J, Provenzano V, and Schenck K P, Ramesh R, Ouyang J and Roytburd L A. , 2005 *Appl. Phys. Lett.* **87**, 072909.
- [74] Slutsker J, Levin I, Li J, Artemev A and Roytburd L A, *Effect of Elastic Interactions on the Self-Assembly of Multiferroic Nanostructures in Epitaxial Films*, submitted to *Phys. Rev. Lett.*
- [75] Speck S J, Pompe W, *J. Appl. Phys.* **76**, 466 (1994)
- [76] Alpay P S., Roytburd.L A, 1998 *J. Appl. Phys.* **83**, 4714.
- [77] Khachaturyan G A, *Theory of Structural Transformations in Solids*, New York: John Wiley & Sons, 1983.
- [78] Chen Z, Yu S, Meng L and Len Y, 2002 *Comp.Structure*, **75**,177.
- [79] Slutsker J, Artemev A, Roytburd L A, 2004 *Acta Mater.* **52**,1731.